BRNO UNIVERSITY OF TECHNOLOGY

VYSOKÉ UČENÍ TECHNICKÉ V BRNĚ

FACULTY OF MECHANICAL ENGINEERING

FAKULTA STROJNÍHO INŽENÝRSTVÍ

INSTITUTE OF PHYSICAL ENGINEERING

ÚSTAV FYZIKÁLNÍHO INŽENÝRSTVÍ

ELECTRON MICROSCOPY AND SPECTROSCOPY OF NANOPHOTONIC STRUCTURES AND MATERIALS

ELEKTRONOVÁ MIKROSKOPIE A SPEKTROSKOPIE NANOFOTONICKÝCH STRUKTUR A MATERIÁLŮ

MASTER'S THESIS

DIPLOMOVÁ PRÁCE

AUTHOR — Bc. Rostislav Řepa

AUTOR PRÁCE

SUPERVISOR — doc. Mgr. Vlastimil Křápek, Ph.D.

VEDOUCÍ PRÁCE

BRNO 2024

VYSOKÉ UČENÍ TECHNICKÉ V BRNĚ
FAKULTA STROJNÍHO INŽENÝRSTVÍ

Zadání diplomové práce

Ústav:	Ústav fyzikálního inženýrství
Student:	**Bc. Rostislav Řepa**
Studijní program:	Fyzikální inženýrství a nanotechnologie
Studijní obor:	bez specializace
Vedoucí práce:	**doc. Mgr. Vlastimil Křápek, Ph.D.**
Akademický rok:	2023/24

Ředitel ústavu Vám v souladu se zákonem č.111/1998 o vysokých školách a se Studijním a zkušebním řádem VUT v Brně určuje následující téma diplomové práce:

Elektronová mikroskopie a spektroskopie nanofotonických struktur a materiálů

Stručná charakteristika problematiky úkolu:

Nanofotonické struktury jsou objekty s rozměry typicky v desítkách až stovkách nanometrů, které interagují s externí světelnou vlnou a modifikují její vlastnosti. Umožňují tak řadu fyzikálně významných aplikací, například silnou lokalizaci a zesílení světla pomocí plazmonických antén pro prostorově závislé zesílení optických procesů nebo fokusaci světla ultratenkým metapovrchem s funkcí čočky.

Vlastnosti nanofotonických struktur jsou úzce spjaté s jejich tvarem, velikostí, chemickým složením, krystalinitou, případně přítomností defektů a kontaminace. Dále se v přípravě nanofotonických struktur uplatňují nové materiály, například materiály s laditelnými vlastnostmi, u nichž je důležité porozumět vlastnostem materiálu a jejich změnám při přípravě nanostruktury z objemového materiálu nebo tenké vrstvy. Zmíněné významné vlastnosti nanostruktur a materiálů mohou být s výhodou studovány technikami elektronové mikroskopie a spektroskopie, která nabízí výborné prostorové rozlišení a dobré spektrální rozlišení.

Diplomová práce bude zaměřena na studium nanofotonických struktur nebo nových materiálů pro nanofotoniku pomocí metod elektronové mikroskopie a spektroskopie. Konkrétní téma bude vybráno podle zájmu studenta a zaměření školitele. Může jít například o zkoumání mechanismu plazmonického bleskosvodného jevu nebo o vlastnosti tepelně indukovaného fázového přechodu v oxidu vanadičitém.

Cíle diplomové práce:

Vybrat aktuální téma v oblasti výzkumu nanofotoniky a zvolit k němu metody elektronové mikroskopie a spektroskopie.

Podrobně prozkoumat vybrané téma zvolenými metodami, porozumět pozorování a navrhnout optimální použití struktury nebo materiálu v příslušných nanofotonických aplikacích.

Seznam doporučené literatury:

HOHENESTER, Ulrich. Nano and Quantum Optics. Cham: Springer International Publishing, 2020 [cit. 2021-11-22]. Graduate Texts in Physics. ISBN 978-3-030-30503-1. Dostupné z: doi:10.1007/978-3-030-30504-8

HORÁK, Michal, Kristýna BUKVIŠOVÁ, Vojtěch ŠVARC, Jiří JASKOWIEC, Vlastimil KŘÁPEK a Tomáš ŠIKOLA. Comparative study of plasmonic antennas fabricated by electron beam and focused ion beam lithography. Scientific Reports. 2018, 8(1), 9640. ISSN 2045-2322. Dostupné z: doi:10.1038/s41598-018-28037-1

Termín odevzdání diplomové práce je stanoven časovým plánem akademického roku 2023/24

V Brně, dne

L. S.

prof. RNDr. Tomáš Šikola, CSc. ředitel ústavu	doc. Ing. Jiří Hlinka, Ph.D. děkan fakulty

Abstract
The lightning-rod effect is a well-established principle in electrostatics, characterized by the generation of a strong electric field near the pointed features of a charged conductor. In the field of plasmonics, the influence of local curvature on the induced electric field around metal nanoparticles (plasmonic antennas) is similarly observed. Besides this so-called plasmonic lightning rod effect, other phenomena such as the charge reservoir of the plasmonic antenna, the surface wave localization, and the interaction between two plasmonic antennas also contribute to field enhancement. This thesis utilizes electron energy loss spectroscopy and electromagnetic simulations to quantitatively examine these distinct phenomena by isolating their partial contributions to the strength of the induced electric field around a plasmonic antenna.

Keywords
Plasmonic lightning-rod effect, localized surface plasmons, plasmonic antenna, charge reservoir, local curvature, electron energy loss spectroscopy

Abstrakt
Bleskosvodný jev je dobře známý princip elektrostatiky, který vyjadřuje vznik silného elektrického pole v blízkosti zakřivených částí nabitého vodiče. V oblasti plazmoniky je podobně pozorován vliv lokálního zakřivení na indukované elektrické pole v okolí kovových nanočástic (plazmonických antén). Kromě tohoto tzv. plazmonického bleskosvodného jevu přispívají k zesílení pole i další jevy, jako je rezervoár náboje plazmonické antény, lokalizace povrchové plazmonové vlny, nebo interakce mezi dvěma plazmonickými anténami. Tato práce využívá spektroskopii energiových ztrát elektronů a elektromagnetických simulací ke kvantitativnímu zkoumání těchto odlišných jevů tím, že izoluje jejich dílčí příspěvky k velikosti indukovaného elektrického pole v okolí plazmonické antény.

Klíčová slova
Plazmonický bleskosvodný jev, lokalizované povrchové plazmony, plazmonická anténa, rezervoár náboje, lokální křivost, spektroskopie energiových ztrát elektronů

ŘEPA, R. *Electron microscopy and spectroscopy of nanophotonic structures and materials.* Brno, 2024. 90 p. Master's Thesis. Brno University of Technology, Faculty of Mechanical Engineering. Supervisor doc. Mgr. Vlastimil Křápek, Ph.D.

I hereby declare, that I have written this thesis independently under the guidance of doc. Mgr. Vlastimil Křápek, Ph.D. All sources, references, and literature utilized during the preparation of this thesis are cited and listed in the complete reference.

Bc. Rostislav Řepa

I would like to express my gratitude to my supervisor doc. Mgr. Vlastimil Křápek, Ph.D. for his professional guidance, assistance in resolving challenges, and insightful recommendations and feedback. I am grateful to Ing. Michal Horák, Ph.D. for conducting the EELS measurements and for his essential advice on the operation of the TEM. Finally, I express my gratitude to my family for their continuous support throughout my academic career, including the completion of this thesis.

CzechNanoLab project LM2023051 funded by MEYS CR is acknowledged for the financial support of the measurements and sample fabrication at CEITEC Nano Research Infrastructure.

Bc. Rostislav Řepa

Contents

Introduction 3

1 Analytical Electron Microscopy 5
- 1.1 Electron-Specimen Interactions . . . 5
- 1.2 Transmission Electron Microscopy . . . 8
  - 1.2.1 Electron Gun . . . 10
  - 1.2.2 Electron Lenses . . . 11
  - 1.2.3 Illumination System . . . 13
  - 1.2.4 Imaging System . . . 14
  - 1.2.5 Detectors and Spectrometers . . . 17
- 1.3 Electron Diffraction, Imaging and Analytical Techniques . . . 19
  - 1.3.1 Electron Diffraction . . . 19
  - 1.3.2 Imaging . . . 23
  - 1.3.3 Energy Dispersive X-Ray Spectroscopy . . . 27
  - 1.3.4 Electron Energy Loss Spectroscopy . . . 28

2 Nanophotonics 33
- 2.1 Electromagnetic Field in Materials . . . 33
- 2.2 Optical Properties of Materials . . . 34
  - 2.2.1 The dipole oscillator (Drude-Lorentz) model . . . 34
  - 2.2.2 Bulk Polaritons . . . 37
  - 2.2.3 Surface Plasmon Polariton . . . 39
  - 2.2.4 Localized Surface Plasmon . . . 42
- 2.3 Computational Methods in Plasmonics . . . 44
  - 2.3.1 Metallic Nanoparticle Boundary Element Method . . . 45

3 Plasmonic Lightning-Rod Effect 49
- 3.1 Introduction . . . 49
- 3.2 Methodology . . . 51
  - 3.2.1 Fabrication of Plasmonic Antennas . . . 51
  - 3.2.2 Structural and Elemental Characterization . . . 53
  - 3.2.3 Electron Energy Loss Spectroscopy Measurements . . . 56
  - 3.2.4 Theoretical Modeling . . . 59
- 3.3 Task 1: Charge Reservoir . . . 62
  - 3.3.1 Design of Plasmonic Antennas . . . 63
  - 3.3.2 Electron Energy Loss Spectroscopy . . . 64
  - 3.3.3 Induced Electric Field . . . 67
  - 3.3.4 Discussion . . . 70
- 3.4 Task 2: Local Curvature . . . 73
  - 3.4.1 Design of Plasmonic Antennas . . . 73
  - 3.4.2 Electron Energy Loss Spectroscopy . . . 74
  - 3.4.3 Induced Electric Field . . . 77
  - 3.4.4 Discussion . . . 79

Conclusions and Outlook 81

References 83

List of abbreviations 89

Introduction

Analytical electron microscopy (AEM) is currently one of the most prominent techniques utilized in materials science and nanotechnology. It integrates the transmission electron microscopy (TEM) with analytical techniques such as electron energy loss spectroscopy (EELS) and energy dispersive X-ray spectroscopy (EDS). Collectively, these techniques provide a powerful tool for studying the chemical composition, electronic structure, and crystallographic properties of the sample at the nanoscale. In this thesis, we utilize AEM to study the structural and optical properties of metal nanophotonic structures, the so-called plasmonic antennas.

Nanophotonic structures are objects with dimensions typically in the tens to hundreds of nanometers that interact with an external light wave and modify its properties. Nanophotonics is a scientific discipline that deals with such light-matter interactions [1, 2]. Plasmonics is a subfield of nanophotonics concerned with the interaction of light with metals [3]. The coupling between the electromagnetic field and free electrons in metals at the metal-dielectric interface leads to the formation of the so-called surface plasmon polaritons (SPP). SPPs are electromagnetic evanescent waves propagating along the metal-dielectric interface connected to oscillations of surface charges. The amplitude of this wave decreases exponentially in both media, resulting in its spatial localization on the surface of the metal. In the case of spatially restricted interfaces, such as metal nanoparticles (plasmonic antennas, PAs), the so-called localized surface plasmons (LSP) can be excited. A significant feature of LSP is a strong enhancement of the electromagnetic field in the vicinity of PAs, accompanied by its confinement to subwavelength dimensions [4, 5].

The lightning rod effect is a well-known phenomenon in electrostatics characterized by the formation of a strong electric field near the sharp features of a charged conductor. Similarly, PAs are expected to produce particularly strong electromagnetic fields around their features with high curvature. This aspect is evident in meticulous designs of plasmonic structures applied in areas such as enhanced photoluminescence [6], surface-enhanced Raman scattering [7, 8], and strong light-matter coupling [9]. However, this so-called plasmonic lightning-rod effect (PLRE) is not rigorously understood, although various innovative studies have explored its particular aspects [10, 11].

Importantly, the field enhancement in plasmonics stems from additional contributions besides the local curvature, including the evanescent nature of surface plasmon polaritons or the magnitude of the induced charge for a specific excitation. Despite the fact that the plasmonic lightning rod effect (PLRE) is widely utilized, its understanding is mostly intuitive, and so is the design of plasmonic antennas for specific applications. A comprehensive description of the PLRE fundamentals, which would enable a guided design of plasmonic antennas and optimization of their performance, is missing.

In this thesis, we employ EELS along with numerical electromagnetic simulations to examine these distinct effects by isolating their partial contributions to the strength of the induced electric field. Chapter 1 discusses various experimental techniques employed for the structural and elemental analysis of plasmonic antennas within the context of the entire AEM instrument's operation. Chapter 2 covers the basics of electromagnetic theory related to localized surface plasmons and their numerical simulations using the boundary element method. In Chapter 3, we provide our investigation of the plasmonic lightning-rod effect. The initial section focuses on introducing the various phenomena that can impact

the strength of the induced fields during LSP excitation. Following that, we outline the research methodology, which encompasses the fabrication of plasmonic antennas, their structural and elemental analysis, as well as EELS measurements and data processing. In the subsequent two studies, we examined the influence of the charge reservoir and the effect of local curvature on the induced electric field, isolating these effects from other contributions.

1 Analytical Electron Microscopy

Analytical electron microscopy (AEM) is a powerful technique that offers a wide range of applications in the field of material characterization at the nanoscale. Using electrons as a probe not only has an advantage in the possibility of achieving very high spatial resolutions, but also in the prospect of generating various secondary signals that carry information on the chemical composition, electronic structure, or crystallographic properties of the specimen. In this chapter, AEM is introduced in the context of this thesis as a tool for experimental characterization of nanophotonic structures. In particular, in Section 1.1 electron-specimen interactions and the generation of secondary signals are summarized. In Section 1.2, the functionality of the individual components of the transmission electron microscope (TEM) is briefly described. Section 1.3 introduces the most important analytical TEM techniques used later in this thesis.

1.1 Electron-Specimen Interactions

In a typical scenario in TEM, high-energy electrons traverse a thin solid specimen and interact with its atoms, resulting in electron scattering. During these scattering events, electrons may undergo a change in their momentum (resulting into their deviation from their incident direction) and energy. Scattering can be divided into two main categories: *elastic*, where the energy exchange between incident electrons and the specimen can be neglected, and *inelastic*, where some part of the energy of incident electrons is transferred to the specimen. The interactions between the electron beam and the specimen are often accompanied by the production of a wide range of secondary signals. Some of them are illustrated in Fig. 1.1.

Elastic scattering occurs as a result of Coulomb interactions between the incident electrons and the high concentration of positive charge of the atomic nucleus. Some incident electrons travel in the vicinity of the nucleus, where they experience intense electric fields and are scattered through large angles (Rutherford scattering)[1]. Electrons scattered to angles exceeding 90° are referred to as backscattered electrons (BSE) and are widely utilized in scanning electron microscopy (SEM) for their sensitivity in the atomic number Z of the studied specimen offering material (Z) contrast. However, in TEM, this signal is not very useful due to the limited thickness of the observed samples, and thus smaller BSE yields, and the possibility of using much more convenient quantitative spectroscopy techniques for material analysis (like energy-dispersive X-ray spectroscopy or electron energy loss spectroscopy).

Most of the incident electrons travel further away from the atomic nuclei, where its electrostatic field is much weaker and also partially screened by the surrounding electron cloud, and thus they are scattered only through small angles (10-100 mrad). These electrons are the main contributors to the image contrast and are therefore used in the main TEM imaging techniques, dark field (DF) and bright field (BF) imaging. If we consider scattering on periodic structures (crystals), the wave nature of electrons cannot be ignored because of the interference effects of the scattered waves. This collective scattering

[1] The theory of high-angle elastic scattering on atomic nuclei was developed by Ernest Rutherford in 1911 to explain the well known gold foil experiment performed by him and his student Ernest Marsden in 1909. The experiment led to the proposal of a new model of the atom, known as the Rutherford model.

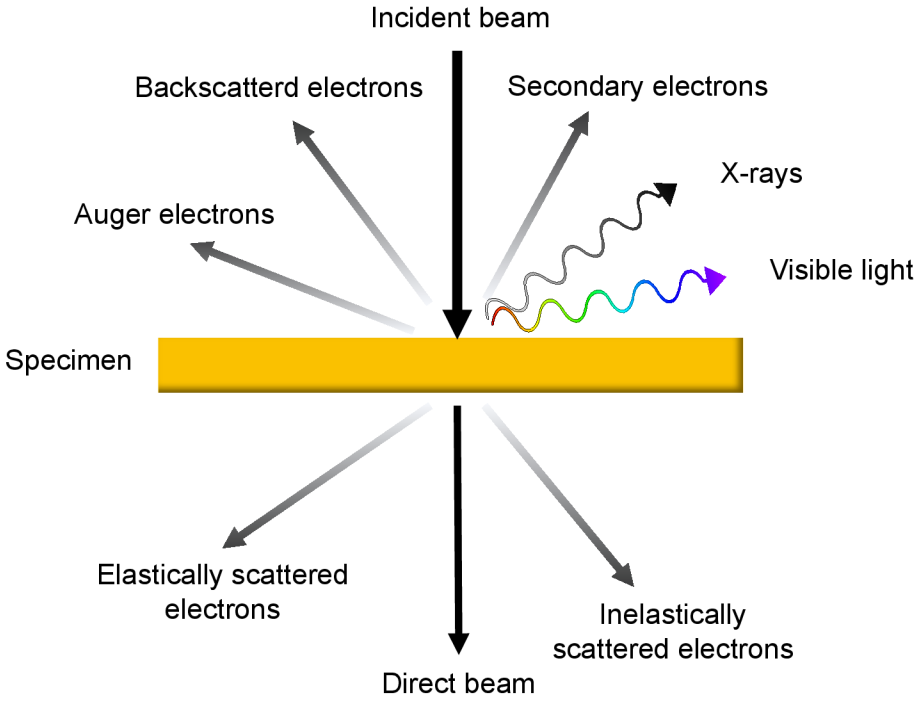

Figure 1.1: Signals generated during the electron-specimen interactions. Adapted from [12].

of electrons on atomic planes is known as *diffraction*. The observed angular distribution of electron intensity consists of distinct (diffraction) peaks carrying information on the interplanar spacing and the symmetry of the crystal which make diffraction an invaluable technique for the crystallography characterization of the specimen. Diffraction and imaging will be covered in more detail in Section 1.3.1.

In AEM, inelastically scattered electrons (also known as energy-loss electrons) are equally important as the elastically scattered ones. During inelastic scattering, a part of the kinetic energy of the incident electron is converted into atom-electron excitations, which can be studied using electron energy loss spectroscopy (EELS). Some of the possible excitation mechanisms, as well as the de-excitation processes associated with the generation of secondary signals, are depicted in the energy level diagram in Fig. 1.2.

An electron can be excited from an inner shell (K, L, M, etc.) to an unoccupied energy state above the Fermi level, or it can leave the atom entirely when the transferred energy surpasses its binding energy. The excited electron leaves behind a vacant hole that is quickly filled by an outer-shell electron or another core-shell electron with a lower binding energy. The energy released during the de-excitation process can be emitted in the form of X-rays or it can be absorbed by another inner- or outer-shell (Auger) electron, which is afterwards ejected from the specimen. In both of these cases, the energy of the emitted X-rays or the kinetic energy of the Auger electron is dependent on the electronic structure of the atom (characteristic to the atom). Therefore, these signals carry information about the elemental composition of the sample. The spectroscopies employing these signals are referred to as Auger electron spectroscopy (AES) and energy-dispersive X-ray spectroscopy (EDS), which is described in more detail in Section 1.3.3.

When the incident beam interacts with an outer-shell electron, it can induce an intraband or interband excitation. Interband (between two different bands) excitations are particularly important in the case of semiconductors where the generated electron-hole

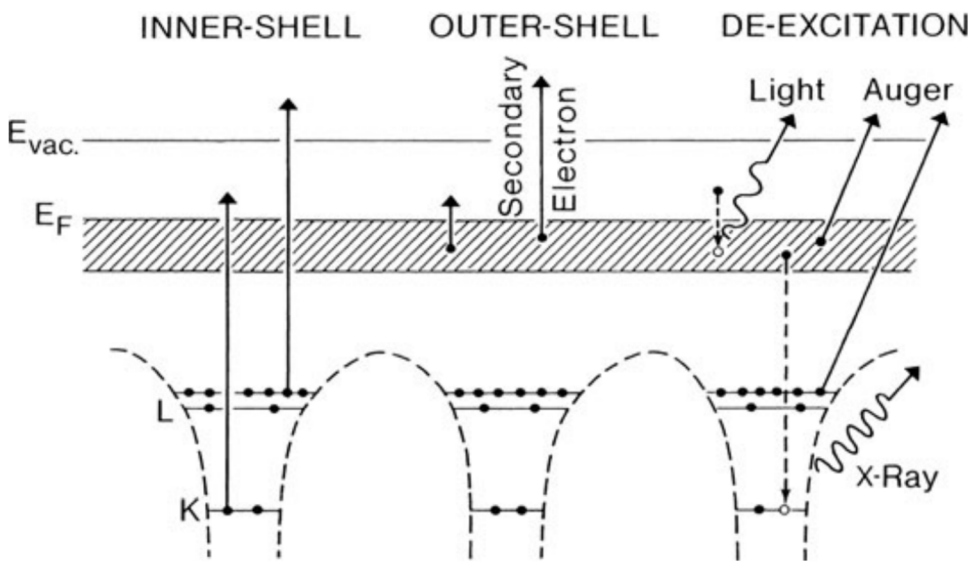

Figure 1.2: Energy-level diagram of a solid representing inner-shell and outer shell excitations originating in electron-specimen interactions (on the left) and possible secondary signal generation during the de-excitation processes (on the right). Taken from [13].

pairs can be studied to provide information about the electronic properties of the specimen, such as the type of the band gap (direct or indirect), its energy, and impurity effects. Electron-hole pairs can be separated by an internal bias, and then this electron-beam-induced current (EBIC) can be measured through a picoammeter. When an electron-hole pair recombines, the released energy can be emitted in the form of a photon (often in the infrared, visible, or ultraviolet region) and detected by cathodoluminescence (CL) spectroscopy. When the transferred energy to the outer-shell electron exceeds its binding energy, the electron is emitted from the specimen. The emitted electrons with the energy below 50 eV are denoted as secondary electrons and are used mainly in SEM to form images sensitive to the surface topology of the specimen.

Beside the single-electron excitations discussed so far, inelastic scattering also includes collective excitations, such as phonons and plasmons. Phonons are collective oscillations of atoms in an atomic lattice (lattice vibrations), and plasmons are longitudinal collective oscillations of free (or weakly bound) electrons, which occur predominantly in metals. These phenomena will be discussed in detail in Chapter 2.

Finally, in addition to all the valuable signals produced during the electron-specimen interactions, the electron beam can cause undesirable damage to the specimen (bond breaking, lattice defects, sputtering of atoms, etc.). This is a major problem in TEM where high-energy electrons (hundreds of keV) are used to probe the sample, which after the exposure may no longer represent the original chemistry and structure of the material. Consequently, low-dose, low-energy, and ultrafast electron microscopy techniques have been developed to reduce beam damage while maintaining considerable signal yield and spatial resolution.

1.2 Transmission Electron Microscopy

In a transmission electron microscope (TEM), we use a high-energy electron beam to image the sample under study. The microscope consists of the following parts: electron gun (further described in Section 1.2.1), electron lenses (Section 1.2.2) utilized in the illumination system (Section 1.2.3) and imaging system (Section 1.2.4), and detectors (Section 1.2.5). A simplified schematic of the microscope is shown in Fig. 1.3.

The electron beam is produced in an electron gun, which can operate on the basis of thermionic emission, field emission, or a combination of the two, Schottky emission. The beam is gradually accelerated by accelerators to high energies of the order of hundreds of keV. The monochromator can be implemented to reduce the distribution width of the kinetic energies of primary electrons produced by the electron gun, leading to improved spectral resolution in EELS.

The electron beam is formed and shaped by the electromagnetic fields of the individual microscope components. They include the lenses that can focus the electron beam and create an image of the specimen. The electron beam is shaped by a set of condenser lenses before hitting the sample. By changing their excitation, TEM can be operated in two basic imaging modes. The first is conventional TEM, which uses a parallel electron beam. The second is the scanning TEM (STEM) mode, which uses a convergent beam focused into a small spot (called a probe), which is scanned across the sample using scan coils, and the resulting image of the sample is produced point by point.

Since electron lenses suffer from large aberrations (mainly spherical), the beam is spatially limited by apertures, so that only electrons near the optical axis, where the aberrations are less severe, are transmitted through the column of the microscope. To reduce aberrations, TEM can be equipped with spherical aberration corrector in the electron column either before the beam hits the sample as in Fig. 1.3 (probe Cs corrector) or after the sample (image corrector), but these solutions are very expensive and are used mainly for high-end instruments, which can achieve sub-angstrom spatial resolution [14]. Due to the manufacturing inaccuracies of individual components, it is also necessary to include deflectors and stigmators in the microscope, which are not shown in the schematic for simplicity.

The specimen is mounted in the specimen holder (stage) and placed directly inside the electromagnetic field of the objective lens. This naturally divides it into an objective prefield, which can be considered as the last lens of the illumination system, and the extent of the field referred to as objective lens is responsible for the creation of the first image and thus for the quality of the transferred information about the specimen. The objective aperture is located in the back focal plane (BFP) of the objective lens and is mainly used in conventional TEM imaging to increase the contrast of the image (bright field and dark field). The selected area aperture is located in the image plane of the objective lens and is used mainly for selected area electron diffraction (SAED). The EDS detector collecting X-rays produced during the deexcitation of the sample is positioned near the sample in order to collect as much of the X-ray power as possible.

A projector system typically consists of four lenses, a diffraction lens, an intermediate lens, and two projector lenses. The system is designed to magnify the image produced by the objective lens onto the detector. For the STEM mode, bright field and annular dark field detectors are important, detecting electrons scattered at different angles. A spectrometer consisting of a magnetic prism can be attached below the electron column.

The magnetic field then spatially separates the incoming electrons with different velocities according to the Lorentz force. The CCD camera can then capture energy-filtered images and diffraction patterns (EFTEM) or energy-loss spectra (EELS).

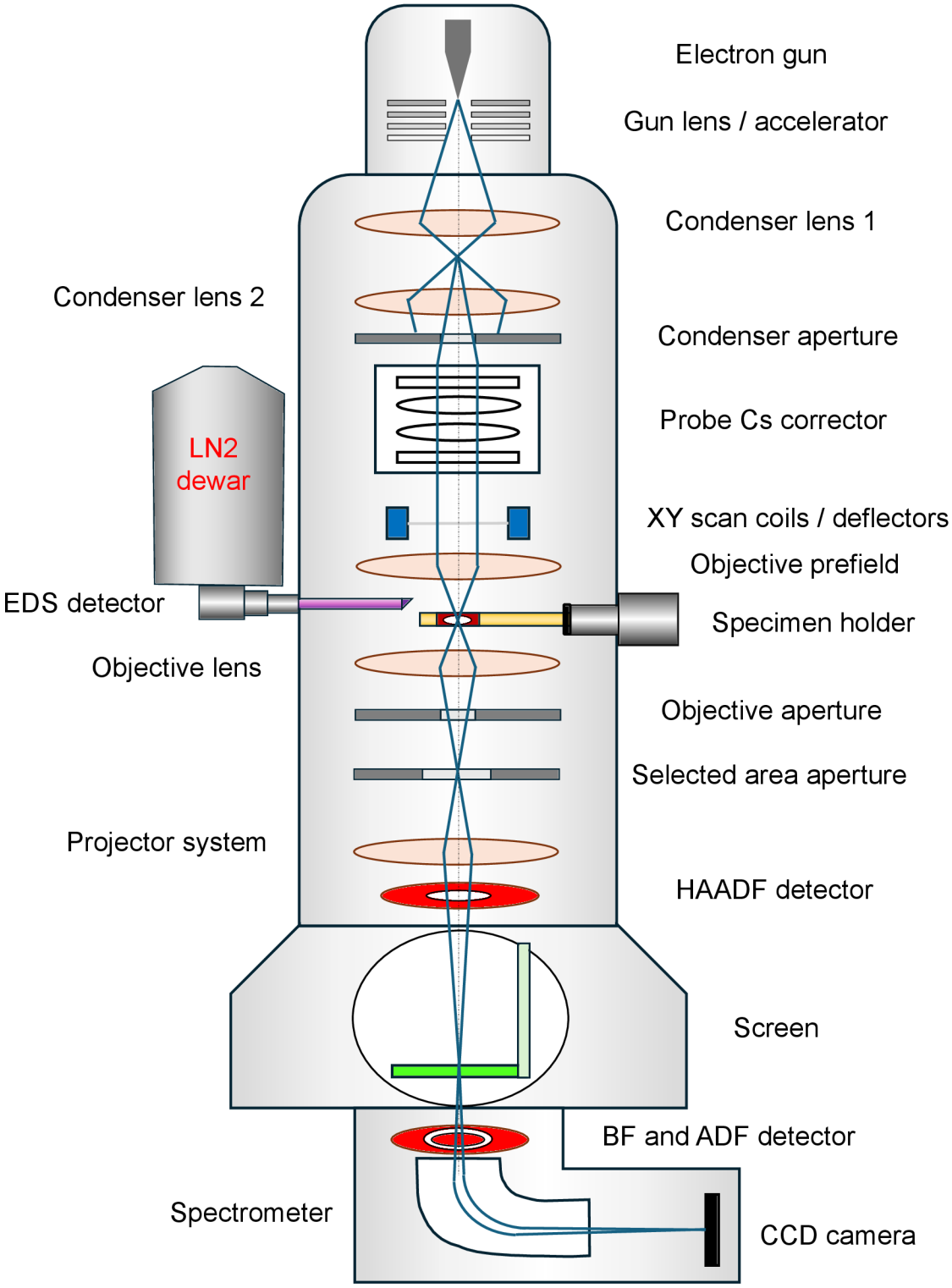

Figure 1.3: Schematic illustration of a modern analytical electron microscope, its primary optical elements and possible add-ons for analytical techniques such as EDS and EELS.

1.2.1 Electron Gun

Electron guns are used as a source of electron illumination in TEM. The quality of the electron source has a direct impact on the acquired images and spectra, and therefore the electron gun is one of the most important parts of a TEM. Electrons can be emitted from the cathode into the vacuum by overcoming its potential barrier, which is known as the work function. Because the emission of electrons would cause charging, metals are used as cathodes because of their high electrical conductivity. There are three main types of electron gun according to the type of electron emission: thermionic emission, Schottky emission, or cold field emission guns (cold FEG), illustrated in Fig. 1.4.

In the case of thermionic electron guns, the cathode needs to be heated to high temperatures, so that some part of the conduction electrons reaches a kinetic energy sufficient to surpass the work function of the material. For most metals, the operating temperature of the thermionic emission exceeds their melting point. However, tungsten stands out as an exception, with an operating temperature of approximately 3000 K (below its melting point of 3650 K). Another option is lanthanum hexaboride (LaB_6), which has a lower work function and can operate at temperatures up to 2000 K. The work function of the material can be reduced by the application of an external electric field (Schottky effect). This effect is utilized in Schottky FEG, where a sharp tungsten tip (less than 1 µm in radius) is coated with ZrO to further reduce the work function. Similarly, as in the case of thermionic sources, electrons still have to overcome the potential barrier by their kinetic energy, which is achieved by heating the cathode. In the case of cold FEG, electrons are extracted in a different way, via electron tunneling. This is made possible even at room temperature by employing a very sharp tip with radius reduced below 0.1 µm creating strong electric fields in its vicinity ($E \geq 10^9$ Vm^{-1}).

The electron beam is characterized by the source brightness given by the current density per unit solid angle, crossover diameter, emission current, energy spread, operating temperature, etc. The typical values of these parameters for the discussed types of electron

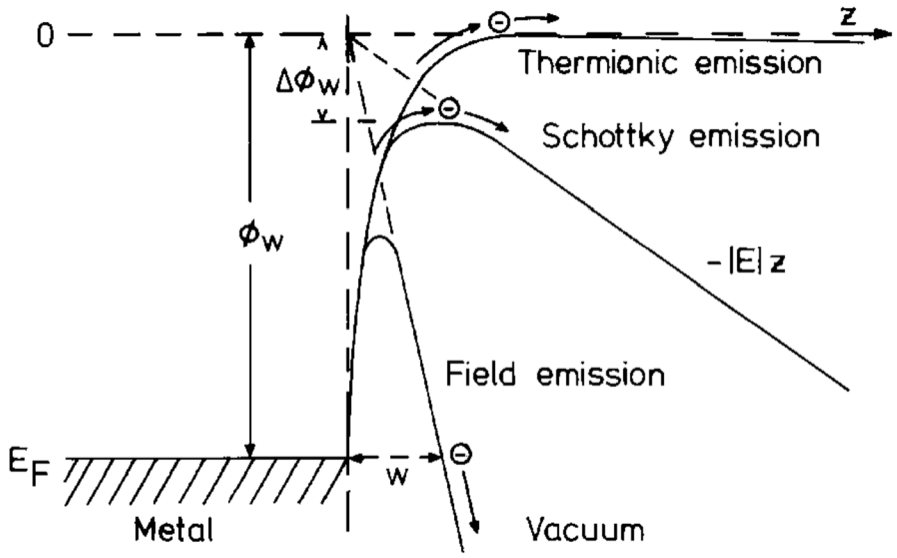

Figure 1.4: Illustration of the three main types of electron emission: thermionic, Schottky and field emission. Taken from [15].

Table 1.1: Characteristics of the electron sources. Taken from [12]

Characteristic	Tungsten	LaB_6	Schottky FEG	Cold FEG
Work function (eV)	4.5	2.4	3.0	4.5
Operating temperature (K)	2700	1700	1700	300
Current density (A/m^2)	5	10^2	10^5	10^6
Crossover size (nm)	$> 10^5$	10^4	15	3
Brightness (A/m^2sr)	10^{10}	5×10^{11}	5×10^{12}	10^{13}
Energy spread (eV)	3	1.5	0.7	0.3
Emission current stability (%/hr)	< 1	< 1	< 1	5
Vacuum (Pa)	10^{-2}	10^{-4}	10^{-6}	10^{-9}
Lifetime (hr)	100	1000	> 5000	> 5000

guns are listed in Table 1.1. In AEM, well-defined small probes with high current, high spatial and temporal coherence (small source size and energy spread), and high emission stability are required to optimize both spatial resolution and analytical sensitivity. Taking into account the source characteristics in Table 1.1, thermionic sources are not a good choice for AEM but can still perform better at low magnifications, where FEGs exhibit low current density due to small source sizes, and the relatively low vacuum requirements make microscope operation cheaper. Schottky FEGs offer much higher brightness and coherence than thermionic sources, as well as a smaller energy spread and a better lifetime, making them a common choice for AEM. However, to obtain the best possible AEM performance, cold FEGs are the electron source of choice for state-of-the-art instruments.

1.2.2 Electron Lenses

In electron microscopy, electromagnetic fields are used to control the trajectories of electrons that traverse the electron column through the Lorentz force $\mathbf{F}_\mathrm{L} = -e(\mathbf{E} + \mathbf{v} \times \mathbf{B})$, where e is the elementary charge, $\mathbf{E}$ is the electric field, $\mathbf{v}$ is the velocity of the electron and $\mathbf{B}$ is the magnetic field. Electromagnetic fields can be designed for the specific purpose of an individual TEM component. Deflectors are used to shift and tilt the electron beams, electric and magnetic multipoles are included to correct for aberrations such as astigmatism, magnetic prism can be utilized in the spectrometer or monochromator to disperse electrons with different energies. But most importantly, it has been shown already in 1927 by Busch that electron beams can be focused by magnetic or electrostatic electron lenses [16]. Electrostatic lenses are often used in electron guns or ion optics [15]. Magnetic lenses are more efficient in focusing the high-energy electron beam and also produce lower aberrations [17], making them the preferred choice for most TEM instruments.

The magnetic lens (Fig. 1.5) consists of a coil of copper wire, which is responsible for the generation of the magnetic field as an electric current flows through it. The coil is enclosed by a magnetic loop with a hole in its center called the bore. The magnetic loop is made of soft iron with high permeability to keep the magnetic field within the loop, except for the polepiece gap, where the magnetic field is highly concentrated and through which it is brought to the optical axis, where it acts as a lens for the incoming electrons. The magnetic field must be strong enough to be able to focus the electron beam in a short

distance and also rotationally symmetric as much as possible to obtain a uniform focus. To provide strong magnetic fields, high currents have to be used, causing resistive heating of the coil. For this reason, magnetic lenses have to be cooled with a water circuit.

Note that the magnetic field inside the lens has axial B_z and radial B_r components. If we consider an electron traversing the magnetic lens parallel to the optical axis, it can only be affected by B_r through the Lorentz force, generating a polar velocity of the electron. The polar component of velocity has a non-zero vector product with the axial magnetic field resulting into radial Lorentz force which bends the electron toward the optical axis. As a result, electrons can be focused by the magnetic lens but follow complicated helical trajectories. This also means that the created images or diffraction patterns can be rotated compared to the studied object, and this can cause problems with the image interpretation. Electrons can be traced using advanced software such as Electron Optical Design (EOD) [19], which helps design new magnetic lenses with improved performance for specific applications. The exact electron trajectories are not important for understanding the TEM operation and thus the electron paths will be represented in the text by simplified ray diagrams.

A big advantage of a magnetic electron lens is that its focal distance can be adjusted simply by changing the excitation strength (current in the coil) of the lens. This allows for a variety of illumination possibilities (different spot sizes, convergence angles, etc.), imaging modes (TEM, STEM, diffraction) or magnifications, as will be discussed in the following sections.

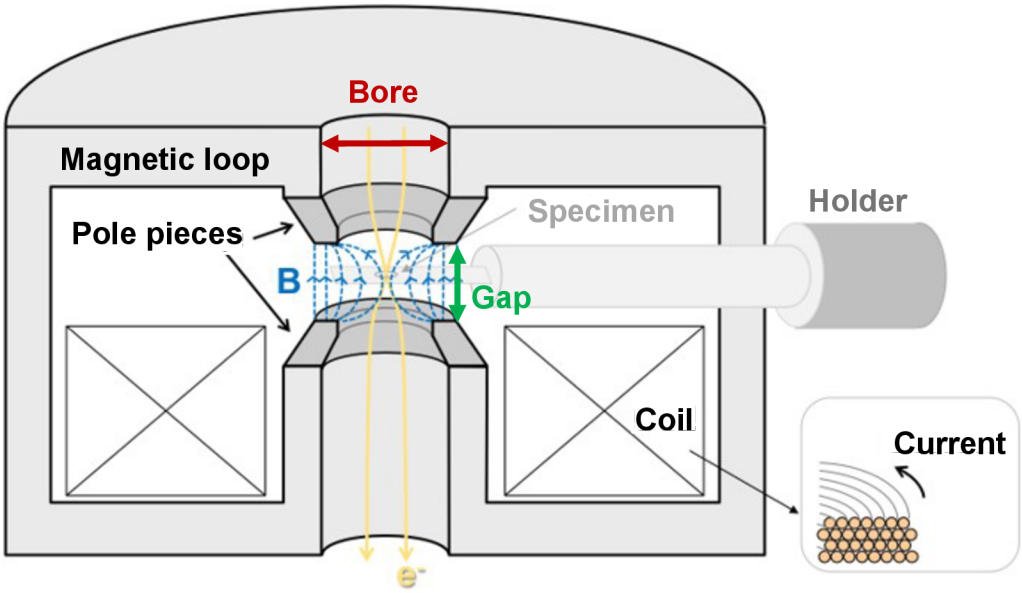

Figure 1.5: A schematic diagram of a magnetic lens. Magnetic field is generated by the current flowing inside the copper coils and brought to the optical axis through the pole pieces. The field is rotationally symmetric, very strong inside the gap and it gradually decreases towards the optical axis. This causes the focusing effect on the electron beam; the further away from the optical axis the electrons are traveling, the more they are deflected. Adapted from [18]

1.2.3 Illumination System

The main goal of the illumination system of a TEM/STEM instrument is to transfer electrons from the electron gun crossover to the specimen and to form an electron beam with specific properties to achieve the desired illumination conditions. To address the need for illumination variability, at least two condenser lenses are used in combination with the objective prefield. For simplicity, let us initially consider the setup consisting of only two condenser lenses, namely condenser lens 1 (C1) and condenser lens 2 (C2) and the objective prefield, as depicted in Fig. 1.6.

The C1 lens is used to image and, in most cases, to demagnify the electron gun crossover to the object plane of the C2 lens (C1 crossover) in order to obtain small electron probes. By changing the excitation of the C1 lens, the image position of the gun crossover changes as well as its demagnification. In this way, one can control the size of the electron probe (often referred to as spot size or spot number) and the beam current.

The excitation of the C2 lens, and thus its focal distance, is varied together with the condenser aperture to control the electron beam. This enables, for example, to switch between the parallel beam illumination, which is used in conventional TEM imaging and diffraction, and the convergent beam illumination, which is used in STEM or convergent beam electron diffraction (CBED).

In TEM mode (Fig. 1.6 on the left), the C2 lens projects the C1 crossover into the front focal plane (FFP) of the objective prefield, ensuring that a parallel electron beam is

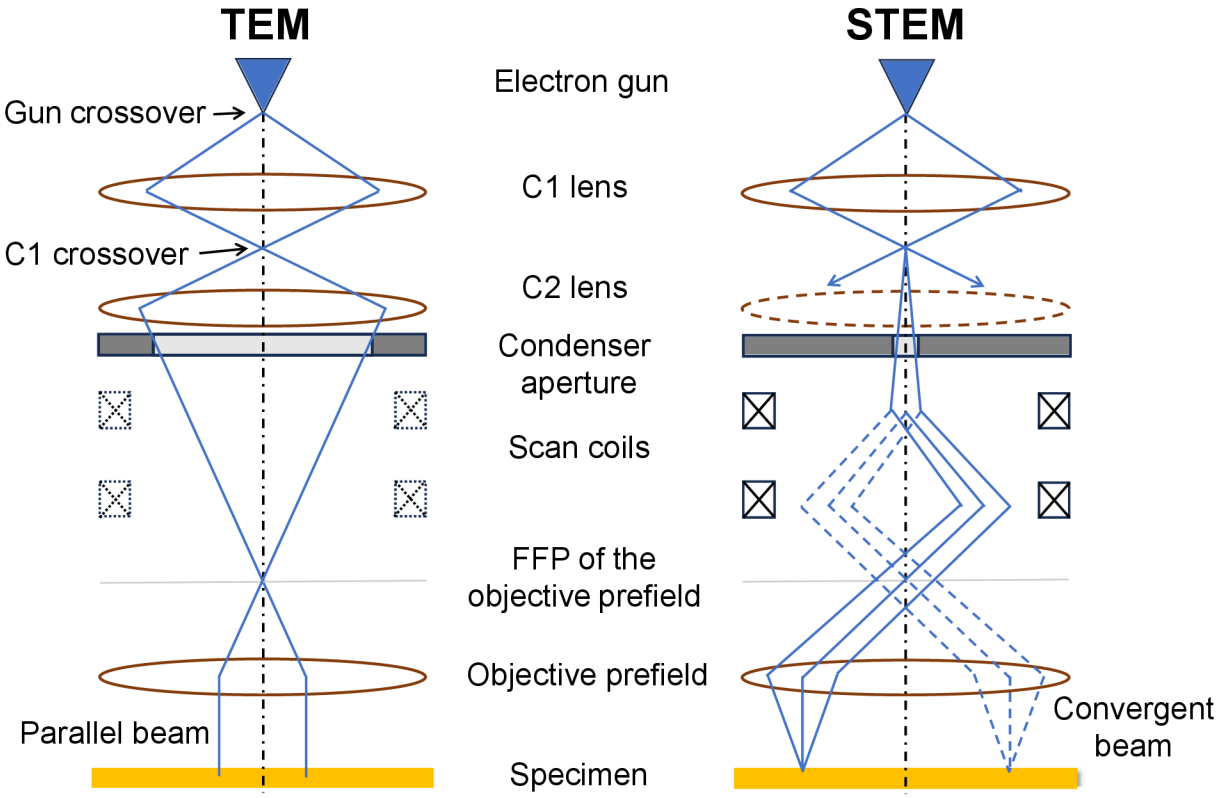

Figure 1.6: A schematic diagram of a two-lens condenser system combined with an objective prefield. Parallel beam illumination (TEM mode, on the left) or convergent beam illumination (STEM mode, on the right) can be achieved by changing the strength of the C2 lens. In STEM, the electron beam is scanned over the sample using scan coils.

produced. Rather large condenser apertures are used to maintain enough beam intensity on the specimen.

In STEM mode (Fig. 1.6 on the right), the C2 lens is only weakly excited and a smaller condenser aperture is used. In this case, the electron gun crossover is strongly demagnified in two steps by the C1 lens and the objective prefield to produce a small electron probe which can be scanned over the specimen. Scanning is accomplished by using two sets of scan coils (deflectors), which are situated between the condenser aperture and the objective prefield. The electron beam is deflected twice by the scan coils (away from and toward the optical axis) to ensure that it always intersects the optical axis at the FFP of the objective prefield, which then brings it to the specimen running parallel with the optical axis. By changing the condenser aperture or the excitation of the C1 lens, one can control the size, current, or convergence angle of the probe.

The two-condenser-lens setup allows one to freely switch between TEM and STEM imaging modes just by changing the excitation of the C2 lens. However, illumination possibilities are still seriously limited, mainly due to the fixed excitation of the objective lens (to maintain the optical alignment and stability) and thus the position of its FFP, into which the beam often has to be focused or deflected. As a solution, modern TEM/STEM instruments use three condenser lenses and also include the so-called condenser minilens placed immediately above the objective lens. This opens up a variety of illumination possibilities and combinations of beam parameters such as spot size, beam current, or convergence angle, which are crucial to meet the different needs of TEM/STEM imaging, diffraction, and analytical techniques.

1.2.4 Imaging System

The TEM imaging system consists of the objective lens, which creates the first image and the diffraction pattern of the specimen, and a set of lenses of the projector system, which further magnify the image (or the diffraction pattern) and project it onto the screen, camera, or detector where it is recorded.

The objective lens is the most important lens in TEM because it produces the very first image of the sample. For this reason, high demands are placed on the precision of the manufacturing and the optical stability of the objective lens. It is an immersion lens, which means that the sample is inserted directly between the pole pieces of the lens. In the case of AEM, the pole pieces must be sufficiently far apart to allow the sample to rotate through large angles, which is important for crystal structure investigations using diffraction techniques. The sample is subjected to a strong magnetic field of the order of 2 T. Strong excitation of the objective lens results in short focal lengths in the order of a few millimeters, which results in an image magnification of 20 to 50 times.

A ray diagram depicting the formation of the image by the objective lens in TEM mode (parallel beam illumination) is shown in Fig. 1.7. The parallel rays are focused by the lens into its back focal plane (BFP), where the diffraction pattern (DP) of the sample is created. An objective aperture can be inserted into this plane to allow only electrons scattered in certain directions to pass through the projector system and form the final image. This is used mainly in TEM imaging techniques such as bright field (BF), dark field (DF), or high resolution TEM (HRTEM), which are described in more detail in Section 1.3.1. The resulting image is formed in the image plane of the objective lens. In this plane, a selector aperture (SAD) is inserted to allow only electrons from a specific

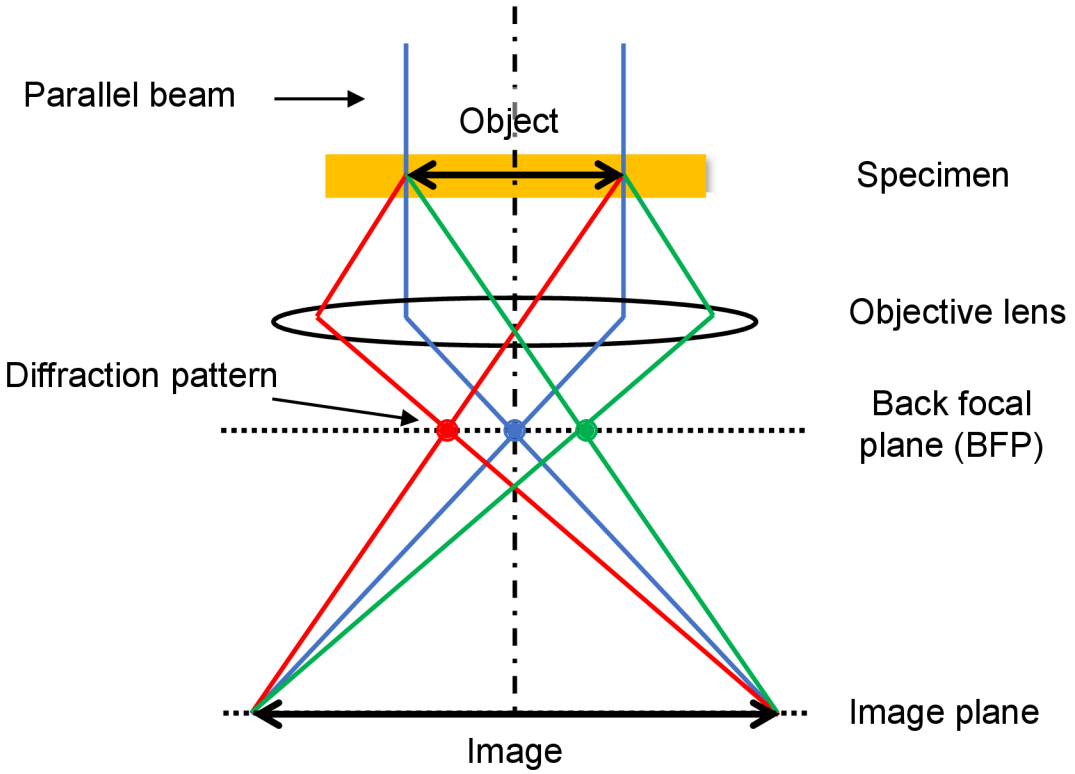

Figure 1.7: Ray diagram depicting the creation of the image (image plane) and the diffraction pattern (back focal plane) of the specimen by the objective lens for the case of parallel beam illumination.

area of the sample to pass through the projector system, which is used in a technique called selected area electron diffraction (Section 1.3.1).

The projection system typically consists of four lenses, namely the diffraction lens, intermediate lens, projection lens 1 and projection lens 2. By changing the excitation of the diffraction lens, its focal length varies and its object plane is shifted In this way, either the BFP or the image plane of the objective lens can be chosen to be projected onto the camera. The projector system is calibrated for a wide range of magnifications up to at least 500 000 times. It ensures that the image remains in focus and corrects any image rotation resulting from variations in the magnetic fields of the lenses when switching between magnifications and imaging modes.

In the case of the conventional TEM imaging mode, the diffraction lens is focused in the image plane of the objective lens, creating an intermediate image, which is then further magnified by the projection lenses and transferred to the camera (Fig. 1.8 left). For the TEM diffraction mode, the excitation of the diffraction lens is reduced, causing it to change focus to the BFP of the objective lens. In this case, the diffraction lens forms an intermediate DP of the sample, which is then projected onto the camera (Fig. 1.8 middle). In STEM mode, the specimen is illuminated with a convergent beam. Electrons are scattered to various directions and form a DP in the objective BFP. This plane is displayed by the projection system on the detector plane (Fig. 1.8 right). The transmitted electrons that were not elastically scattered (or scattered with small momentum transfer) are collected by the circular detector on the optical axis and form a bright field image of the specimen (hence the name BF detector). The scattered electrons at medium angles are projected onto the annular dark-field (ADF) detector, which produces a dark field image

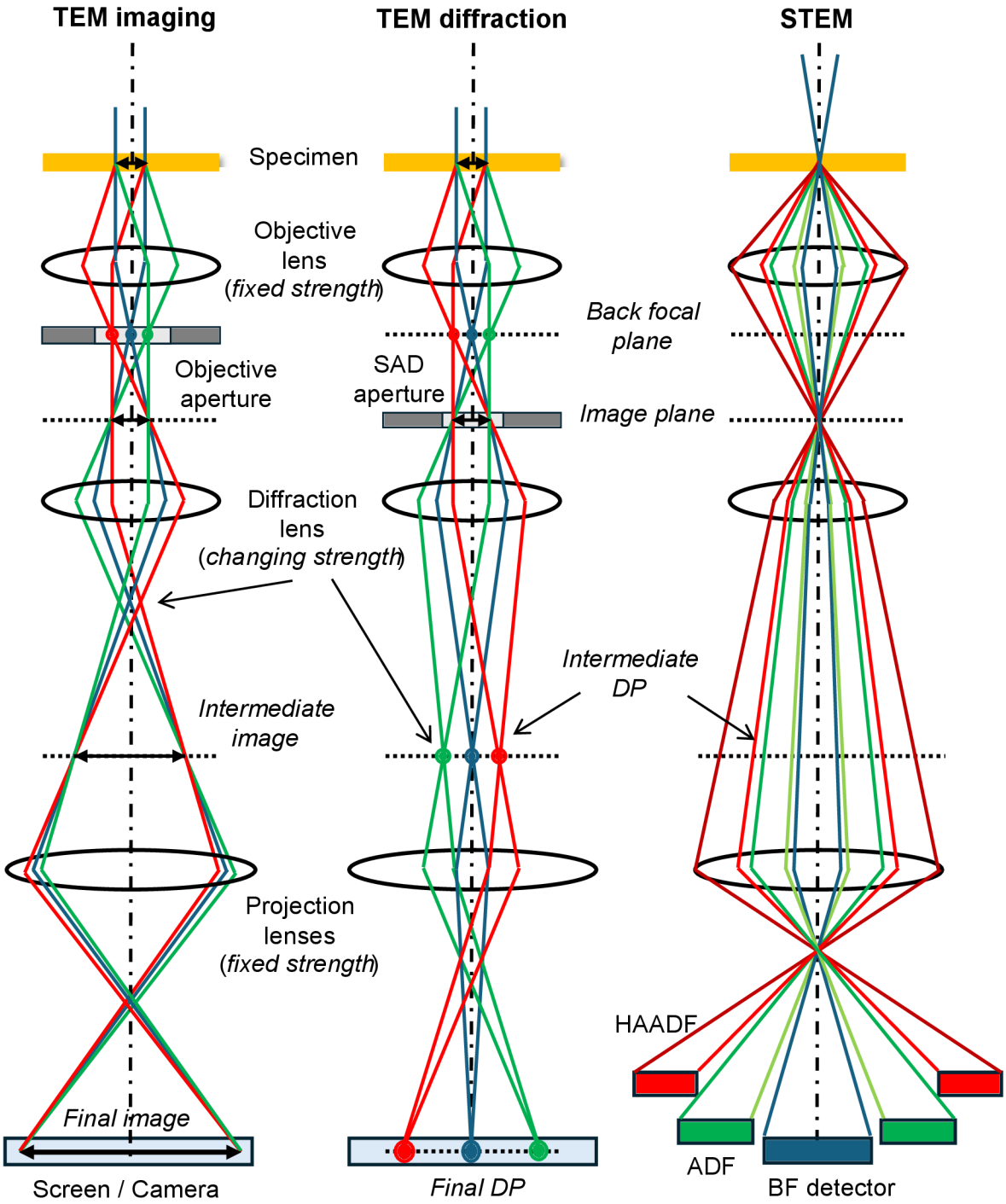

Figure 1.8: The basic operation modes of the TEM/STEM imaging system: TEM imaging projecting the image onto the screen (left), TEM diffraction projecting the DP onto the screen (middle), and STEM projecting the convergent beam DP onto the detector plane (right). In TEM, the switching between the modes can be done by changing the excitation of the diffraction lens. The other three projection lenses (here represented as one) further magnify the image or DP onto the screen. Note that the schematic is highly simplified to show the basic principles of imaging, the real instruments involve more lenses and imaging options. Adapted from [12].

of the sample with dominant diffraction contrast. Electrons scattered to high angles (Rutherford scattering dependent on the atomic number Z) are projected onto the high angle annular dark field (HAADF) detector and form a dark field image of the sample with material contrast.

1.2.5 Detectors and Spectrometers

Although human vision is not sensitive to electrons, some microscopes allow us to observe the sample directly on a fluorescent screen. It contains phosphorescent powders which emit visible light when illuminated by electrons in a process known as cathodoluminescence. The screen can also be recorded by a camera and observed on a computer monitor. However, the resulting image is not of sufficient quality for image recording and, therefore, is used primarily for alignments of the optical system. The advantage of the screen is that it can withstand the strong electron intensities commonly achieved during the alignment procedure.

For image recording, the so-called charge-coupled device (CCD) camera or the complementary metal-oxide semiconductor (CMOS) sensor are used. Both of these devices consist of a thin scintillator to convert the incoming electrons into photons, which are then transferred via fiber optics onto the pixelated CCD (or CMOS) sensor (direct electron exposure might cause damage to the sensors). In each pixel, photons are transformed into electrical signals (electron-hole pairs) by a photodiode, and the signal is further amplified and recorded (for more information, see [20]). Imaging sensors can easily be damaged by highly intense electron beams (mainly when acquiring diffraction patterns). For this reason, low exposure times, image stacking, and beam stoppers must be used when the camera is at risk of overexposure and damage.

In STEM, circular- or annular-shaped semiconductor or scintillation detectors are used to detect transmitted and scattered electrons at various angles (BF, ADF, HAADF detectors; see Fig. 1.8, right panel). The signal collected across the entire detector is integrated and recorded at each scanning point and displayed on the computer screen as a pixel of the corresponding intensity. The final image is formed point-by-point by scanning the electron probe over the sample. However, by integrating the signal, the information on the angular distribution of the electron scattering is lost. This can be solved by replacing conventional integrating STEM detectors with a pixelated direct detector, which allows recording of the entire convergent beam electron diffraction (CBED) pattern at each point of the scan [21]. Consequently, a four-dimensional (4D-STEM) data set is obtained from which not only the image of the specimen can be reconstructed, but also the mapping of the strain, phase, or crystal orientation can be performed [22].

Energy filtered imaging (EFTEM) and electron energy loss spectroscopy (EELS) are performed using an electron spectrometer which can be located either directly in the electron column (in-column filters) or below it (post-column spectrometers). A schematic illustration and a model of the post-column electron spectrometer developed by Gatan (GIF Quantum [23]) are shown in Fig. 1.9. The GIF spectrometer is equipped with a variable entrance aperture to select electrons that contribute to the spectra or filtered images. A key element of the GIF spectrometer is its 90 °magnetic prism. Within its magnetic field B, the incoming electrons with different kinetic energies (and velocities v) follow circular trajectories with the radius given by $R = (m/eB)v$. Therefore, the electrons are dispersed according to their energies, which in turn correspond to their

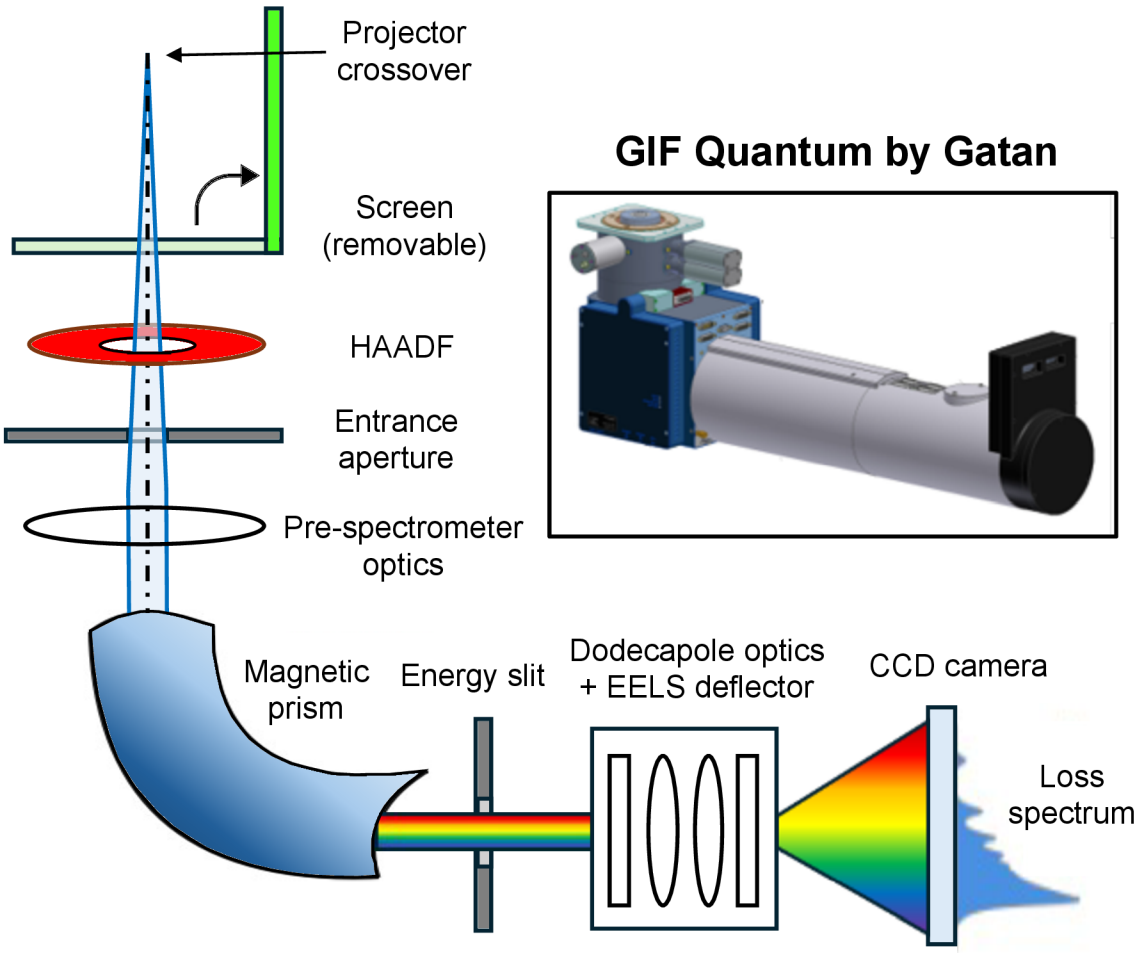

Figure 1.9: Schematic illustration and a model of a post-column electron spectrometer GIF Quantum developed by Gatan. The spectrometer can be operated in two modes: imaging and spectroscopy. In imaging mode (EFTEM), an energy-selecting slit is inserted into the dispersion plane of the spectrometer selecting an energy window of electrons that form the final energy filtered image on the camera. In the spectroscopy mode, the dodecapole optics projects the focused energy loss spectrum from the dispersion plane of the spectrometer onto the camera. Adapted from [23].

energy losses imposed by the interaction with the specimen. Electrons that suffered higher energy losses are deflected at higher angles (smaller R), forming an energy loss spectrum in the dispersion plane of the spectrometer. The energy slit can be placed in the dispersion plane of the spectrometer to provide energy filtering for EFTEM. Dodecapole optics is used to control the focus, magnification, and energy dispersion of the spectrum, as well as to correct for various aberrations. Loss spectra or energy filtered images are recorded by a CCD camera. Additional STEM detectors, such as HAADF, may be included. For a more detailed description of the EELS/EFTEM instrumentation, I refer to a textbook by Egerton [13].

Semiconductor X-ray detectors are used to detect X-rays generated during electron-specimen interactions. The EDS detector is placed directly above the specimen to collect as many X-rays as possible. The X-rays excite electrons from the valence band to the conduction band of the semiconductor, creating electron-hole pairs. The number of electron-hole pairs is proportional to the X-ray energy. Charges are separated via applied

bias voltage, generating charge pulses that are measured and processed by a computer. The most common X-ray detectors in AEM are silicon-based Si(Li) detectors, which need liquid nitrogen cooling and offer spectral resolutions around 140 meV, or silicon drift detectors (SDD) for high-speed X-ray spectrum imaging with improved spectral resolution [24].

1.3 Electron Diffraction, Imaging and Analytical Techniques

1.3.1 Electron Diffraction

When the sample is irradiated by an electron wave, a characteristic diffraction pattern is formed. From the analysis of the diffraction patterns, the sample crystallinity, crystal structure and its defects, lattice parameters, thickness, and many other parameters can be determined. For the understanding and interpretation of electron diffraction on crystals, it is important to introduce the concept of real and reciprocal crystal lattices. The periodicity of the crystal can be described by unit cell (basis) vectors **a**, **b**, and **c**. Each vector in the crystal lattice can be expressed as a linear combination of the basis vectors $\mathbf{r} = u\mathbf{a} + v\mathbf{b} + w\mathbf{c}$. In this coordinate system, the lattice planes are characterized by the Miller indices (hkl). Crystal lattice planes can also be represented by a vector $\mathbf{r}^*_{hkl}$ in the so-called reciprocal space as $\mathbf{r}^*_{hkl} = h\mathbf{a}^* + k\mathbf{b}^* + l\mathbf{c}^*$, where $\mathbf{a}^*$, $\mathbf{b}^*$, $\mathbf{c}^*$ are the primitive unit cell vectors of the reciprocal lattice. The relations between the real-space lattice vectors and the reciprocal-space lattice vectors are as follows

$$\mathbf{a}^* = 2\pi\frac{\mathbf{b}\times\mathbf{c}}{V_\mathrm{c}}, \qquad \mathbf{b}^* = 2\pi\frac{\mathbf{c}\times\mathbf{a}}{V_\mathrm{c}}, \qquad \mathbf{c}^* = 2\pi\frac{\mathbf{a}\times\mathbf{b}}{V_\mathrm{c}}, \tag{1.1}$$

where V_c is the volume of the unit cell given by $V_c = \mathbf{a}\cdot(\mathbf{b}\times\mathbf{c})$. Taking this into account, it can further be shown that $\mathbf{r}^*_{hkl}$ is normal to the (hkl) lattice plane and its length is equal to $2\pi/d_{hkl}$, where d_{hkl} is the interplanar distance. In summary, every crystal structure has two lattices associated with it, the real crystal lattice, which can be studied by TEM imaging techniques, and the reciprocal lattice, which can be mapped using diffraction techniques. The two lattices are rigidly connected through the above-mentioned definitions, and it can be further shown that the reciprocal lattice is a Fourier transform of the real crystal lattice. For more information on this topic, see [15, 25].

A simple model of diffraction is represented by the Bragg's law. We will consider a set of lattice planes of spacing d [Fig. 1.10(a)]. An incident electron wave W_I is scattered by the atoms (positions B, C) at an angle of θ, producing a diffracted electron wave W_D. Two adjacent waves (represented by the beams R_1 and R_2) travel different distances with a path difference of $\mathrm{AC} + \mathrm{CD} = 2d\sin\theta$, also causing a phase shift between the waves. Strong diffraction can be observed when the scattered waves are in phase and interfere constructively. This is true when the path difference between the scattered waves is an integer multiple of the wavelength, or

$$2d\sin\theta_\mathrm{B} = n\lambda, \tag{1.2}$$

which is known as the Bragg's law of diffraction. As will be discussed later, in TEM, a strong diffraction spot can be observed, although the electron beam does not impinge the

crystal planes exactly at the Bragg angle θ_B. However, in both cases, the difference in angle between the incident and diffracted beams is close to (or equal to) $2\theta_B$ [Fig. 1.10(b)].

We can now rewrite the Bragg diffraction condition in vector form according to Fig. 1.10(b). The incident electron beam and the diffracted beams are defined by their wave vectors $\mathbf{k}_I$ and $\mathbf{k}_D$, respectively. We assume elastic scattering, thus $|\mathbf{k}_I| = |\mathbf{k}_D| = 2\pi/\lambda$. The incident beam and the diffracted beam are related by the so-called scattering vector $\Delta\mathbf{k} = \mathbf{k}_D - \mathbf{k}_I$. When the Bragg condition is satisfied, we get

$$\Delta\mathbf{k} = \mathbf{g}, \tag{1.3}$$

where $\mathbf{g}$ is a particular reciprocal lattice vector corresponding to the lattice planes that cause the diffraction, thus we can write $\mathbf{g}_{hkl} = \mathbf{r}^*_{hkl} = h\mathbf{a}^* + k\mathbf{b}^* + l\mathbf{c}^*$. As discussed above, the vector $\mathbf{g}_{hkl}$ is normal to the corresponding lattice plane (hkl), and its length is given by $|\mathbf{g}| = 2\pi/d$, where d is the interplanar distance. From the diffraction geometry in Fig. 1.10(b), we can write $|\Delta\mathbf{k}| = 2|\mathbf{k}_I| \sin\theta_B = 2(2\pi/\lambda)\sin\theta_B$. By substituting $|\mathbf{g}|$ and $|\Delta\mathbf{k}|$ into Eq. (1.3), we get $2d\sin\theta_B = \lambda$ corresponding to the Bragg diffraction condition [Eq. (1.2)]. By taking the dot products of $\Delta\mathbf{k}$ and $\mathbf{g}$ with the unit cell vectors $\mathbf{a}$, $\mathbf{b}$, and $\mathbf{c}$, Eq. (1.3) can be further expressed in the form of the well-known Laue equations:

$$\mathbf{a}\cdot\Delta\mathbf{k} = 2\pi h, \qquad \mathbf{b}\cdot\Delta\mathbf{k} = 2\pi k, \qquad \mathbf{c}\cdot\Delta\mathbf{k} = 2\pi l. \tag{1.4}$$

Another useful way to describe the diffraction is by introducing the so-called Ewald sphere construction. Consider a reciprocal crystal lattice in which a wave vector of the incident electron beam $\mathbf{k}_I$ is drawn. One end of the vector is placed at the origin O of the reciprocal lattice. The position of the other end, which can be determined through the direction and length of $\mathbf{k}_I$, is taken as the center of the Ewald sphere of radius $R = |\mathbf{k}_I| = 2\pi/\lambda$ [Fig. 1.10(c)]. If any point in the reciprocal lattice intersects the surface of the Ewald sphere, the Bragg diffraction condition is satisfied, and a diffracted beam can be observed. The radius of the Ewald sphere in Fig. 1.10(c) is rather small, which resembles more an X-ray diffraction, where the reciprocal value of the wavelength (sphere radius) is comparable to the reciprocal lattice parameters, and as a result only a few diffraction spots are observed. In TEM, the situation is different. The reciprocal value of the electron wavelength is much larger than the reciprocal value of the lattice parameters, and thus the Ewald sphere has a radius much larger than in the case of X-ray diffraction. There is also another effect associated with the shape and size of the observed sample, the so-called shape effect. The points of the reciprocal lattice are ideal mathematical points only in the case of an ideal crystal of infinite dimensions. However, in TEM, the sample must be very thin, and, as a result, the reciprocal lattice points are transformed to spots of finite dimensions elongated in the direction of the reduced size of the sample, forming the so-called reciprocal lattice relrods [12][Fig. 1.10(d)]. When the reciprocal relrod is intercepted by the Ewald sphere, diffraction occurs. The intensity of diffraction spots is then proportional to the so-called excitation error, which is a measure of how far we deviate from the exact Bragg condition (center of the relrod). Fig. 1.10(e) shows how a monocrystalline sample diffraction pattern may look in TEM, as the Ewald sphere cuts through the reciprocal lattice planes perpendicular to the direction of the incident beam (the so-called Laue zones). The resulting diffraction pattern is thus a projection of the intersection of the reciprocal lattice relrods and the Ewald sphere, and in TEM, it can be observed in the back focal plane of the objective lens.

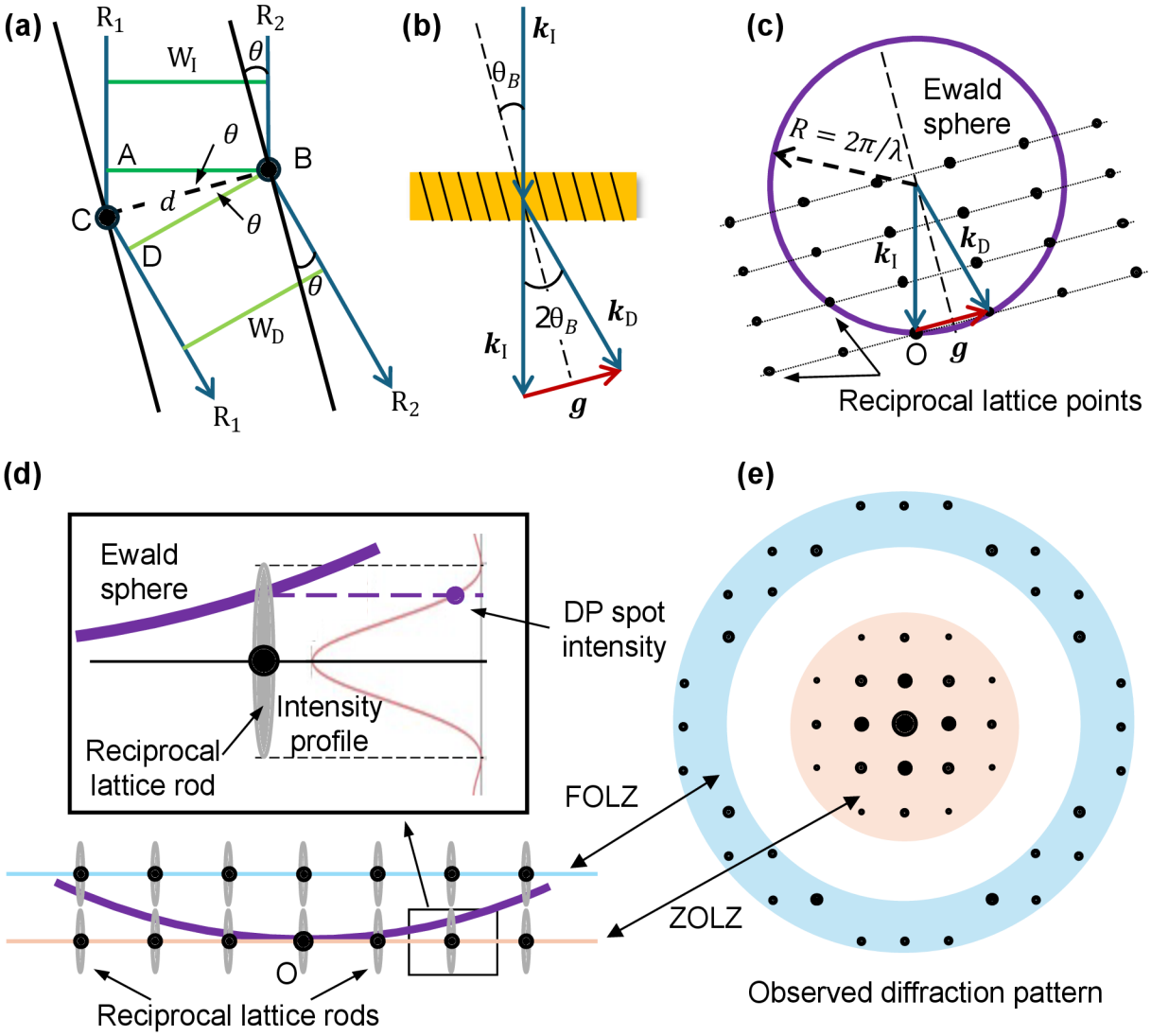

Figure 1.10: A formation of a diffraction pattern in TEM. (a) An incident electron wave is scattered on atoms of two adjacent atomic planes. The rays R_1 and R_2 travel different distances with a path difference AC + CD leading to a phase shift between the rays. At the Bragg angle, the rays interfere constructively, and a strong diffraction is observed. (b) Geometry of Bragg diffraction in TEM. The incident and diffracted electron beams are represented by their wave vectors $\mathbf{k}_\mathrm{I}$ and $\mathbf{k}_\mathrm{D}$, with the angle $2\theta_\mathrm{B}$ between them. (c) Construction of the Ewald sphere. The diffraction condition is satisfied when the Ewald sphere intercepts a reciprocal lattice point. (d) Ewald sphere in TEM intercepting the reciprocal lattice rods, the elongation of the reciprocal lattice rods results from the low thickness of TEM samples, resulting in more diffraction spots appearing in TEM diffraction patterns. The intensity of the diffraction spot is the highest when the Bragg condition is exactly satisfied (the center of the reciprocal relrod) and reduces as the Ewald sphere intercepts the relrod further away from the center (shown in the inset). (e) The resulting diffraction pattern observed in TEM as a projection of the intersection of the Ewald sphere with the reciprocal lattice relrods. The Ewald sphere can intercept more parallel reciprocal planes (Laue zones), a zero-order Laue zone (ZOLZ), and a first-order Laue zone (FOLZ) are depicted. Schematics and ray diagrams are inspired by Refs. [12, 15, 26].

One significant benefit of TEM diffraction techniques is the ability to analyze the crystal structure in specific small regions of the sample, while also utilizing various imaging techniques that offer excellent spatial resolution. The most popular and straightforward diffraction technique in TEM is selected area electron diffraction (SAED). The specimen is illuminated with a broad parallel beam, and a DP and image are formed by the objective lens. An aperture is placed in the image plane of the objective lens to allow only electrons from a selected region of the sample to pass through, only these electrons then contribute to the recorded diffraction pattern, while the rest is blocked by the aperture [see Fig. 1.11(a)]. This technique can be used to study both crystalline and noncrystalline samples. In the case of monocrystalline samples, SAED can be used to determine the crystal orientation, symmetry, or interplanar spacing. Polycrystalline samples typically form ring diffraction patterns to which many randomly oriented grains may contribute. Again, interplanar spacing can be obtained from the radii of these diffraction rings and indexing of the diffraction patterns can be performed.

The interplanar spacing d_{hkl} of a set of (hkl) lattice planes can be established by measuring the distance R_{hkl} between the direct and diffracted spots in the diffraction pattern. Following the geometry in Fig. 1.11(b), we can write $\tan 2\theta_B = R_{hkl}/L$, where L is the camera length. Camera length can be understood in TEM as an effective distance between the specimen and the camera, which changes with the magnification of the imaging lenses. The interplanar spacing can be expressed from Bragg's law [Eq. (1.2)] as $d_{hkl} = \lambda/2\sin\theta_B$. Since the Bragg angles can be considered very small ($\theta_B < 1°$), we can make the approximations $2\sin\theta_B \approx \tan 2\theta_B \approx 2\theta_B$, and so we can write $d_{hkl} = \lambda L/R_{hkl}$. If the camera length is well calibrated, we can obtain the interplanar spacing with reasonable accuracy. Conversely, camera length calibration is performed by measuring the R_{hkl} of a specimen with known d_{hkl} (such as thin gold foil) for different magnifications.

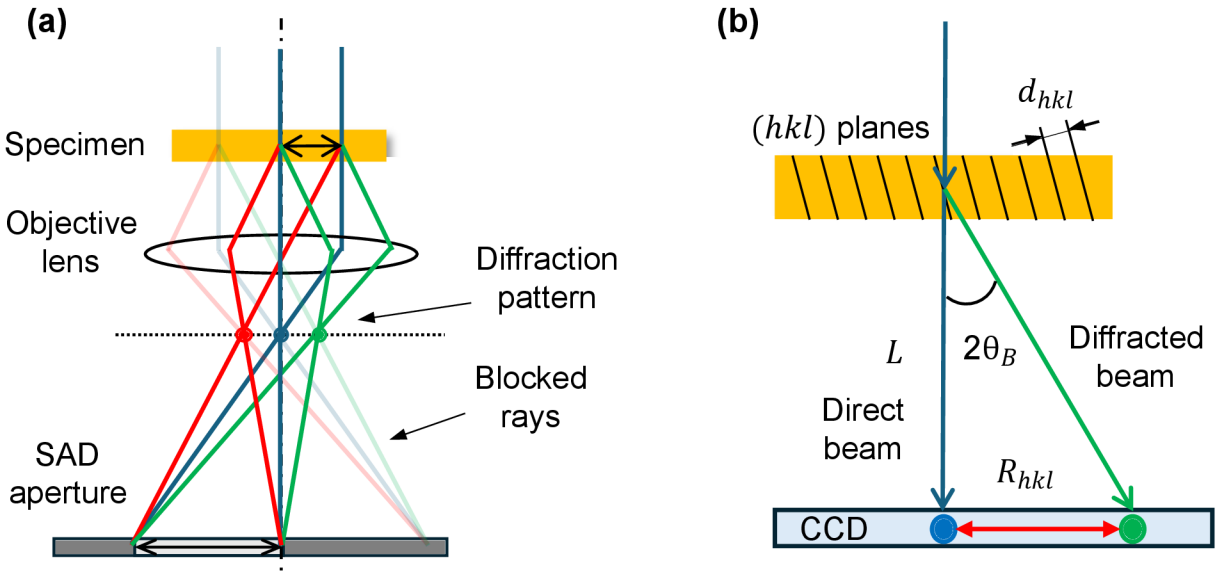

Figure 1.11: (a) Selected area electron diffraction (SAED). Selector (SAD) aperture is inserted in the image plane of the objective lens, ensuring that the observed diffraction pattern comes only from the area of the specimen marked with the arrow, and the rest of the electrons are blocked by the SAD aperture. (b) Geometry for measurements of the diffraction pattern and determination of the interplanar spacing d_{hkl}. Schematics are inspired by [12].

Once the lengths of at least two reciprocal lattice vectors and the angle between them are established, the diffraction pattern can be indexed.

For smaller areas of interest, such as single nanoparticles, a nanoprobe or convergent beam electron diffraction (CBED) might be used, where the studied area is defined directly by the probe size. CBED patterns can also serve to determine specimen thickness, point group, and space group of the crystal lattice, lattice parameters with higher accuracy, and many other parameters [27].

1.3.2 Imaging

When the incident electron beam interacts with the specimen, electron scattering occurs. During scattering events, the amplitude and phase of the electron wave function is modified. The electrons are then transferred through the imaging system and, in the case of TEM mode, form the image of the sample which can be detected by the CCD camera, or, in the case of STEM mode, electrons are detected by the STEM detectors. In order to distinguish individual adjacent areas (or features) of the sample (such as grains or even atomic columns), it is necessary to obtain sufficient image contrast. Image contrast can be defined as

$$C = \frac{I_2 - I_1}{I_1} = \frac{\Delta I}{I_1}, \tag{1.5}$$

where I_1, and I_2 are the intensities of two adjacent areas. In TEM, there are two main types of image contrast: amplitude contrast, which is based on electron scattering events described by particle optics, and phase contrast, which arises from the interference of transmitted and diffracted electron waves in the image plane.

Amplitude Contrast

The amplitude contrast appears as a result of electron scattering on the sample, which then causes a decrease in the intensity of the direct beam of transmitted electrons. By inserting a small aperture into the BFP of the objective lens, it is then possible to absorb these scattered electrons and thus ensure that the image is formed only by directly transmitted (unscattered) electrons. This imaging technique is called bright field (BF) imaging [Fig. 1.12(a)]. In the resulting image, the regions of low scattering (vacuum, thin areas) appear bright, and the regions of high scattering appear dark. We can further distinguish between two types of amplitude contrast, the so-called mass-thickness contrast, and the diffraction contrast.

The mass-thickness contrast can be caused by variation in the sample thickness or the presence of different chemical elements in the sample (high atomic number Z). As more electrons are scattered in the thicker regions of the sample or on heavier atoms, these regions appear darker in the image [Fig. 1.12(a)]. Only on the basis of the observed contrast it cannot be decided whether the decrease in intensity is caused by a higher thickness or a heavier element and, for the interpretation of the image, it is necessary to perform a chemical analysis using analytical techniques (EDS, EELS). The mass-thickness contrast can also be affected by the choice of the objective aperture. Smaller apertures produce images with higher contrast but, in general, lower intensity [Fig. 1.12(a)]. Larger

apertures allow more electrons to pass through, so a higher intensity is observed, but, the image contrast is reduced [Fig. 1.12(b)]. An optimum selection of the aperture size for desired quality of the image depends on the observed sample.

The diffraction contrast occurs in the case of crystalline samples. When a single-crystal grain is oriented in such a way that the Bragg condition is satisfied, many electrons are diffracted and then blocked by the objective aperture. Therefore, the intensity of the direct beam is reduced and the grain appears dark in the BF image [Fig. 1.12(c)]. In addition to classical BF imaging [Fig. 1.13(a)], it is useful to observe crystalline samples using the dark-field (DF) imaging technique. Here, the objective aperture is used to exclude the direct electron beam. It can be achieved by displacing the aperture from the optical axis and centering it around a specific diffracted beam. Consequently, only electrons that are diffracted by grains oriented close to the Bragg condition contribute to the image, and therefore these grains appear bright in the DF image (the vacuum is dark as no scattering occurs). However, when the aperture is displaced from the optical axis, the quality of the image might be affected by off-axis optical aberrations. To avoid this, centered dark-field (CDF) imaging can be used [Fig. 1.13(b)]. The diffraction pattern can be shifted in the BFP of the objective lens by tilting the incident electron beam. In doing so, the diffracted beam of choice can be moved to the optical axis, where it passes

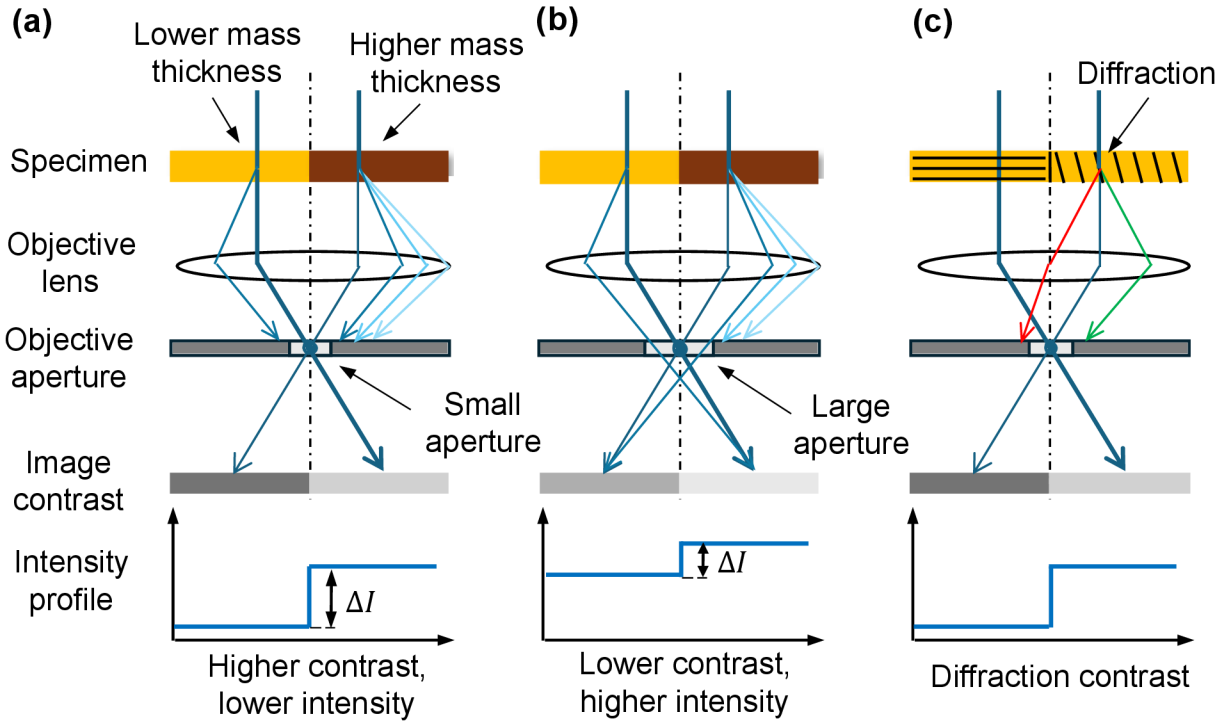

Figure 1.12: Amplitude contrast in TEM bright field images. (a) Areas with higher mass or thickness give rise to more scattering, weakening the transmitted electron beam. Scattered electrons are blocked by the small objective aperture in the BFP of the objective lens. Areas with lower mass scatter less electrons and thus more intensity is transmitted through the aperture. (b) Images with larger objective apertures are of higher intensity, but the contrast is lowered. (c) Two adjacent grains with different orientations can also give rise to amplitude contrast, when the diffraction condition is satisfied. Schematics inspired by [12].

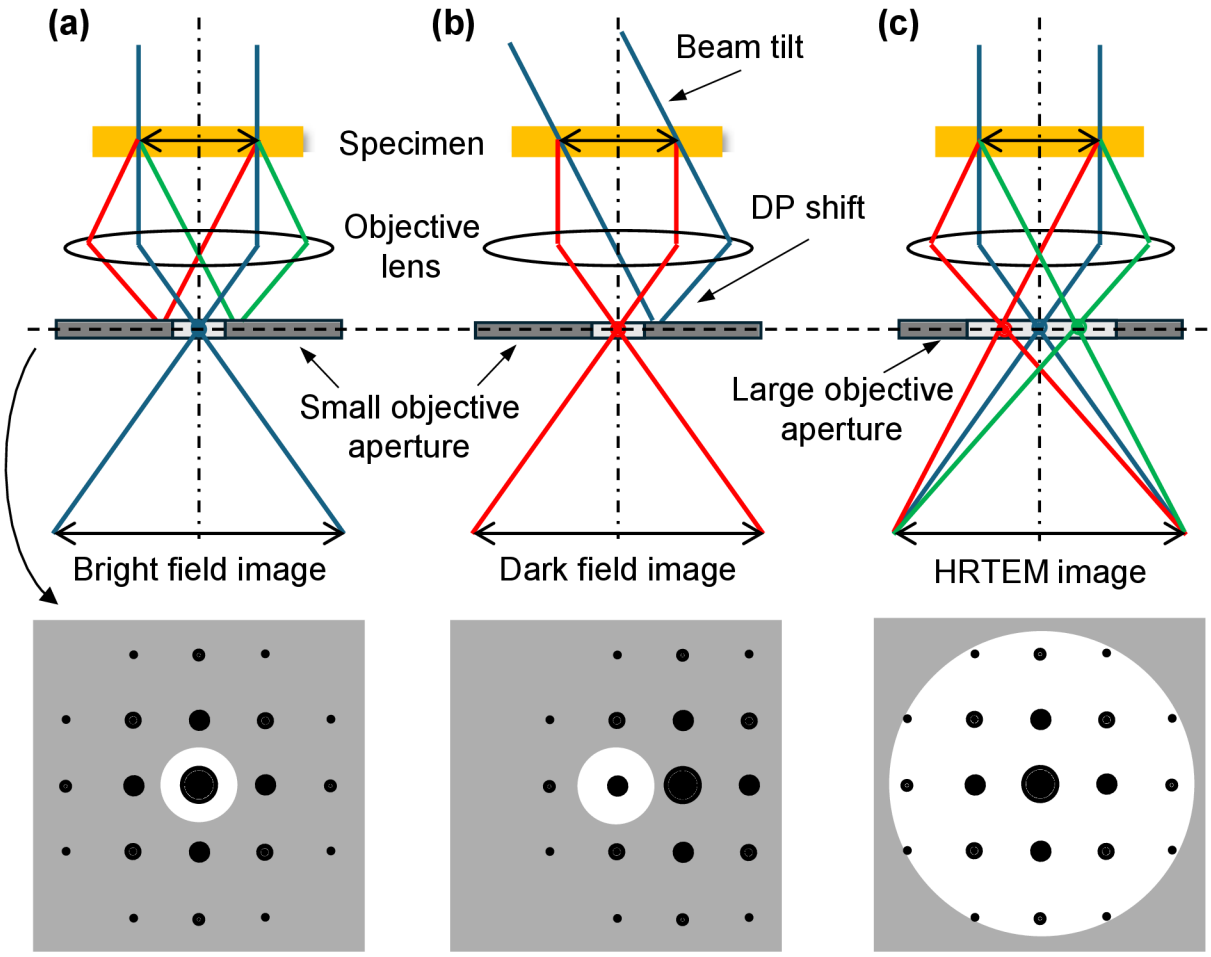

Figure 1.13: TEM Imaging techniques. (a) TEM bright-field (BF) imaging with a small objective aperture centered around the direct beam. (b) TEM centered dark-field (CDF) imaging. By tilting the incident electron beam the diffraction pattern can be shifted, thus a diffraction spot of choice can be brought to the optical axis and used for imaging with a small objective aperture centered around it. (c) High resolution TEM (HRTEM) imaging is performed with a large objective aperture centered around the direct beam letting through many diffracted electron beams which later interfere creating a HRTEM image with dominant phase contrast. Schematics inspired by [12].

through a centered objective aperture, and the quality of the resulting image is improved. Diffraction contrast is also produced by crystal imperfections, such as dislocations, grain boundaries, stacking faults, etc., which can thus be studied using CDF imaging, weak-beam dark-field microscopy and other TEM imaging techniques [12].

Phase Contrast

Phase contrast is caused by the interference of transmitted and diffracted electron waves in the image plane. Unlike the previously described BF and DF imaging techniques, a large objective aperture is centered on the optical axis, allowing many diffracted electron beams to pass through [Fig. 1.13(c)]. The size of this aperture then defines which diffracted beams and hence which spatial frequencies will contribute to the interference pattern of the resulting image. If the available resolution of the microscope is sufficient and if the

sample is oriented along the so-called zone axis[2], it is possible to observe high-resolution TEM images that contain the so-called lattice fringes. These lattice fringes are not a direct image of the crystal structure but reflect the orientation and spacing of the lattice planes. The observed contrast also depends on the sample thickness, defocus, or properties of the optical system and its aberrations described by the contrast transfer function (CTF). This might cause confusion in image interpretation, and therefore HRTEM image simulations are often required to help interpret the experimental data [28].

In addition to HRTEM applications, phase contrast is also used for imaging of magnetic domains (Lorentz microscopy), dislocations using Moiré fringes, or holography, where both the intensity and phase of the electron wave are recorded [12].

Contrast in STEM

The image in STEM is created point by point by scanning a small probe over the sample. Electrons are scattered on the sample at different angles and captured by the STEM detectors [see Fig. 1.8 right].

The circular BF detector is placed around the optical axis, capturing non-scattered electrons or electrons scattered to small angles (up to 10 mrad). The annular dark-field (ADF) detector captures scattered electrons at intermediate angles (10 mrad to 50 mrad). The contrast here is created similarly to that in the case of TEM mode, mass-thickness, or diffraction contrast. Compared to TEM, the mass-thickness images have a better contrast in STEM in general, but a worse resolution and signal-to-noise ratio. The diffraction contrast is almost always better in the TEM mode, where an objective aperture is used to select only a small portion of the scattered electrons typically from a single diffraction spot, whereas in STEM we integrate the signal over the entire annular detector losing contrast, and also useful information about the momentum distribution of the scattered electrons. The high-angle annular detector (HAADF) collects electrons scattered at large angles (more than 50 mrad), which is usually ensured by placing it higher in the electron column. At these high scattering angles, the scattering of electron waves is mostly incoherent, which means that interference effects do not occur, and the recorded image can be understood as a result of Rutherford scattering, which depends on the atomic number Z, and thus the material Z contrast can be observed. This material contrast can be observed even on the atomic scale [29]. Another advantage of using the HAADF detector is that the image can be acquired simultaneously with the spectroscopic data (more details in Section 1.3.4).

The STEM mode generally offers better image contrast than the TEM mode. The use of digital STEM detectors also enables improving image contrast by changing the detector settings, such as offset (black level) and gain. Even more contrast variability can be achieved by changing the camera length parameter, which directly affects the collection angles of the detectors. However, STEM images tend to be more noisy and take longer to acquire, which can be a problem when the sample is not very stable, resulting in sample drift, blurring of the image, and loss of spatial resolution.

[2]Typically an orientation of high crystal symmetry, where the atomic columns are oriented along the direction of the incident electron beam.

1.3.3 Energy Dispersive X-Ray Spectroscopy

Energy dispersive X-ray spectroscopy (EDS) enables qualitative and quantitative analysis of the elemental composition of the specimen. It uses X-rays produced by the interaction of an incident electron beam with the sample. Two types of X-ray can be produced, the so-called bremsstrahlung and characteristic X-rays.

The incident electrons can interact with the atomic nuclei through Coulomb forces and, as a result, they are decelerated. The kinetic energy lost during this process is then radiated in the form of bremsstrahlung X-rays with a continuous photon energy distribution bounded by the energy of the incident electron beam. Bremstrahlung thus creates an unwanted background in the EDS spectra, which must be subtracted when a quantitative analysis of the chemical composition is performed.

For spectroscopic purposes, it is the second type of X-rays that is crucial. Characteristic X-rays can be produced when an incident electron beam ionizes an atom by ejecting one of its inner-shell electrons, leaving a vacant state behind. As the atom returns to the ground state, this vacancy is filled with an electron from a higher energy level. The excess energy, corresponding to the energy difference between the two energy levels, can then be emitted as characteristic X-rays. Because each chemical element has a unique configuration of electronic states, the energies of characteristic X-rays are element-specific and can be used for qualitative analyses of the chemical composition. Characteristic X-rays can be distinguished in the acquired EDS spectrum as distinct peaks. The intensities of these peaks can then be used for the quantification of the chemical composition (as discussed below). Due to the high energy of incident electrons (typically 200 keV to 300 keV), it is possible to acquire spectra with an energy range of up to 80 keV, allowing the detection of all common chemical elements heavier than beryllium [12].

EDS is an ideal technique for qualitative chemical analysis, as it is quick and relatively easy to perform, but difficulties may arise when quantifying the chemical composition of the specimen. First, the spectral resolution of EDS is quite poor, typically around 140 eV, resulting in the overlap of some characteristic peaks. For this reason, it is essential to know which chemical elements should be present in the specimen and which elements might have been introduced unintentionally during the specimen preparation (i.e. ion implantation during ion lithography, possible contaminants from the growth chambers, etc.) to correctly identify the characteristic peaks in the spectra. EDS spectra often contain spurious signals and additional peaks that do not come from the observed area. These signals may come from the copper TEM support grid on which the specimen is placed, the specimen holder, or even from some parts of the microscope (such as objective pole pieces) or the detector itself. This can happen because all of these parts can be hit by scattered electrons or X-rays, generating characteristic X-rays, which may then be misinterpreted as generated in the studied area of the specimen. Artifact peaks such as internal fluorescence peaks, escape peaks, or sum peaks may also arise. The internal fluorescence peak comes from the silicon detector itself, as the incoming X-rays can excite the Si atoms, generating Si K_α X-rays (1.74 keV) which are then detected. Consequently, the X-rays responsible for producing the Si K_α X-rays have their energy reduced by 1.74 keV, and thus appear in the spectra 1.74 keV below the true position of the characteristic peak, these are known as escape peaks. Finally, the sum peaks appear when two X-ray photons enter the detector at the same time and are registered as one X-ray photon with an energy corresponding to the sum of the two X-ray photons. Therefore, before quantification of the spectra, all

characteristic peaks and possible artifacts must be identified to avoid misinterpretation of the spectra.

Quantitative EDS analysis can be performed using the Cliff-Lorimer ratio technique for the case of thin-foil specimens, where any absorption and fluorescence of X-rays in the specimen can be neglected. For a system consisting of two elements A and B the ratio of weight percents C_A and C_B of each element can be related to the ratio of the characteristic peak intensities I_A and I_B through the Cliff-Lorimer equation [12]

$$\frac{C_A}{C_B} = k_{AB}\frac{I_A}{I_B}, \tag{1.6}$$

where k_{AB} is the so-called Cliff-Lorimer factor or shortly k-factor, which depends on the atomic number Z and experimental conditions such as beam energy or detector collection angle. The k-factors can be determined experimentally from thin-foil standards, or they can be calculated using theoretical models. For the binary system, we can further assume that

$$C_A + C_B = 1, \tag{1.7}$$

and thus using Eqs. (1.6) and (1.7) we get the absolute values of weight percents of each element. Systems with more elements can be quantified similarly by extending this set of equations. For more information about this model and its limitations, see Chapter 35 in [12].

EDS can be performed in both the TEM and STEM modes. However, in TEM the X-rays come from the whole illuminated area, and it is not possible to produce very useful qualitative maps of the chemical composition. This is why it is more useful to work in the STEM mode, where a selected area of the sample is scanned sequentially, and an EDS spectrum is taken at each scanning point. This results in a three-dimensional dataset, called a spectrum image, which can be processed to yield EDS spectra and the chemical composition maps.

1.3.4 Electron Energy Loss Spectroscopy

Electron energy loss spectroscopy (EELS) is an analytical technique that studies inelastically scattered electrons, which lost some part of their incident kinetic energy during electron-specimen interactions. These energy-loss electrons are dispersed according to the energy transferred to the specimen (referred to as the loss energy) in the spectrometer and detected, creating an energy loss spectrum. The experimental setup and the creation of energy loss spectra were briefly introduced in Section 1.2.5. An example of such an energy loss spectrum corresponding to a thin silver film is shown in Fig. 1.14. The spectrum can be divided into three main parts according to the loss energy, the so-called zero-loss peak (ZLP), the low-loss region ($\Delta E < 50$ eV), and the core-loss region ($\Delta E > 50$ eV).

Zero-loss peak (ZLP)

The most dominant spectral feature in the EEL spectra is the ZLP corresponding to the electrons, which did not suffer any energy losses as they traversed the specimen. However, it is not possible to create a monochromatic electron beam, and thus the ZLP has a finite energy width, which limits the experimental spectral (or energy) resolution. The spectral

resolution of the EELS is defined by the full width at half maximum (FWHM) of the ZLP recorded by the spectrometer. The FWHM of ZLP is partially affected by the energy spread of the electron gun, which is the lowest for the case of a cold FEG with a value 0.3 eV [see Table 1.1]. However, this spectral resolution might still not be sufficient, especially in the low-loss EELS region, where the signals are deeply embedded in the broad ZLP, as well as when resolving fine structure in the core-loss EELS. Therefore, a monochromator is often included in the TEM optical system to further improve spectral resolution [13]. Nowadays, spectral resolutions of 0.2 eV are quite common and current state-of-the-art instruments can achieve spectral resolutions below 5 meV [31].

Low-loss EELS

The low-loss (or valence) region of the EEL spectra contains low-energy excitations, such as intraband and interband electron transitions or collective oscillations (plasmons, phonons, and their localized modes). Therefore, analysis of the low-loss region yields information on the electronic and optical properties of the material.

Phonon and molecular vibration energies are on the order of 20 meV to 1 eV, and thus it was not possible to probe these excitations until recent advances in the development of EELS instrumentation [31, 32]. It opened up the prospects of electron vibrational spectroscopy with high spatial resolution [33], damage-free spectroscopy of biological materials [34] or mapping of surface phonon polaritons [35].

Single-electron interactions with energy losses up to 25 eV, such as interband or intraband electron transitions [12], can also be observed in low-loss EELS. The material band gap energy can be estimated from the onset of the EELS signal after the subtraction of the ZLP tail. Relativistic effects such as the Čerenkov radiation, which appears when the

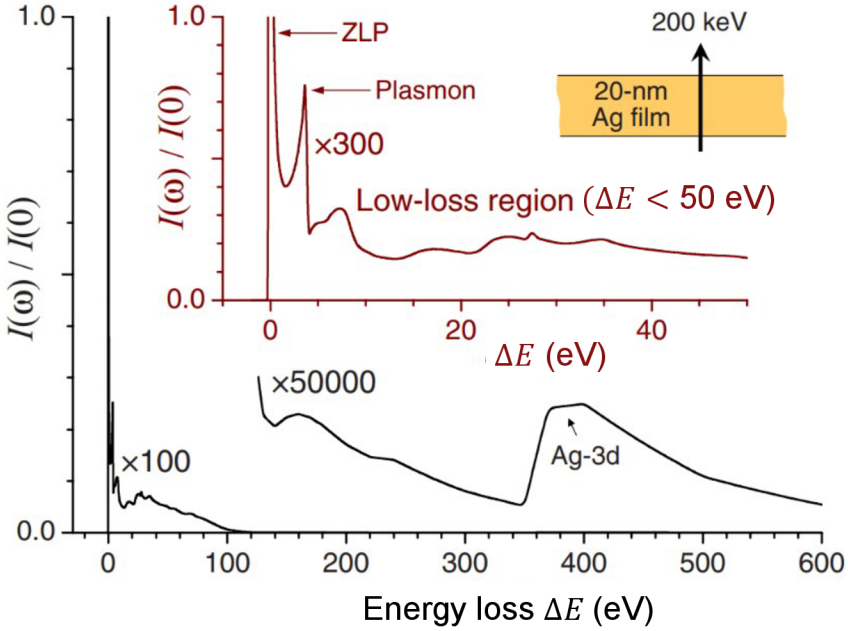

Figure 1.14: A typical electron energy loss spectrum showing a narrow zero-loss peak (ZLP), strong collective modes in the low-loss region (e.g. plasmon peak at 3.7 eV), much weaker core-loss excitations at higher energy losses. The spectrum is calculated for a 200 keV electron beam traversing a 20 nm Ag film. Taken from [30].

velocity of incident electrons exceeds the speed of light in the material, obscure the determination of the band gap energy [36]. When treated correctly, the band-gap mapping with a high spatial resolution can be performed [37], making EELS a prominent technique for characterization of semiconductor optical properties.

The plasmon peak is the second most dominant spectral feature in the EEL spectra after ZLP (Fig. 1.14). It can be attributed to the collective oscillations of a free electron gas in metals, which can be described in the simplest situation by the Drude model of electrical conduction (discussed in Section 2.2.1). Other plasmon peaks may also be present in the spectra, corresponding to surface plasmon polaritons (SPPs), electromagnetic waves propagating along the metal-dielectric interface (Section 2.2.3), or localized surface plasmon resonances (LSPRs) for the case of metallic particles (Section 2.2.4). Furthermore, utilizing the high spatial resolution of the STEM EELS technique, LSPR mapping can be performed. It provides information on the spatial distribution of the EELS signal [38], the so-called loss probability Γ_{EELS}, which can be related to the induced electric field $\mathbf{E}_{\mathrm{ind}}$ of the LSPR through [30]

$$\Gamma_{\mathrm{EELS}}(\omega) = \frac{e}{\pi\hbar\omega} \int \mathrm{Re}\{\mathbf{v} \cdot \mathbf{E}_{\mathrm{ind}}(\mathbf{r}(t), t)\}\, \mathrm{d}t, \tag{1.8}$$

where $\mathbf{v}$ is the velocity of the incident electron, e is the elementary charge, and $\hbar\omega$ corresponds to the loss energy of the electron (thus, to the resonance energy of the excited LSPR). Therefore, the induced electric field in the vicinity of metallic nanoparticles can be experimentally studied by STEM EELS with high spatial resolution.

Core-loss EELS

The core-loss EEL spectrum is contributed by high energy excitations (above 50 eV), such as the ionization (or core-loss) edges, which result from the interactions of the incident electrons with inner-shell electrons of the specimen atoms. This part of the spectrum can thus provide information about the chemical composition of the specimen, since the observed signals are material-specific.

During the deexcitation process of the ionized atoms, X-rays of characteristic energies may be emitted (as discussed in the previous section) providing similar qualitative information. Core-loss EELS and EDS are thus complementary techniques that detect different signals of the same phenomenon. However, the core-loss EELS offers much better spectral resolution and also provides information on the chemical bonding or oxidation states of the elements, which can be determined from the fine edge structure, also known as the energy-loss near-edge structure (ELNES) [13]. The core-loss EELS should always be used for the analysis of light elements for better spectral resolution, but the EDS might be preferable for the analysis of heavy elements since the EELS signal becomes very weak and noisy for higher energy losses. The core-loss EELS signal is free from spurious signals, and the overlapping of peaks is much less severe than in the case of EDS. On the other hand, EELS can suffer from multiple scattering events, which cause difficulties for the quantification of the chemical composition. Therefore, the sample should be thin enough to limit multiple scattering events, or a deconvolution process must be performed to remove multiple scattering effects prior to quantification. Elemental quantification is described, for example, in Chapter 39 in [12], and a more detailed description and derivation can be found in [13].

Thickness Measurement

The thickness of the specimen can also be established using EELS (with the error within 10 %) [13]. If we consider multiple inelastic events as a series of independent collisions, the probability P_n that an incident electron undergoes n scattering events follows the Poisson statistics, thus we can write

$$P_n = \left(\frac{t}{\lambda}\right)^n \frac{\exp\left(-t/\lambda\right)}{n!}, \tag{1.9}$$

where t is the specimen thickness and λ is the so-called mean-free path for inelastic scattering, resembling the average distance between collisions. The ratio t/λ thus gives the mean number of inelastic collisions.

Consider now that no inelastic scattering event occurred, thus $n = 0$, then Eq. (1.9) simplifies into

$$P_0 = \exp\left(-t/\lambda\right) = \frac{I_0}{I_\mathrm{t}}, \tag{1.10}$$

where we expressed the probability P_0 as a ratio of measurable intensities of EELS signals, corresponding to the energy-integrated intensity of the ZLP I_0 (containing all non-scattered electrons) and the total integrated intensity of the acquired spectrum I_t.

Using this relation in Eq. (1.10), we can express the specimen thickness as follows

$$t = \lambda \ln\left(I_\mathrm{t}/I_0\right) \tag{1.11}$$

As discussed above, the intensities I_0 and I_t can easily be determined from the low-loss EELS measurement. For the case of a thin, light element specimen it is sufficiently accurate to estimate I_t only from the low-loss EELS signal (below 50 eV), as the core-loss intensity is too small and can be neglected. However, as the mass-thickness of the specimen grows, multiple scattering events occur, and I_t should be integrated over a larger interval of loss energies to maintain sufficient accuracy of the thickness estimation. The mean free path of inelastic scattering λ can be found in the literature for common materials, calculated, or established experimentally (for more details, see Section 5.1 in [13]).

2 Nanophotonics

2.1 Electromagnetic Field in Materials

The electromagnetic field in materials can be expressed in terms of four macroscopic fields, the electric field **E**, the electric displacement **D**, the magnetic field **H**, and the magnetic induction **B**. Their relations and dynamics are described by Maxwell's equations, which form the basis of the theory of electrodynamics [39, 40]. Maxwell's equations can be written in the form

$$\nabla \cdot \mathbf{D}(\mathbf{r}, t) = \rho_{\text{free}}(\mathbf{r}, t), \tag{2.1a}$$

$$\nabla \cdot \mathbf{B}(\mathbf{r}, t) = 0, \tag{2.1b}$$

$$\nabla \times \mathbf{E}(\mathbf{r}, t) = -\frac{\partial}{\partial t}\mathbf{B}(\mathbf{r}, t), \tag{2.1c}$$

$$\nabla \times \mathbf{H}(\mathbf{r}, t) = \mathbf{J}_{\text{free}}(\mathbf{r}, \mathbf{t}) + \frac{\partial}{\partial t}\mathbf{D}(\mathbf{r}, t), \tag{2.1d}$$

where ρ_{free} and $\mathbf{J}_{\text{free}}$ are the free charge and current densities, respectively.

We can now introduce polarization **P** as an electric dipole moment per unit of volume and magnetization **M** as a magnetic dipole moment per unit of volume accordingly. These quantities reflect the response of the material that is subjected to external electromagnetic fields. Using these quantities, we can further link the four macroscopic fields through

$$\mathbf{D}(\mathbf{r}, t) = \varepsilon_0 \mathbf{E}(\mathbf{r}, t) + \mathbf{P}(\mathbf{r}, t), \tag{2.2a}$$

$$\mathbf{H}(\mathbf{r}, t) = \frac{1}{\mu_0}\mathbf{B}(\mathbf{r}, t) - \mathbf{M}(\mathbf{r}, t), \tag{2.2b}$$

where ε_0 and μ_0 are the electric permittivity and magnetic permeability of the free space. Throughout this thesis, we assume nonmagnetic materials, and thus Eq. (2.2b) simplifies to $\mathbf{H}(\mathbf{r}, t) = \mathbf{B}(\mathbf{r}, t)/\mu_0$. Furthermore, if we consider a linear and homogeneous material, the polarization **P** of the material can be related to the applied external electric field **E** through the convolution product [2]

$$\mathbf{P}(\mathbf{r}, t) = \varepsilon_0 \int \mathrm{d}t' \int \mathrm{d}^3\mathbf{r}' \chi(\mathbf{r} - \mathbf{r}', t - t')\mathbf{E}(\mathbf{r}', t'), \tag{2.3}$$

where χ is the electric susceptibility of the material. By performing the spatial and temporal Fourier transforms, Eq. (2.3) can be expressed in the frequency domain as

$$\mathbf{P}(\mathbf{k}, \omega) = \varepsilon_0 \chi(\mathbf{k}, \omega)\mathbf{E}(\mathbf{k}, \omega), \tag{2.4}$$

here susceptibility depends on both frequency ω and wave vector (spatial frequency) **k**.

If we also apply the Fourier transforms in Eq. (2.2a) and substitute Eq. (2.4) for $\mathbf{P}(\mathbf{k}, \omega)$, we get

$$\mathbf{D}(\mathbf{k}, \omega) = \varepsilon_0 \varepsilon(\mathbf{k}, \omega)\mathbf{E}(\mathbf{k}, \omega), \tag{2.5}$$

where we introduce the dielectric function as $\varepsilon(\mathbf{k}, \omega) = 1 + \chi(\mathbf{k}, \omega)$, describing the optical response of the material. Here, the dielectric function depends on both the angular and

spatial frequencies, which results from the non-local and non-instantaneous response of the material, such material is then referred to as dispersive. For many materials, it can be assumed that their response is spatially local, i.e. the wavelength of the incoming EM wave is significantly larger than the characteristic lengths of the processes responsible for the polarization of the material (mean free path of electrons, size of the unit cell, etc.). Then in Eq. (2.3) we can consider $\chi(\mathbf{r}-\mathbf{r}', t-t') = \delta(\mathbf{r}-\mathbf{r}')\chi(t-t')$, the integral in this equation is simplified, and after performing the Fourier transforms we get the electric susceptibility, and hence the dielectric function, depending only on the angular frequency ω, which is considered throughout this work. In the following section, the dielectric function for the so-called dipole oscillator (Lorentz) model will be derived and its applicability on the description of the optical response of metals and polar crystals will be shown.

2.2 Optical Properties of Materials

2.2.1 The dipole oscillator (Drude-Lorentz) model

The dipole oscillator model (or Drude-Lorentz model) provides a simple way to derive the dielectric function of the material describing its optical response. It is based on the classical model of a harmonic oscillator, where two oppositely charged particles are bound together, oscillating with a natural resonance frequency ω_0. For instance, it can be an electron oscillating around the positively charged nucleus or the oscillations of two oppositely charged ions. The binding of oppositely charged particles can be described by a restoring force $m\omega_0^2\mathbf{r}(t)$, where m is the mass of the oscillator and $\mathbf{r}(t)$ is the displacement vector. The oscillator is driven by an external time-varying electric field $\mathbf{E}(t)$ and damped via collisions within the material, which can be represented by a force $-m\gamma \mathrm{d}\mathbf{r}(t)/\mathrm{d}t$, where γ is the characteristic collision frequency (also known as the damping constant). Then we can write the equation of motion of the driven oscillator in the form

$$m\frac{\mathrm{d}^2\mathbf{r}(t)}{\mathrm{d}t^2} = -m\omega_0^2\mathbf{r}(t) - m\gamma\frac{\mathrm{d}\mathbf{r}(t)}{\mathrm{d}t} - e\mathbf{E}(t). \tag{2.6}$$

If we now consider a harmonic time dependence of the external electric field $\mathbf{E}(t) = \mathbf{E}_0 \exp(\mathrm{i}\omega t)$, a particular solution of Eq. (2.6) will take the form $\mathbf{r}(t) = \mathbf{r}_0 \exp(\mathrm{i}\omega t)$, where

$$\mathbf{r}_0(\omega) = -\frac{e}{m(\omega_0^2 - \omega^2 - \mathrm{i}\gamma\omega)}\mathbf{E}_0. \tag{2.7}$$

The displacement $\mathbf{r}_0$ leads to a dipole moment $\mathbf{p}_0(\omega) = -e\mathbf{r}_0(\omega)$. Therefore, each oscillator contributes to the total macroscopic polarization of the material $\mathbf{P}(\omega) = n\mathbf{p}_0(\omega) = -ne\mathbf{r}_0(\omega)$, where n is the density of oscillators. By substituting Eq. (2.7) into this expression, we get

$$\mathbf{P}(\omega) = \frac{ne^2}{m(\omega_0^2 - \omega^2 - \mathrm{i}\gamma\omega)}\mathbf{E}_0, \tag{2.8}$$

where the expression on the right-hand side of the equation before $\mathbf{E}_0$ can be according to Eq. (2.4) assigned to the expression $\varepsilon_0\chi(\omega)$ and because $\epsilon(\omega) = 1 + \chi(\omega)$, the dielectric function of the dipole oscillator model can be written as

$$\varepsilon(\omega) = \varepsilon_\infty + \frac{ne^2}{m\varepsilon_0}\frac{1}{\omega_0^2 - \omega^2 - \mathrm{i}\gamma\omega}, \tag{2.9}$$

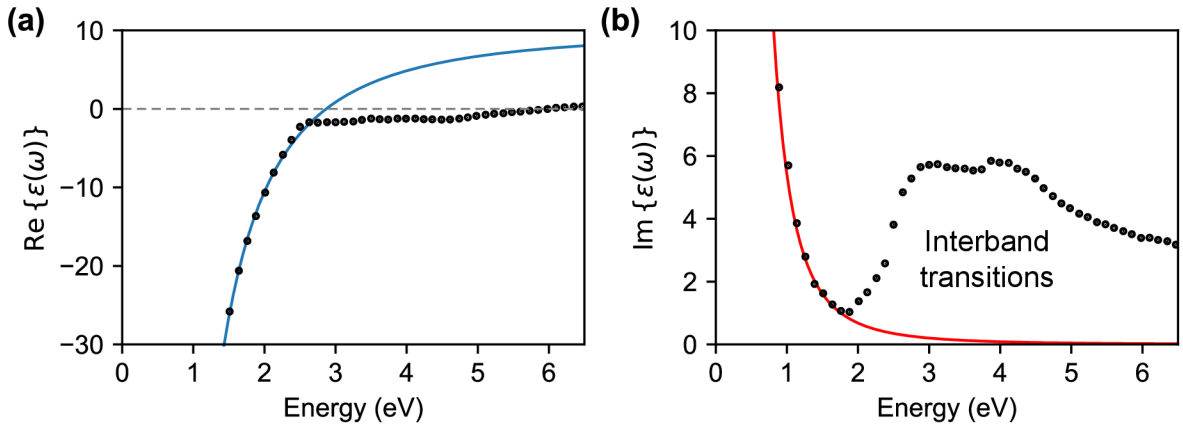

Figure 2.1: (a) Real part and (b) imaginary part of the dielectric function of gold. Solid lines correspond to the theoretical model of a free electron gas (Drude model) with parameters $\hbar\omega_{\mathrm{P}} = 9.03$ eV, $\hbar\gamma = 0.066$ eV, $\varepsilon_\infty = 10.0$ taken from MNPBEM toolbox (Section 2.3.1). Experimental data (black dots) taken from [41].

where we introduced ε_∞ as the so-called high-frequency limit corresponding to the polarization caused by other non-resonant processes [3]. Furthermore, Eq. (2.9) can be generalized to describe several resonances of different frequencies by introducing a summation over the individual resonator contributions to the dielectric function [1].

Despite its simplicity, the dipole oscillator model accurately describes the optical response of some materials in the visible and infrared frequency range. In the following discussion, this model will be utilized with minor changes to describe the optical response of metals and polar crystals.

The Dielectric Function of Metals

The derivation of the dielectric function of metals can be made using a procedure similar to that in the previous section. However, in the case of metals, electrons in the conduction band are considered to act as a free electron gas, moving in a stationary ionic background. This can be taken into account by setting $\omega_0 = 0$ in Eq. (2.6) and in the following equations. When the metal is illuminated by an external wave, the electrons collectively oscillate as a free electron gas and their motion is damped via collisions represented by a collision frequency γ. Considering this, the dielectric function for metals can be written as

$$\varepsilon(\omega) = \varepsilon_\infty - \frac{\omega_{\mathrm{p}}^2}{\omega^2 + \mathrm{i}\gamma\omega}, \tag{2.10}$$

(so-called Drude model) where we introduced the so-called plasma frequency of the material in the form $\omega_{\mathrm{p}} = \sqrt{\frac{ne^2}{\varepsilon_0 m_e}}$, where n is the electron density, e and m_e are the electron charge and mass, respectively. In Section 2.2.2 it will be shown that at this frequency a resonance occurs in the form of longitudinal oscillations of the electron gas, which are known as a plasmon.

Note that the dielectric function is, in general, a complex quantity and can thus be expressed using real and imaginary parts $\varepsilon(\omega) = \varepsilon_1(\omega) + \mathrm{i}\varepsilon_2(\omega)$, where

$$\varepsilon_1(\omega) = \mathrm{Re}\{\varepsilon(\omega)\} = \varepsilon_\infty - \frac{\omega_\mathrm{p}^2}{\omega^2 + \gamma^2} \tag{2.11a}$$

$$\varepsilon_2(\omega) = \mathrm{Im}\{\varepsilon(\omega)\} = \frac{\omega_\mathrm{p}^2 \gamma}{\omega(\omega^2 + \gamma^2)}. \tag{2.11b}$$

These theoretical relations are plotted in Fig. 2.1 with the parameters ω_0 and γ corresponding to gold, which is a commonly used material in plasmonics for the preparation of nanostructures or metasurfaces and which will also be used as a material for the research of the plasmonic lightning-rod effect in this work. The real part of the dielectric function is shown in Fig. 2.1(a) and the imaginary part in Fig. 2.1(b), solid lines correspond to the theoretical model described by the Drude model [Eqs. (2.11a)–(2.11b)] and the black dots refer to the experimental data obtained from [41]. We can see that for energies below 2 eV the Drude model describes the optical response of gold reasonably well. However, above this energy, the Drude model deviates from the experimental dielectric function due to the onset of interband transitions in gold, related to the increase in the imaginary part of the dielectric function [1]. The interband transitions can be modeled approximately as Lorentz oscillators of the form of Eq. (2.9).

In summary, the Drude model of free electron gas can be used to describe the optical properties of metals, but often with limited validity. For a more realistic description it is then necessary to consider theoretical models that account for interband and intraband transitions, or use the dielectric function obtained experimentally.

The Dielectric Function for Polar Crystals

The dipole oscillator model can also be used to describe the optical properties of polar crystals, in which collective lattice vibrations, called optical phonons, can be excited. Polar crystals are typically formed by a two-atom basis consisting of oppositely charged ions. This can be the case of some semiconductors such as GaP, GaAs, etc. The motion of ions in the crystal lattice can again be described by Eq. (2.6), where we initially neglect damping for simplicity, thus $\gamma = 0$. The dielectric function of a polar crystal has the form

$$\varepsilon(\omega) = \varepsilon_\infty + \frac{ne^2}{m\varepsilon_0} \frac{1}{\omega_\mathrm{TO}^2 - \omega^2}, \tag{2.12}$$

where the resonant frequency to ω_TO corresponds to the transverse optical (TO) phonon. By introducing the low-frequency dielectric constant $\varepsilon(0) = \varepsilon_\infty + ne^2/(m\varepsilon_0\omega_\mathrm{TO}^2)$, we can rewrite Eq. (2.12) as

$$\varepsilon(\omega) = \varepsilon_\infty + \frac{\varepsilon(0) - \varepsilon_\infty}{1 - \omega^2/\omega_\mathrm{TO}^2}. \tag{2.13}$$

At frequency ω_LO collective longitudinal vibrations of the crystal lattice occur, called the longitudinal optical phonon (LO). Furthermore, at this frequency the dielectric function Eq. (2.13) is zero, from which the Lyddane-Sachs-Teller (LST) relation can be deduced

$$\frac{\varepsilon(0)}{\varepsilon_\infty} = \frac{\omega_\mathrm{LO}^2}{\omega_\mathrm{TO}^2}. \tag{2.14}$$

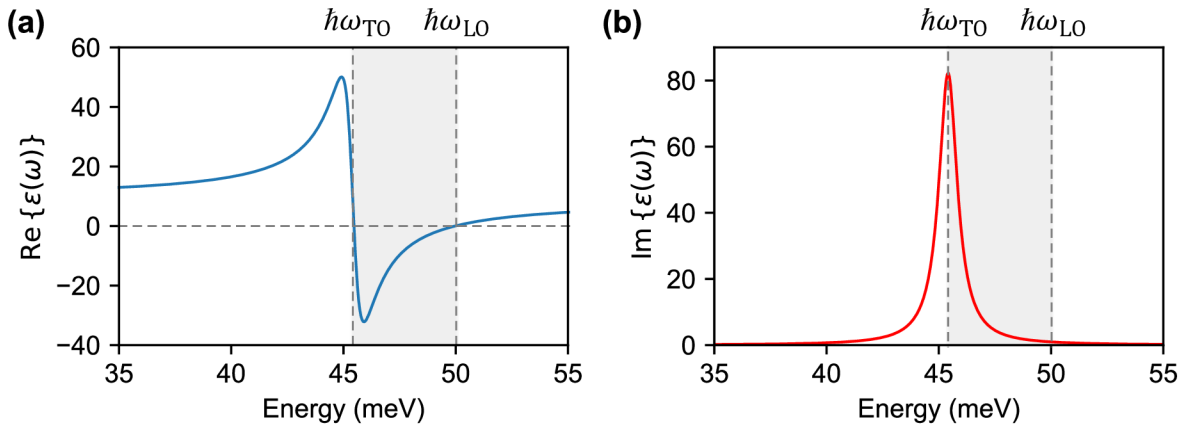

Figure 2.2: (a) Real part and (b) imaginary part of the dielectric function of polar crystals given by Eq. (2.2) obtained using parameters $\varepsilon_\infty = 8.5$, $\varepsilon(0) = 10.7$, $\hbar\omega_{TO} = 45.4$ meV, $\hbar\omega_{LO} = 50.0$ meV. These parameters taken from [25] are typical for gallium phosphide (GaP). The damping is set to $\hbar\gamma = 100$ meV.

Using the LST relation, we can further rewrite Eq. (2.13) into

$$\varepsilon(\omega) = \varepsilon_\infty \left(1 + \frac{\omega_{LO}^2 - \omega_{TO}^2}{\omega_{TO}^2 - \omega^2 - i\gamma\omega}\right), \tag{2.15}$$

where we added damping represented by the damping constant γ, limiting the lifetimes of optical phonons. The lifetime is determined by scattering of phonons e.g. on defects of the crystal lattice, such as impurities, vacancies, interstitial atoms [2].

The real and imaginary parts of the dielectric function Eq. (2.15) are plotted in Fig. 2.2(a) and Fig. 2.2(b), respectively, for the case of gallium phosphide (GaP). Note the sharp peak in the imaginary part around 45 meV that corresponds to the increased absorption of electromagnetic radiation upon excitation of TO phonons in GaP. Furthermore, between the energies $\hbar\omega_{TO}$ and $\hbar\omega_{LO}$ (shaded gray area), the real part of the dielectric function is negative, which means that electromagnetic waves in this energy interval (called Reststrahlen band) cannot propagate through the bulk polar crystal, and total reflection occurs, instead. Similar behavior is observed for the case of metals for energies below $\hbar\omega_P$, where the real part of the dielectric is also negative, see Fig. 2.1(a).

2.2.2 Bulk Polaritons

In this section, we will focus on the propagation of electromagnetic waves in the bulk material for the case of both metals and polar crystals. Consider a medium without free charges, $\rho_{free} = 0$, and free currents $\mathbf{J}_{free} = \mathbf{0}$. From Maxwell's equations (2.1a)–(2.1d) the wave equation for the electric field vector $\mathbf{E}(\mathbf{r}, t)$ can be derived by direct application of mathematical operators and operator identities in the form

$$\nabla(\nabla \cdot \mathbf{E}) - \nabla^2\mathbf{E} = -\varepsilon_0\mu_0\varepsilon(\omega)\frac{\partial^2\mathbf{E}}{\partial t^2}, \tag{2.16}$$

which can be expressed in the frequency domain as [3]

$$\mathbf{k}(\mathbf{k} \cdot \mathbf{E}) - k^2\mathbf{E} = -\varepsilon(\omega)\frac{\omega^2}{c^2}\mathbf{E}, \tag{2.17}$$

where we denote $c = \frac{1}{\sqrt{\varepsilon_0 \mu_0}}$. Let us now focus on two cases of waves satisfying Eq. (2.17), transverse and longitudinal waves. For transverse waves, the electric intensity vector $\mathbf{E}$ is perpendicular to the direction of propagation of electromagnetic waves given by the wave vector $\mathbf{k}$, i.e. $\mathbf{k} \cdot \mathbf{E} = 0$. From Eq. (2.17) we then get the general dispersion relation of the transverse waves:

$$k^2 = \varepsilon(\omega) \frac{\omega^2}{c^2}. \tag{2.18}$$

For the case of longitudinal waves, when the electric intensity vector $\mathbf{E}$ is parallel to the wave propagation direction $\mathbf{k}$, the left side of Eq. (2.17) is zero, which leads to a nontrivial solution for

$$\varepsilon(\omega) = 0. \tag{2.19}$$

As mentioned in Section 2.2.1, collective longitudinal oscillations in the material occur when this condition is met. For the metals described by the Drude model, this condition is satisfied approximately at the plasma frequency ω_p, when longitudinal oscillations of the free electron gas, known as plasmon, occur. In polar crystals, the condition is fulfilled at the frequency ω_LO, when the longitudinal vibrations of the crystal lattice, the longitudinal optical (LO) phonon, are excited. These longitudinal oscillations do not couple to transverse electromagnetic waves and thus cannot be excited by them. However, they can be excited by an electron beam, which enables the study of bulk plasmons and phonons by EELS.

Now let us consider transverse waves satisfying the relation (2.18), to which we insert dielectric functions for metals and polar crystals derived in the previous section to obtain the dispersion relations for waves in these materials. We start with metals by inserting Eq. (2.10) with the parameters $\varepsilon_\infty = 1$ and $\gamma = 0$ (damping neglected) into the dispersion relation Eq. (2.18). We obtain the dispersion relation of bulk plasmon polaritons

$$\omega^2 = \omega_\mathrm{p}^2 + c^2 k^2. \tag{2.20}$$

This relation is plotted for parameters typical for gold in Fig. 2.3(a). Note that for frequencies $\omega < \omega_\mathrm{p}$, transverse waves cannot propagate within the metal. As discussed in the previous section, the dielectric function is negative for these frequencies. Taking into account Eq. (2.18), this leads to imaginary values of the wave vector magnitude, i.e. $k = \mathrm{i}\kappa$, giving rise to evanescent waves whose amplitudes decay exponentially in the material. For frequencies $\omega > \omega_\mathrm{p}$, Eq. (2.20) yields a solution of transverse electromagnetic waves propagating through the metal [blue curve in Fig. 2.3(a)]. We can see that the solution converges to the plasmon energy $\hbar\omega_\mathrm{P}$ in the long-wavelength limit, that is, when $k \to 0$, and for high energies it asymptotically approaches the light line given by $\omega = ck$.

Similarly, we can proceed with polar crystals by inserting the dielectric function Eq. (2.15) into the dispersion relation Eq. (2.18). The solution is plotted in Fig. 2.3(b) for GaP (blue lines) along with the experimentally obtained values (black dots) taken from [25]. We can see that in this case we obtained two solutions (branches) of bulk phonon polaritons, which are separated by a band of forbidden energies (Restrahlen band, shaded area) limited by the energies of the transverse and longitudinal optical phonons. In this interval, no electromagnetic waves can propagate through the polar crystals. Taking into account the asymptotic behavior of the two solutions, the lower branch approaches $\hbar\omega_\mathrm{TO}$

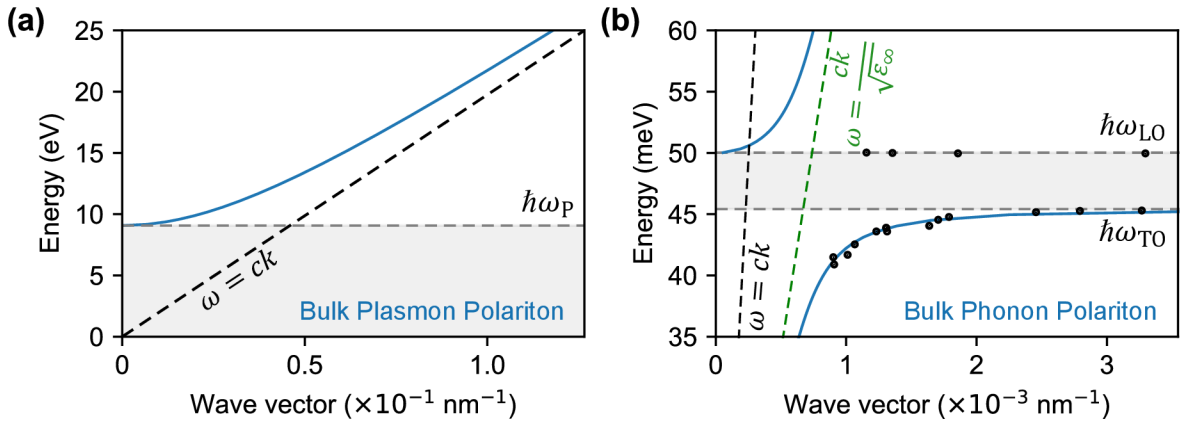

Figure 2.3: (a) Dispersion relation of a bulk plasmon polariton in gold given by Eq. (2.20) for parameters $\hbar\omega_P = 9.03$ eV, $\hbar\gamma = 0$, $\varepsilon_\infty = 1$. (b) Dispersion relation of bulk phonon polaritons in GaP for parameters used in Fig. 2.9. Theoretical dispersion curves are shown by solid lines with. The black dots refer to experimental values of the observed energies and wave vectors of the polaritons and LO phonons by C. H. Henry and J. J. Hopfield, data taken from [25].

for the large magnitudes of the wave vector, and the upper branch approaches the light line in the medium given by $\omega = ck/\sqrt{\varepsilon_\infty}$.

In this part, the simplest waves propagating inside a material have been discussed, the bulk plasmon polaritons in metals and the bulk phonon polaritons in polar crystals. In the next part, we restrict ourselves to the discussion of metals and show that the metal-dielectric interface supports a propagating electromagnetic wave bound to the interface and connected with the oscillations of the free electron gas, the so-called surface plasmon polariton (SPP).

2.2.3 Surface Plasmon Polariton

Surface plasmon polaritons (SPPs) are electromagnetic evanescent waves propagating along the metal-dielectric interface connected to oscillations of surface charges. In this section, we examine the properties of SPP together with the conditions of their existence and the possibilities of their excitation.

Consider the geometry in Fig. 2.4, where the dielectric (medium 1) and metal (medium 2) half-spaces are separated by an interface at $z = 0$. Next, consider a planar electromagnetic wave described by its wave vector $\mathbf{k_1} = (k_{1,x}, 0, -k_{1,z})$ impinging on the metal-dielectric interface. Initially, let us assume the electromagnetic wave vector in the metal in general form $\mathbf{k}_2 = (k_{2,x}, k_{2,y}, k_{2,z})$. We neglect the absorption of the electromagnetic wave in both materials, as a result of which their dielectric functions are real. The dielectric material is described by a positive dielectric constant $\varepsilon_1 > 0$ and for the metal we assume $\varepsilon_2(\omega) < 0$, which is met for frequencies below ω_P (Section 2.2.1). When the electromagnetic wave hits the interface, it must satisfy the boundary conditions [39, 40]. The continuity of the tangential components of $\mathbf{E}$ and $\mathbf{H}$ implies that $k_{1,x} = k_{2,x} \equiv k_x$ and $k_{1,y} = k_{2,y} = 0$. Taking into account the dispersion relation given by Eq. (2.18) for the electromagnetic wave in the metal, we can write $k_x^2 + k_{2,z}^2 = \varepsilon_2(\omega)\omega^2/c^2$. The right-hand side of this equation is negative because $\varepsilon_2 < 0$, hence $k_{2,z}^2 < 0$, which is satisfied only for

the imaginary $k_{2,z}$, i.e. $k_{2,z} = \mathrm{i}\kappa_{2,z}$. The electromagnetic wave can therefore only propagate along the metal-dielectric interface, having an evanescent character in both media in the direction normal to the interface [3].

According to the polarization of these propagating waves bound to the interface, one can distinguish between two types of guided modes: the transverse magnetic (TM) mode and the transverse electric (TE) mode. However, for the geometry of an infinite metal-dielectric interface discussed, it can be shown from the boundary conditions that only the transverse magnetic (TM) mode exists [3], where the magnetic field vector **H** has only

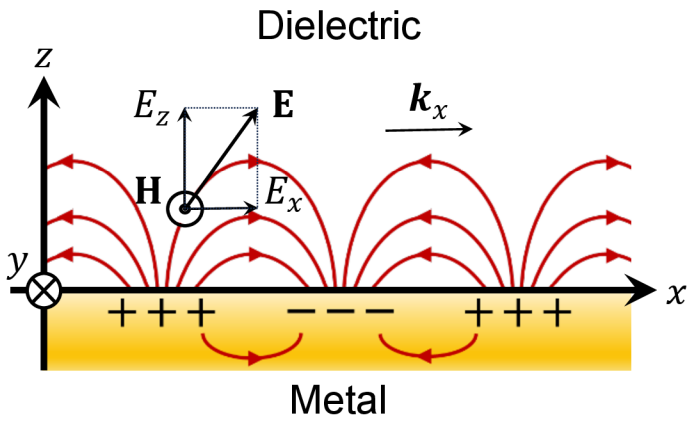

Figure 2.4: Schematic of the surface plasmon polariton (SPP) confined at the metal-dielectric interface propagating along the x axis. The SPP is accompanied with coherent charge oscillations at the interface. The electromagnetic fields have transverse magnetic (TM) polarization and decay exponentially along the z axis in both media.

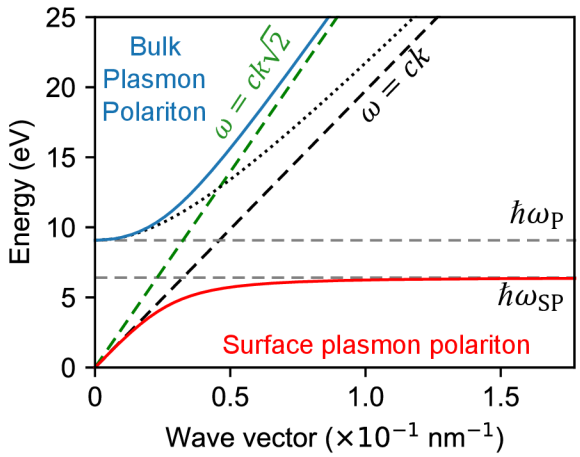

Figure 2.5: Dispersion relation of surface plasmon polariton (red line) and bulk plasmon polariton (blue line) determined by Eq. (2.26) for a Drude dielectric function given by Eq. (2.10) for parameters $\hbar\omega_P = 9.03$ eV, $\hbar\gamma = 0$, $\varepsilon_\infty = 1$, corresponding to gold. The SPP dispersion relation asymptotically approaches the energy of the surface plasmon given by $\hbar\omega_{SP} = \hbar\omega_P/\sqrt{1+\varepsilon_\infty} = \hbar\omega_P/\sqrt{2}$. The dotted line corresponds to the bulk polariton from Fig. 2.3(a).

one non-zero component H_y parallel to the interface (Fig. 2.4). Thus we can write the magnetic field in both media in the form

$$\mathbf{H}_1 = (0, H_{1,y}, 0) = (0, A_1, 0) \exp(\mathrm{i}k_x x - \kappa_{1,z} z), \tag{2.21a}$$
$$\mathbf{H}_2 = (0, H_{2,y}, 0) = (0, A_2, 0) \exp(\mathrm{i}k_x x + \kappa_{2,z} z), \tag{2.21b}$$

where A_1 and A_2 denote the amplitudes of the magnetic field in the dielectric and the metal, respectively. The signs before the z-component of the wave vector ensure the evanescent character of the wave in both media. The electric intensity $\mathbf{E}$ can be obtained by inserting Eq. (2.21a) and Eq. (2.21b) into the Ampere–Maxwell law (2.1d):

$$\mathbf{E}_1 = H_{1,y} \frac{1}{\varepsilon_0 \varepsilon_1 \omega} (\mathrm{i}\kappa_{1,z}, 0, -k_x), \tag{2.22a}$$
$$\mathbf{E}_2 = H_{2,y} \frac{1}{\varepsilon_0 \varepsilon_2 \omega} (-\mathrm{i}\kappa_{2,z}, 0, -k_x). \tag{2.22b}$$

From the continuity of the tangential components of $\mathbf{H}$ and $\mathbf{E}$ at the interface, we get the conditions $A_1 = A_2$ and

$$\frac{\kappa_{1,z}}{\kappa_{2,z}} = -\frac{\varepsilon_1}{\varepsilon_2}. \tag{2.23}$$

The components of the wave vectors on the left side of the equation must be positive for the fields to be evanescent in both media, and therefore the dielectric functions on the right side must have opposite signs. This is the first condition for the formation of a SPP:

$$\varepsilon_1(\omega)\varepsilon_2(\omega) < 0. \tag{2.24}$$

This condition is easily satisfied at the metal-dielectric interface. By taking a square of Eq. (2.23) and substituting for $\kappa_{1,z}$ and $\kappa_{2,z}$ from the dispersion relation, we obtain

$$\frac{\varepsilon_1^2}{\varepsilon_2^2} = \frac{k_x^2 - \varepsilon_1 \omega^2/c^2}{k_x^2 - \varepsilon_2 \omega^2/c^2}. \tag{2.25}$$

By solving the Eq. (2.25) for k_x we finally arrive to the dispersion relation of the surface plasmon polariton

$$k_x = k_0 \sqrt{\frac{\varepsilon_1 \varepsilon_2}{\varepsilon_1 + \varepsilon_2}}, \tag{2.26}$$

where $k_0 = \omega/c$ is the magnitude of the wave vector in vacuum. The SPP dispersion relation is plotted in Fig. 2.5 (red line) for the case of gold. We can see that for the long-wavelength limit (small wave vectors), the dispersion relation asymptotically approaches zero, whereas for $k \to \infty$ the dispersion relation asymptotically approaches the energy of the surface plasmon given by $\hbar\omega_{\mathrm{SP}} = \hbar\omega_{\mathrm{P}}/\sqrt{2}$, which can be shown by inserting the Drude dielectric function in the form $\varepsilon_2(\omega) = 1 - \omega_{\mathrm{P}}^2/\omega^2$ and $\varepsilon_1 = 1$ into Eq. (2.26). Furthermore, Eq. (2.26) gives a solution for modes propagating inside the material (blue line) similar to the bulk plasmon polaritons discussed in the previous section (dotted line).

In summary, surface plasmon polaritons are evanescent electromagnetic waves propagating along the metal-dielectric interface connected with collective oscillations of the free

surface charge in metal. The hybrid light-matter character of SPP enables the confinement of light into sub-wavelength volumes [1]. This is caused by the nature of the SPP dispersion relation given by Eq. (2.26), which shows that for a given energy the SPP can have a wavelength much shorter (larger wave vector) than light in free space. However, this also means that the SPP cannot be directly excited by light due to the wave vector (momentum) mismatch. Therefore, to excite the SPP it is necessary to use special experimental configurations (e.g. Otto's [42] and Kretschmann's [43] configurations) or the electron beam.

2.2.4 Localized Surface Plasmon

In the previous section, we dealt with propagating surface waves at the infinite interface of metal and dielectric. Now we focus on the case of surface waves at a spatially restricted interface (e.g., a metal nanoparticle), which allows the formation of resonant modes, the so-called localized surface plasmons (LSPs), connected with natural oscillations of the electron gas confined in the metallic nanoparticle as depicted in Fig. 2.6.

Contrary to the propagating SPP, these localized modes can be excited by a plane electromagnetic wave (here, the spatial confinement of the interface accounts for the momentum mismatch), which represents a planar excitation in the region of the whole nanoparticle, or by an electron beam, which represents a local excitation limited by the range of the electric field of electrons. Due to this, it is possible to map the LSPs using the EELS method with high spatial and spectral resolution. An example of simulated EEL spectra for a gold nanorod is shown in Fig. 2.7(a). The spectra show distinct peaks corresponding to individual longitudinal LSPs excited by the electron beam. These modes can be viewed as standing plasmon polariton waves of certain resonant frequencies. This can be emphasized by plotting the charge distributions of the individual nanorod modes [Fig. 2.7(b)]. As we can see, the first peak ($l = 1$) of the spectra corresponds to a charge distribution with two maxima at the nanorod terminations, resembling the case of an electric dipole, and thus we refer to this resonance as a longitudinal dipole (LD) mode. Higher modes ($l = 2, 3, ...$) exhibit additional maxima and nodes of charge distributions. The charge distributions of the longitudinal quadrupole (LQ) ($l = 2$) and the longitudinal octupole ($l = 3$) are also included. We can distinguish between two types of modes, the so-

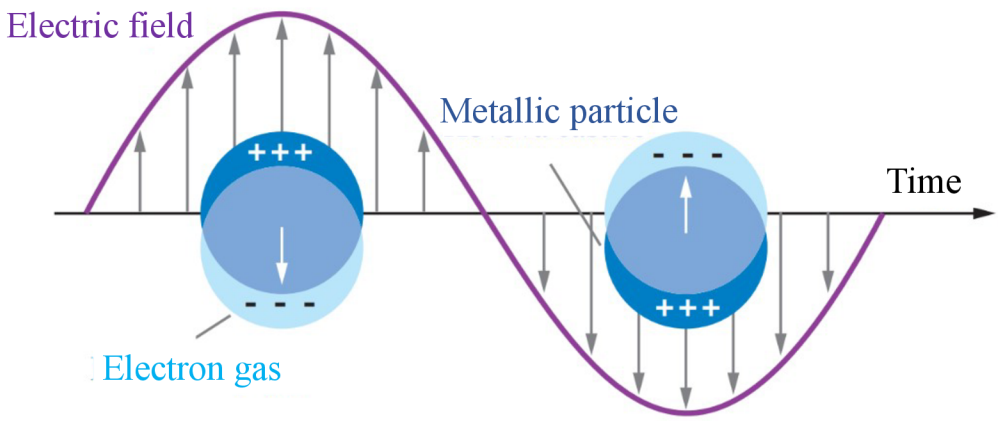

Figure 2.6: Localized surface plasmon in a metallic particle excited by a harmonic electromagnetic field, causing collective oscillations of the free electron gas. Adapted from [44].

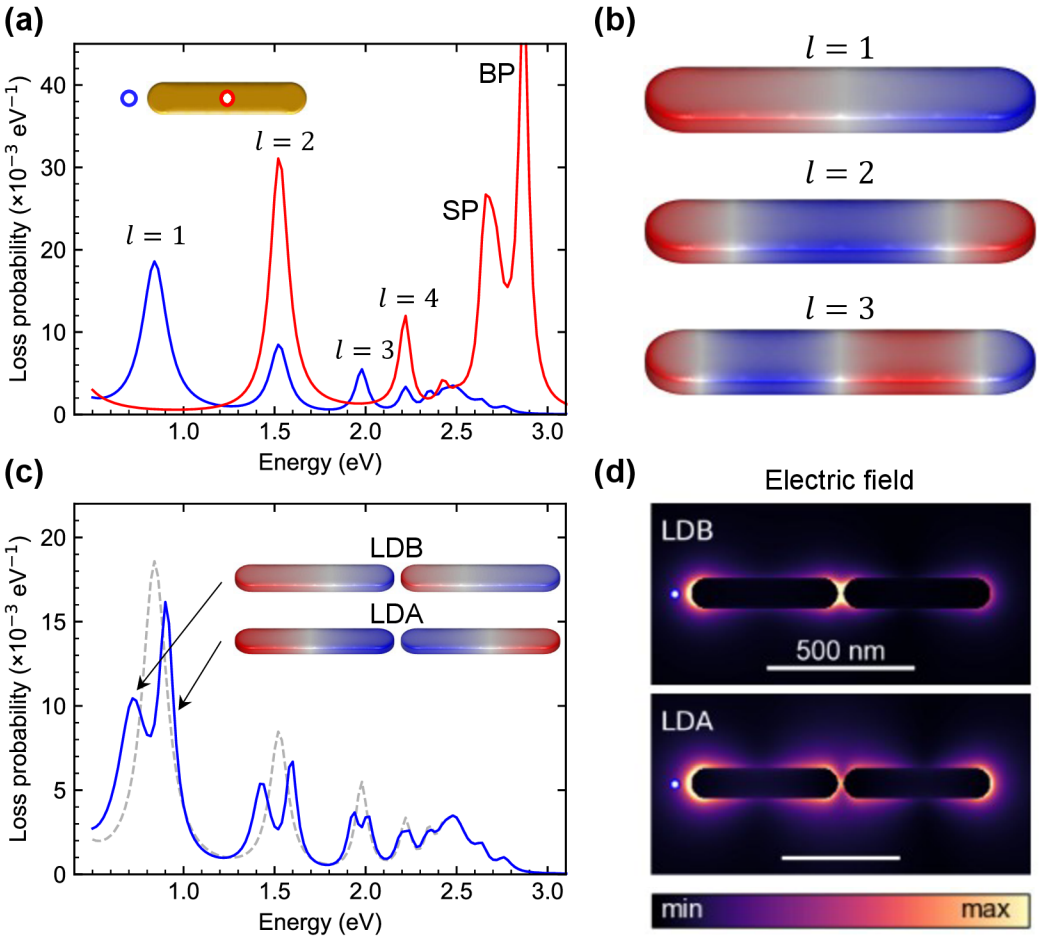

Figure 2.7: (a) Simulated electron energy loss spectra for a gold nanorod of length 500 nm. EEL spectra are calculated for two electron beam positions indicated in the inset, with colors corresponding to the spectra. When the electron beam is placed at the edge of the nanorod, both the bright and dark modes are excited. When the beam is placed in the middle of the nanorod, only dark modes (with even l) appear due to the symmetry of the incident electron field. The last two peaks correspond to material modes, surface plasmon (SP) and bulk plasmon (BP). (b) Charge distributions for the first three LSPs. Red corresponds to a positive charge and blue corresponds to a negative charge. (c) EEL spectra for a nanorod dimer showing the LSP hybridization because of the coupling of the nanorods. Charge distributions of the bonding and antibonding configurations of the longitudinal dipole (LDB and LDA, respectively) are shown. (D) Amplitudes of the total electric field in the xy plane for LDB and LDA modes.

called bright modes and dark modes. Bright modes have non-zero electric dipole moments and can couple to plane waves, meaning that it is possible to excite these modes with electromagnetic plane wave. In the discussed example of nanorod geometry, bright modes correspond to odd-order longitudinal modes (i.e. $l = 1, 3, 5, ...$). Dark modes, on the contrary, have symmetric charge distributions without a dipole moment and thus cannot be excited by light. Dark modes can be probed by strongly confined fields, as is the case of the electron beam, and they are present in the EEL spectra as even modes (i.e. $l = 2, 4, 6, ...$). When the electron beam is placed in the middle of the particle, only dark

modes are excited together with material excitations such as the discussed surface and bulk plasmons [red line in Fig. 2.7(a)].

An important application of LSPs is the ability to confine electromagnetic field to a sub-wavelength scale, focusing it beyond the diffraction limit of light [5]. This effect is accompanied by the formation of a strong field that is confined to the surface of the nanoparticle. This so-called near-field is strongly enhanced compared to incident light, and this is utilized in a wide range of applications, such as spectroscopy and sensing [44], biosensors [45], or photovoltaic devices [46]. A particularly strong field enhancement can be observed in the gap between two coupled plasmonic nanoparticles, called plasmonic dimers. The coupling between nanoparticles is accompanied by the hybridization of single-nanoparticle LSPs, giving rise to the bonding and antibonding configurations of LSP [47]. This results in the splitting of individual LSP peaks in the EEL spectrum, as shown in Fig. 2.7(c). The charge distributions of the longitudinal dipole bonding (LDB) and antibonding (LDA) modes are depicted in the inset. Only the bonding configurations have a net dipole moment and thus can be excited optically (bright modes) [48]. For these configurations, charges with opposite signs accumulate at the nanoparticle terminations in the gap region, causing a strong electric field to appear [Fig. 2.7(d) top panel]. On the other hand, the antibonding configurations have zero net dipole moment and can thus be excited only by strongly confined fields (dark modes). In this case, charges with the same signs accumulate in the gap region and the gap electric field is much weaker [Fig. 2.7(d) bottom panel].

The second aspect of LSP is the conversion of energy from confined fields into propagating waves. This can be achieved by coupling the plasmonic near-field to the electromagnetic fields emitted by atoms, molecules, or quantum dots placed in the vicinity of the nanoparticle. The emission of electromagnetic waves is then strongly enhanced. This has been utilized in surface-enhanced Raman scattering [49], single-molecule fluorescence [6], or strong light-matter coupling [9]. Therefore, near-field enhancement is a key aspect in the design of plasmonic antennas with the best possible performance, which will be addressed in detail in Chapter 3.

LSPs are also utilized to change the local phase of transmitted and scattered waves. In this way, the properties of the transmitted and scattered wavefronts can be controlled by modifying the surface of a substrate with a specific arrangement of plasmonic antennas. These so-called plasmonic metasurfaces can be used, for example, to design ultra-thin optical elements, such as lenses [50].

2.3 Computational Methods in Plasmonics

For the correct interpretation of the experimental data on the optical response of plasmonic particles and materials, analytical models and numerical simulations are important. In addition, simulations can also provide quantities that are hard to observe experimentally (e.g. surface charges and currents). In the case of EELS, analytical methods offer solutions only in a few special cases (e.g., planar surfaces, spheres, or cylinders [51]). For more complex geometries of plasmonic antennas (PAs), which are often encountered in practice, numerical simulations must be used. There are several numerical methods available for simulations of LSP ecitations in PAs, such as the boundary element method (BEM) implemented, for example, in the MNPBEM toolbox for MATLAB available from

[52], the finite element method (FEM) often used in commercial software COMSOL Multiphysics [53], the finite-difference time-domain (FDTD) method implemented e.g. in Ansys Lumerical [54], and others [55, 56]. In this work, most of the simulations are carried out using the MNPBEM toolbox, and thus it is briefly introduced in the following section.

2.3.1 Metallic Nanoparticle Boundary Element Method

The MNPBEM toolbox is based on the boundary element method (BEM), which was adapted to describe EELS by F. J. García de Abajo in collaboration with A. Howie [51]. In BEM, we look for solutions of Maxwell's equations in the form of surface integrals at the interface of two media. The interfaces are discretized (divided) into regions of finite size, the so-called boundary elements. The method is based on the assumption that the media are separated by abrupt interfaces and that individual media are described by homogeneous and isotropic dielectric functions. This assumption may be somewhat limiting, but for most plasmonic applications involving metal nanoparticles placed in a dielectric environment, it is sufficient [57].

The electromagnetic field induced in the nanoparticle by the incident plane wave or an electron is calculated from the surface charges and currents by applying the boundary conditions between the boundary elements. Calculations can be performed within the so-called quasistatic (non-retarded) limit provided that the nanoparticle under investigation is much smaller than the wavelength of the excitation wave. The advantage of the quasistatic approximation is that only the Poisson equation is solved numerically, and the calculations are therefore less demanding. In our case, however, this condition is not satisfied for most particles, and retarded computations solving the full set of Maxwell equations must be employed for the simulations.

Consider nanoparticles described by local and isotropic dielectric functions $\varepsilon_j(\omega)$ separated by abrupt boundaries ∂V_j. We can start by expressing the electromagnetic fields in terms of the scalar and vector potentials, $\phi(\mathbf{r})$ and $\mathbf{A}(\mathbf{r})$, respectively, as

$$\mathbf{E} = \mathrm{i}k\mathbf{A} - \nabla\phi, \tag{2.27a}$$

$$\mathbf{B} = \nabla \times \mathbf{A}, \tag{2.27b}$$

where $k = \omega/c$ is the wavenumber in vacuum. Note that we use the Gaussian unit system throughout this section. For more details on the unit system, see, for example, [39, 40].

Both scalar and vector potentials satisfy the Helmholtz wave equation and are related by the Lorentz gauge condition $\nabla \cdot \mathbf{A} = \mathrm{i}k\varepsilon\phi$. Then we can write the potentials inside each homogeneous region in the form [51, 58]

$$\phi(\mathbf{r}) = \phi(\mathbf{r})_{\mathrm{ext}} + \oint_{\partial V_j} G_j\left(|\mathbf{r}-\mathbf{s}|\right)\, \sigma_j(\mathbf{s})\, \mathrm{d}a \tag{2.28a}$$

$$\mathbf{A}(\mathbf{r}) = \mathbf{A}(\mathbf{r})_{\mathrm{ext}} + \oint_{\partial V_j} G_j\left(|\mathbf{r}-\mathbf{s}|\right)\, \mathbf{h}_j(\mathbf{s})\, \mathrm{d}a, \tag{2.28b}$$

where $\phi(\mathbf{r})_{\mathrm{ext}}$ and $\mathbf{A}(\mathbf{r})_{\mathrm{ext}}$ are potentials produced by the external sources (e.g. plane wave or electron beam) and $G_j(r)$ is the Green's function of the Helmoholtz equation in medium j given by [30]

$$G_j(r) = \frac{\exp\left(\mathrm{i}kr\sqrt{\varepsilon_j}\right)}{r}, \tag{2.29}$$

and σ_j and $\mathbf{h}_j$ are auxiliary interface charges and currents. These quantities are determined by applying the boundary conditions of the electromagnetic field at the interfaces separating the materials, giving a set of integral equations. The interface integrals are then discretized into a number of boundary elements. This leads to a set of linear equations, which can be solved by linear algebra techniques [51].

Simulating EELS

Let us consider a swift electron passing by or through a metallic nanoparticle, exciting LSP resonances. The energies of these resonances are very small compared to the used high-energy electron beam, and we can thus neglect the effect of the lost kinetic energy on the electron trajectory. Assuming that the incident electron travels along the z axis with constant velocity v, it can then be described using the charge distribution along its trajectory as

$$\rho(\mathbf{r},\omega) = -e\int \exp(\mathrm{i}\omega t)\delta(\mathbf{r}-\mathbf{r}_0-\mathbf{v}t)\,\mathrm{d}t = -\frac{e}{v}\delta(\mathbf{R}-\mathbf{R}_0)\exp[\mathrm{i}q(z-z_0)], \tag{2.30}$$

where $\mathbf{R}_0$ is the impact parameter denoting the position of the electron trajectory in the xy-plane and $q=\omega/v$ is the wavenumber.

The electromagnetic field of the incident electron in each medium j is given by the scalar and vector potentials in the form

$$\phi_{\mathrm{ext}}(\mathbf{r}) = -\frac{2}{v\varepsilon_j}K_0\left(\frac{q\,|\mathbf{R}-\mathbf{R}_0|}{\gamma_j}\right)\exp[\mathrm{i}q(z-z_0)], \tag{2.31a}$$

$$\mathbf{A}_{\mathrm{ext}}(\mathbf{r}) = \varepsilon_j\frac{\mathbf{v}}{c}\phi_{\mathrm{ext}}(\mathbf{r}), \tag{2.31b}$$

where $\gamma_j = 1/\sqrt{1-\varepsilon_j v^2/c^2}$ and K_0 is the modified Bessel function of second kind of order zero. These potentials can then be inserted into Eqs. (2.28a)–(2.28b) giving the distributions of σ_j and $\mathbf{h}_j$ at the interfaces.

Thus, the electromagnetic field of the incident electron polarizes the matter in its vicinity, inducing an electric field $\mathbf{E}_{\mathrm{ind}}$, which then acts back on the electron, causing it to lose energy [59]. The electron energy loss can then be expressed as

$$\Delta E = e\int \mathbf{v}\cdot\mathbf{E}_{\mathrm{ind}}(\mathbf{r}(t),t)\,\mathrm{d}t. \tag{2.32}$$

Electron energy loss can also be expressed as the quantum of energy $\hbar\omega$ given to the specimen with a certain probability $\Gamma_{\mathrm{EELS}}(\omega)$. Summing over all ω, we get

$$\Delta E = \int_0^\infty \hbar\omega\,\Gamma_{\mathrm{EELS}}(\omega)\,\mathrm{d}\omega. \tag{2.33}$$

By comparing Eqs. (2.32)–(2.33) and applying the Fourier transform, we obtain the loss probability

$$\Gamma_{\mathrm{EELS}}(\omega) = \frac{e}{\pi\hbar\omega}\int \mathrm{Re}\left\{\mathbf{v}\cdot\mathbf{E}_{\mathrm{ind}}(\mathbf{r}(t),t)\right\}\,\mathrm{d}t. \tag{2.34}$$

The induced electric field $\mathbf{E}_{\text{ind}}$ can be expressed here by substituting the integrals from the equations (2.28a)–(2.28b) into the relation (2.27a). This form of loss probability calculations is commonly used, for example, in the finite element method. Its disadvantage is the necessity of evaluating the induced field sequentially along the entire electron trajectory. In the BEM this can be solved by rewriting it in the form [58]

$$\Gamma_{\text{EELS}}(\omega) = -\frac{e}{\pi\hbar\omega} \sum_j \text{Im} \left\{ \oint_{\partial V_j} \varphi_j(\mathbf{s}) \left[k\mathbf{v} \cdot \mathbf{h}_j(\mathbf{s}) - qv\sigma_j(\mathbf{s}) \right] \text{d}a \right\}, \tag{2.35}$$

where

$$\varphi_j(\mathbf{s}) = \int_{z_j^0}^{z_j^1} \exp\left(-\text{i}qz\right) G_j\left(|\mathbf{r} - \mathbf{s}|\right) \, \text{d}z \tag{2.36}$$

is a potential-like term related to the electron propagation inside a medium j with z_j^0 an z_j^1 being its entry and exit points, respectively. Using Eq. (2.35) the integration is performed only on the boundaries of the discretized object, improving the computational efficiency of the simulations. For more information on simulations using the MNPBEM toolbox, see the related papers by the toolbox authors [57, 58, 60].

3 Plasmonic Lightning-Rod Effect

3.1 Introduction

The lightning-rod effect is a well-known phenomenon in electrostatics characterized by the formation of a strong electric field near the sharp features of a charged conductor. We can illustrate this effect with a simple example depicted in Fig. 3.1. Consider two metallic spheres with radii r_1 and r_2. These spheres are charged with charges Q_1 and Q_2, and are positioned far enough apart that their mutual electrostatic interactions can be ignored. Under these conditions, the charges uniformly distribute across the surfaces of both spheres, resulting in electrostatic potentials $\varphi_i(r)$ and electric fields $E_i(r)$ for each sphere $i = 1, 2$, expressed as

$$\varphi_i(R_i) = \frac{1}{4\pi\varepsilon_0}\frac{Q_i}{R_i},$$
$$E_i(R_i) = \varphi_i(R_i)/R_i = \frac{1}{4\pi\varepsilon_0}\frac{Q_i}{R_i^2}.$$

When the spheres are conductively connected, charges are transferred, leading to equalization of the electrostatic potentials $\varphi_1 = \varphi_2 = c$. Consequently, we can write $\frac{E_1}{E_2} = \frac{R_2}{R_1}$. Given that $R_2 < R_1$ as shown in Fig. 3.1(a), condition $E_2 > E_1$ must hold. Thus, stronger electric fields are formed near the surfaces with higher local curvatures [Fig. 3.1(b)].

The discussed electrostatic example is very illustrative, but it is difficult to fully translate it into the field of plasmonics with electromagnetic fields of very high frequencies ranging typically from the infrared to the visible part of the spectrum, which contrasts with the static fields considered in the given example. Consequently, there are fundamental differences between the electrostatic and plasmonic cases of the lightning-rod effect.

The first important distinction lies in the nature of the electromagnetic fields, which differ already for the simple case of a metal planar sheet, i.e. a surface with zero curvature. In the electrostatic case, the plate has to be charged with a net charge. The charge is distributed uniformly over the surface of the plate, resulting in a homogeneous static electric field in its vicinity [Fig. 3.2(a) left]. In the plasmonic case, the surface plasmon polariton (SPP, discussed in Section 2.2.3) is excited on the metal surface. It is an evanescent electromagnetic wave associated with collective charge oscillations. There is

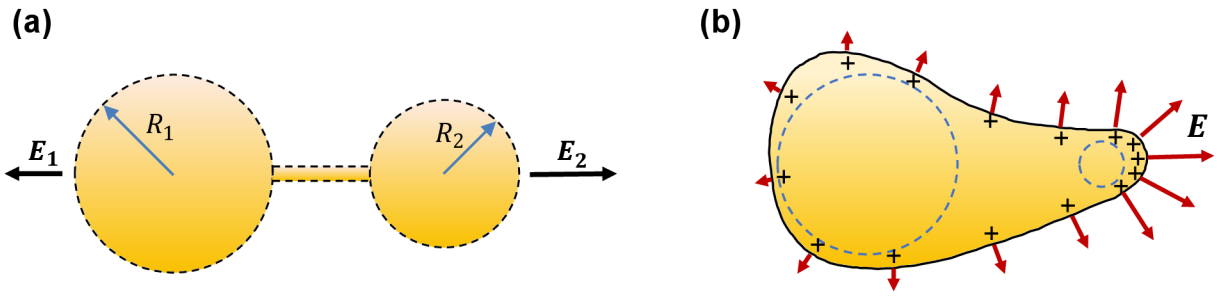

Figure 3.1: Electrostatic lightning-rod effect. (a) Conductive connection of two spheres with different curvatures (radii R_1 and R_2). (b) Formation of a strong electric field near a highly curved metal surface.

a zero net charge associated with the SPP. The amplitude of the electric field decreases exponentially with the distance from the metal-dielectric interface [Fig. 3.2(a) right]. Therefore, these waves naturally confine the electric field into subwavelength dimensions and thus always contribute to the overall field enhancement. This surface wave localization depends on the SPP energy. In general, high-energy SPPs exhibit large field confinements and short propagation lengths, and conversely, low-energy SPPs are less confined and can achieve longer propagation lengths [3].

Secondly, in the electrostatic case, we consider macroscopic metallic particles to which charge is applied from external sources. In the plasmonic case, the charge is represented by an oscillating gas of free electrons in quasineutral PAs (i.e., with zero net charge) driven by an applied external field. The charge is collected (induced) directly from the volume of the PA, which thus serves as a charge reservoir for the excited localized surface plasmon resonance (LSPR). Consequently, the size of the PA (and the charge reservoir) can substantially influence the resulting field enhancement. Intuitively, larger PAs provide larger charge reservoirs and thus can be expected to produce stronger electric fields for a specific excitation.

From the preceding discussion, we can see that there are several partial effects that contribute to the localization of the electromagnetic field in the vicinity of a single plasmonic antenna: surface wave localization, local curvature, and charge reservoir. Furthermore,

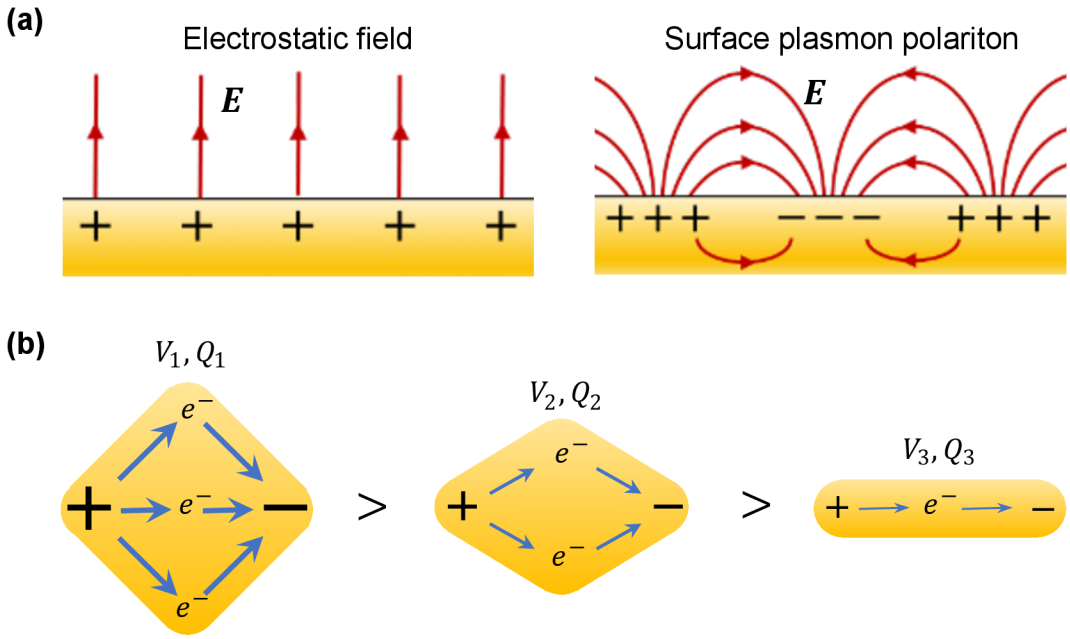

Figure 3.2: (a) Schematic of a homogeneous electrostatic field near a planar charged sheet (left) and evanescent confined field of surface plasmon polariton (right). (b) Schematic illustration of three particles of equal curvature and different volumes, representing an ideal particle set for investigating the charge reservoir contribution to the plasmonic lighning-rod effect. Intuitively, we would expect that more charge can be induced in the particle with the larger charge reservoir (left) and the resulting field enhancement given by the LSPR will be stronger for this particle than for the particles with smaller reservoirs (middle and right).

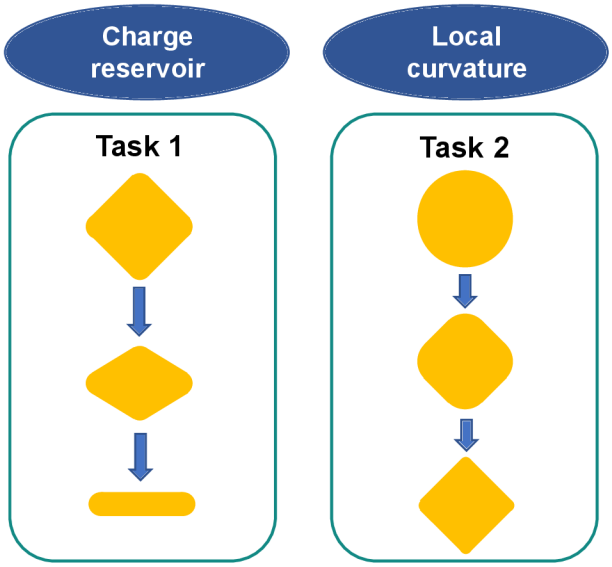

Figure 3.3: Schema of the designed sets of plasmonic antennas for the study of partial effects contributing to the field enhancement: the charge reservoir and the local curvature of the PA.

field enhancement and localization are particularly strong in plasmonic gaps between two coupled PAs, giving rise to an additional effect that contributes to the PLRE, the dimer (plasmonic gap) interaction.

In order to study these effects individually and evaluate their partial contributions to the PLRE, we present a set of studies (tasks) that address particular PLRE effects or their combinations. Each study comprises a set of plasmonic antennas designed to assess these effects.

Task 1 deals with the contribution of the charge reservoir by investigating a set of PAs with different volumes or more specifically, a set of planar PAs with different area/cross sections. By keeping the curvatures and energies of LSPR constant for all the PAs, we can isolate and quantify the contribution of the charge reservoir to the PLRE.

In task 2, our objective is to explore how the local curvature of a PA affects the PLRE. To achieve this, we examine a series of PAs whose curvatures vary from a disc shape to a square shape, while maintaining nearly the same volumes and LSPR energies.

3.2 Methodology

3.2.1 Fabrication of Plasmonic Antennas

For the preparation of PAs, we utilized focused ion beam (FIB) lithography, which consists of only two steps: the deposition of a thin metal layer on a suitable substrate and the subsequent fabrication of structures by local FIB milling illustrated in Fig. 3.4(a). This method offers a relatively high precision for PA fabrication (on the order of tens to units of nanometers [61]). In contrast with alternative PA fabrication techniques such as electron beam lithography (EBL), FIB is less lithographically complex, which reduces the risk of mechanical or chemical damage to the sample and also the overall time consumption. The

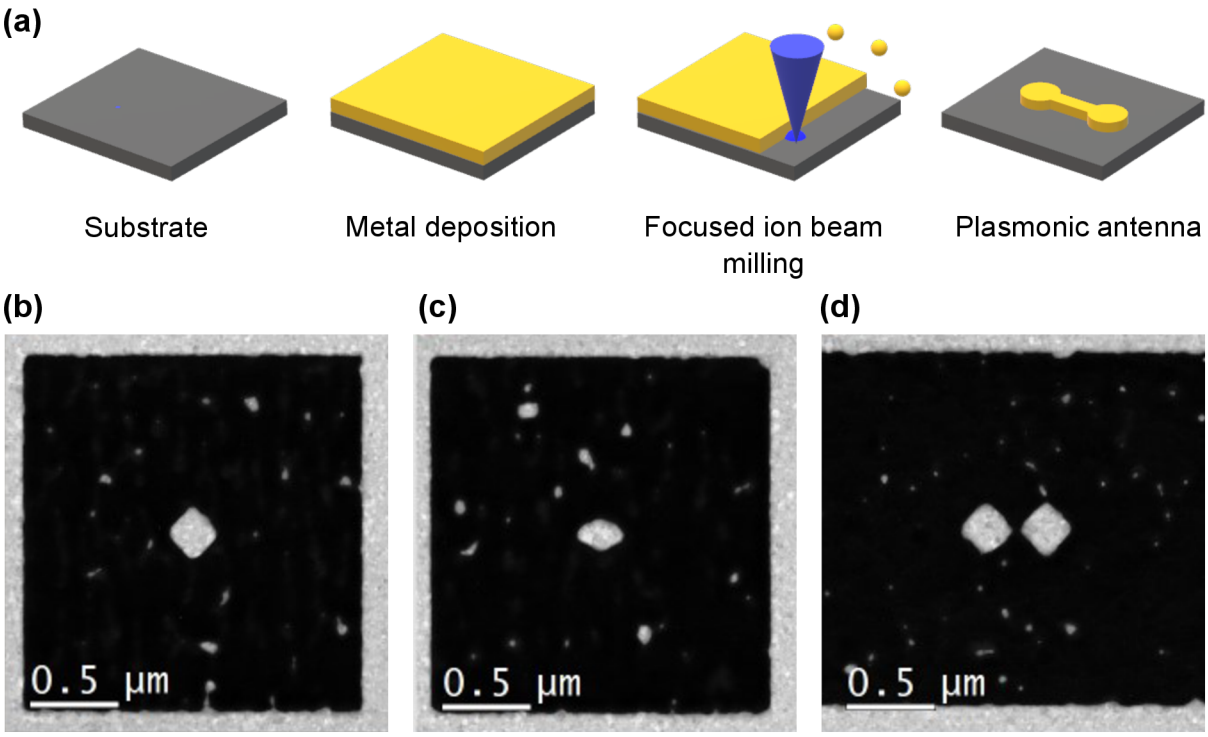

Figure 3.4: (a) Schematic overview of the fabrication process of plasmonic antennas by the ion beam lithography. The grey background indicates the SiN membrane, the gold layer is marked with yellow color, and the ion beam is shown in blue. (b–d) Examples of successfully fabricated plasmonic antennas.

optical and structural properties of the PAs prepared by FIB are sufficiently good for our study of the PLRE.

We chose gold as the primary plasmonic material for our research because of its chemical stability, resistance to oxidation, and relative ease of thin-film preparation. Gold was deposited on the silicon nitride membrane for TEM (provided by Agar Scientific) with a thickness of 30 nm. The gold layer deposition was performed by ion beam assisted deposition (IBAD) using the custom-built deposition chamber equipped with the Kaufman ion source [62], located in the clean laboratories of the Institute of Physical Engineering FME BUT Brno. The argon working gas is introduced into the chamber and ionized by electrons thermally emitted from the heated filament, and the generated argon ions are accelerated by an applied voltage towards a target covered with a gold foil. The sputtered gold atoms then form a polycrystalline layer on the substrate embedded in the chamber. The layer thickness and the deposition rate can be monitored during the deposition process using a quartz crystal microbalance monitor. The deposition rate can be controlled by the flow rate of the argon gas, the discharge current, and the accelerating voltage of the ions. A thin gold layer with a thickness of 30 nm was deposited on the silicon nitride membrane at a deposition rate of 1 Å/s. The chosen deposition rate was optimized for preparing PAs via this technique, as determined by our group's investigation of the morphology of the gold layer and the plasmonic properties of the resulting PAs in a recently submitted publication.

Plasmonic antennas were fabricated using Tescan Lyra 3 dual beam FIB/SEM microscope located in shared laboratories CEITEC Nano Research Infrastructure in Brno. This instrument combines a scanning electron microscope with a gallium ion source and ion beam optics capable of forming high-energy ion beams up to 30 keV and ion currents ranging from 1 pA to 40 nA. The FIB column is tilted at an angle of 55° to the SEM column, and the working distance is 9 mm with respect to the termination of the SEM column. The sample must be placed in this position and tilted perpendicular to the ion beam.

Before starting the PA fabrication, the chamber was cleaned with plasma (20 minutes in high vacuum mode) to limit the presence of organic contaminants inside the chamber that contaminate the resulting PA. During fabrication, the highest possible accelerating voltage of the ion beam (30 keV) and the lowest possible ion current (1 pA) were used. Under these conditions, the ion beam has the smallest spot size, thus obtaining the best spatial resolution of the milling and fabrication precision. Typical dimensions of fabricated PAs ranged from 100 nm to 300 nm. For such dimensions, the energy range of the investigated LSPRs spans from 0.5 eV, the detection threshold of our STEM-EELS, to approximately 2 eV, corresponding to the onset of the interband transitions in gold. The desired PA dimensions and the FIB milling parameters are defined in the microscope software. The PAs are then created by computer-controlled FIB milling over a defined area around the PA (typically a 2×2 µm^2 square or larger rectangle[1]), removing the surrounding gold layer while the PA itself remains intact. Individual grains can be sputtered at different rates, so some of them cannot be fully removed with a given dose of ions. Incompletely removed grains present an undesired modification of the dielectric environment of PAs or even affect its shape[2]. This problem cannot be solved simply by increasing the ion dose, as the gold layer is located on a membrane of very small thickness (30 nm). Increasing the ion dose may cause local damage or complete rupture of the membrane. The optimal dose of ions to sufficiently remove the surrounding gold layer must be determined experimentally. Fig. 3.4(b–d) shows some examples of successfully fabricated PAs.

3.2.2 Structural and Elemental Characterization

The structural properties of the thin gold film were locally studied by transmission electron microscopy using selected area electron diffraction (SAED) and STEM imaging, introduced in Section 1.3.

Fig. 3.5(a) shows the SAED pattern of the gold layer taken from a region of approximate size 9 µm^2. The diffraction pattern consists of individual diffraction rings, which demonstrates the polycrystalline nature of the gold layer. Because the studied region is relatively large and includes many randomly oriented grains, the intensity of the diffraction rings is nearly continuous and radially symmetric. The diffraction pattern was processed using a free CrystBox software package [63]: the beam stopper projection was removed from the pattern, the background was subtracted and the diffraction rings were indexed. Some of the diffraction rings are indexed in Fig. 3.5(a). We found a systematic disagree-

[1] The metal-free area has to be large enough to prevent the coupling between the PA and the surrounding metallic frame.

[2] The residual grain located sufficiently close to the antenna can also influence the LSPR supported by PA. Therefore, EELS measurements were performed only for PAs surrounded by small grains (with high LSPR energies in the region of material interband transitions) or larger grains far apart from the PA.

ment between the interplanar distances experimentally determined from SAED patterns and theoretically predicted. This is probably caused by an inaccurate calibration of the camera length of the microscope, and therefore the experimental spectrum was calibrated by a factor of 1.09. The calibrated experimental DP, after background subtraction and beam stopper removal, is displayed in Fig. 3.5(b) on the right, along with the theoretical ring pattern for gold on the left, showing good qualitative agreement.

The STEM [BF in Fig. 3.5(c) and HAADF in Fig. 3.5(d)] images show in detail the polycrystalline gold layer and its individual grains. The grains show distinct boundaries and exhibit random orientations, resulting in the predominant diffraction contrast (opposite for BF and HAADF). Importantly, the gold layer is continuous without any major protrusions or cavities, which is crucial for PA fabrication. Note that the polycrystallinity of the gold layer does not negatively affect the plasmonic properties of PAs compared to monocrystalline gold, as investigated in [64].

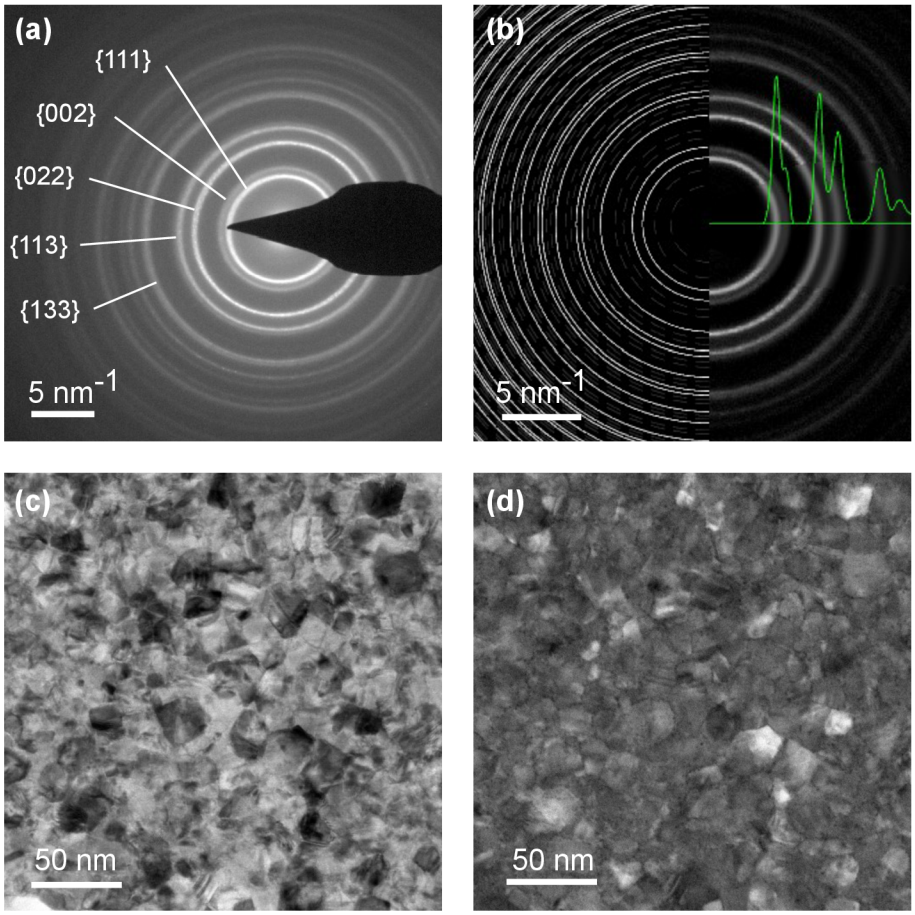

Figure 3.5: (a) Recorded SAED pattern from the golden layer. (b) Processed SAED pattern from (a) on the right compared to the theoretical ring pattern for gold on the left. The post processing includes the background and beam blocker subtraction. The recorded SAED pattern was calibrated by a factor of 1.09 for the comparison with the theoretical pattern. The green lines represent the integrated radial intensity of the pattern. (c) STEM BF micrograph and (d) HAADF micrograph of the gold layer.

The structural properties and dimensions of the fabricated PAs can be assessed directly from STEM micrographs. The thickness profiles of PAs can be determined using the EELS thickness mapping method described in detail in Section 1.3.4. The relative thickness of PA can be determined from the measurements rather reliably. However, to determine the absolute thickness of the PA we need to obtain the inelastic mean free path (IMFP) λ of electrons in gold [see Eq. (1.11)]. The IMFP for a specific material and the EELS settings can be determined using the EELSTools software by D. Mitchell [65], which incorporates the algorithm developed by K. Iakoubovskii et al. [66]. For our EELS settings, with an electron energy of 120 keV, a convergence semi-angle of 10 mrad, and a collection semi-angle of 11.4 mrad, the calculated IMFP for gold is 78 nm. With this value, thickness mapping of the produced PAs via EELS can be performed. An example of thickness cross sections is shown in the bottom panels of Fig. 3.6 for the case of PA shown in the upper left panel. The thickness cross sections show that the edges of the antennas are inclined, which can be attributed mainly to the finite size and the Gaussian profile of the ion beam during fabrication. The surface of the particle is also relatively rough, as the estimated thickness profile ranges between 30 nm and 50 nm. The average value of the thickness of these profiles is approximately 37 nm. Therefore, this value exceeds the nominal value of the thickness of the gold layer, which was set to 30 nm. However, it should be noted that the EELS thickness measurements are influenced by the limited

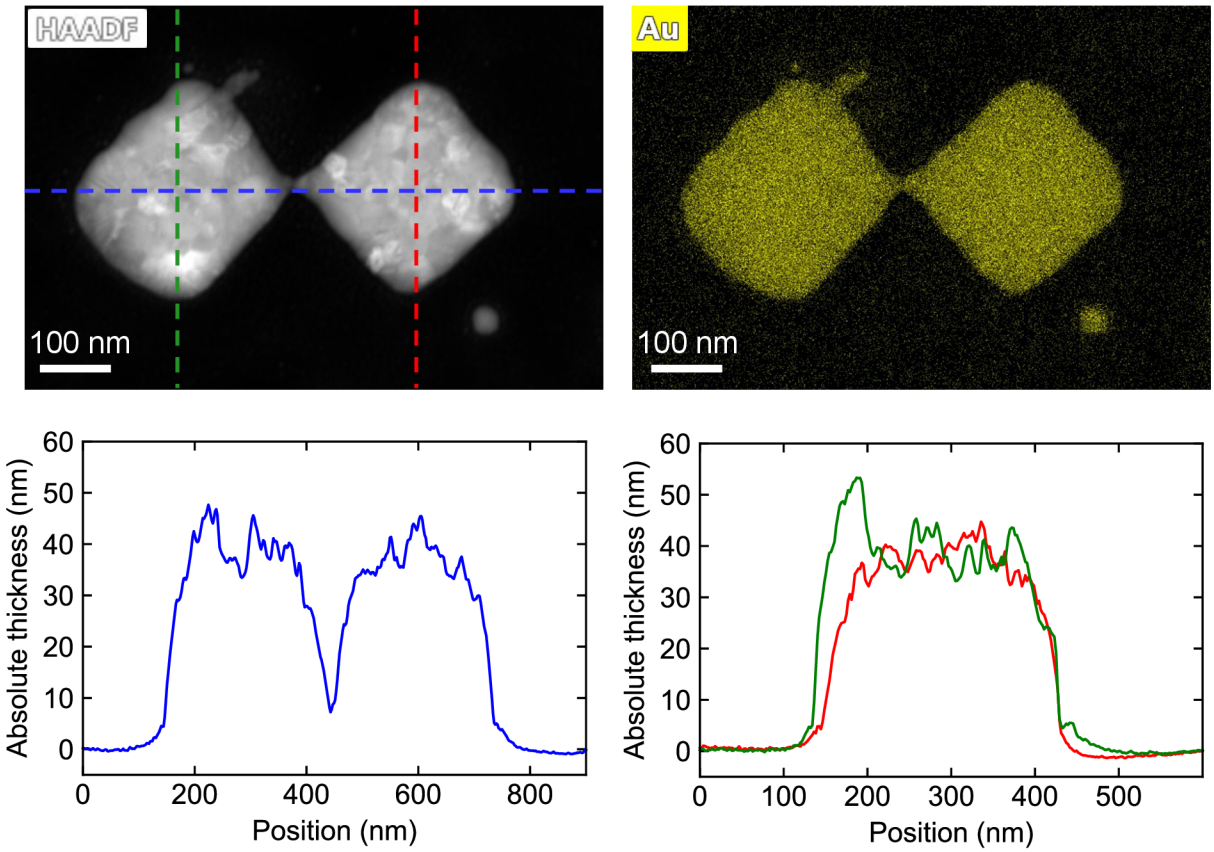

Figure 3.6: Top left panel: HAADF micrograph of the characterized PA. Top right panel: EDS elemental map for Au. Bottom panels: The thickness profiles of the PA along the lines shown in the top left panel with corresponding colors.

experimental precision of EELS and the uncertainties associated with the establishment of IMFP, which have an estimated error of 20 % [67]. Furthermore, the measured thicknesses may also be exaggerated as the membrane surrounding the PA may have been partially removed during the FIB lithography .

Energy dispersive X-ray spectroscopy (EDS) can be utilized to quantitatively study the elemental composition of PAs, including possible contaminants such as hydrocarbons or ions implanted during the fabrication process. EDS measurements were performed using the TEM FEI Titan equipped with the Super-X spectrometer located in the shared laboratories CEITEC Nano Research Infrastructure in Brno. The microscope was operated at 300 keV in scanning mode. The probe current was set to 0.5 nA. EDS spectrum image was acquired and processed in Velox software. The spectrum image was obtained by integrating 100 frames taken with a dwell time of 10 µs. In this way, the individual frame time is only a few seconds, which allows the drift correction to be applied correctly. The background of the EDS spectra was fitted using the parabolic model and quantification was performed using the Brown-Powell model (based on empirical data) which yields the atomic and weight fractions with estimated errors for each selected element.

EDS spectra were integrated from the entire spectrum image and the major peaks corresponding to the following chemical elements were identified: Au forming the PA, Si and N forming the membrane, C and O as frequent contaminants and Ga resulting from ion implantation during PA fabrication by FIB. A minor contribution of Cu was detected. Copper is a common spurious signal in the TEM EDS most likely originating from the specimen holder, and thus was not taken into account in the elemental quantification. Argon, which could be implanted in the gold layer during deposition, was not detected. The elemental quantification yields the following atomic fractions (in atomic percents): Au (14 ± 3) %, Si (39 ± 10) %, N (27 ± 7) %, C (9 ± 1) %, O (9 ± 2) %, Ga (1.0 ± 0.2) %.

We can notice relatively high atomic fractions of contaminants, (9 ± 1) % for carbon and (9 ± 2) % for oxygen. Carbon contamination is likely to originate from the FIB chamber, which may remain partially uncleaned even after plasma cleaning. It should also be noted that the EDS measurements were performed after the EELS measurements, during which a carbon layer is often formed on the surface of the sample. The sample was also exposed to the atmosphere between the measurements. To reduce the effect of carbon contamination, the sample can be plasma-cleaned directly in the TEM holder prior to the EELS measurements and other investigations. Importantly, the fabrication process does not substantially degrade PAs with the implantation of gallium ions [(1.0 ± 0.2) %]. Furthermore, gallium ions are deposited primarily in areas of the membrane, which was directly exposed to the ion beam during fabrication [67].

3.2.3 Electron Energy Loss Spectroscopy Measurements

EELS measurements were performed in a scanning transmission electron microscope FEI Titan equipped with a GIF Quantum spectrometer (discussed in Section 1.2.5) by Dr. Michal Horák. The processing of the experimental data was then fully performed by the author of the thesis. The microscope was operated at 120 keV in the scanning monochromated mode, with a convergence semi-angle set to 10 mrad and a collection semi-angle set to 11.4 mrad. These experimental settings are optimized for the low-loss EELS characterization of PAs as studied in [68].

When measuring EELS in STEM mode, the electron beam is scanned over a defined area of the sample, and the loss spectrum is recorded on the CCD camera at each beam position. The measured area must include the antenna itself and also a sufficiently large area of the surrounding membrane for background subtraction [Fig. 3.7(a)]. The outcome of the measurement is the so-called spectrum image (SI), which represents a three-dimensional data set (also known as a data cube). Each pixel of this data cube is correlated with the beam position and contains the corresponding recorded loss spectrum. The spatial resolution of the EELS data cube corresponds to the pixel size, which was set to 2 nm. Spectra were recorded with a spectrometer dispersion of 0.01 eV per channel and the full-width at half-maximum of the zero-loss peak was found in the range from 0.09 eV to 0.12 eV. The raw data contain electron counts recorded by the CCD camera. To obtain the loss probability, the data must be divided by the total number of electrons impinging the sample. However, this approach is not feasible, so instead we normalize the spectra using the electron counts from the zero-loss peak (with an energy integration window set between −1 eV and 1 eV), which reasonably approximates the total electron counts. Thus, we obtain a quantity proportional to the loss probability. This quantity is then divided by the energy interval of the spectrometer channel (0.01 eV) to calculate the loss probability density, also known as the loss function. The loss function is com-

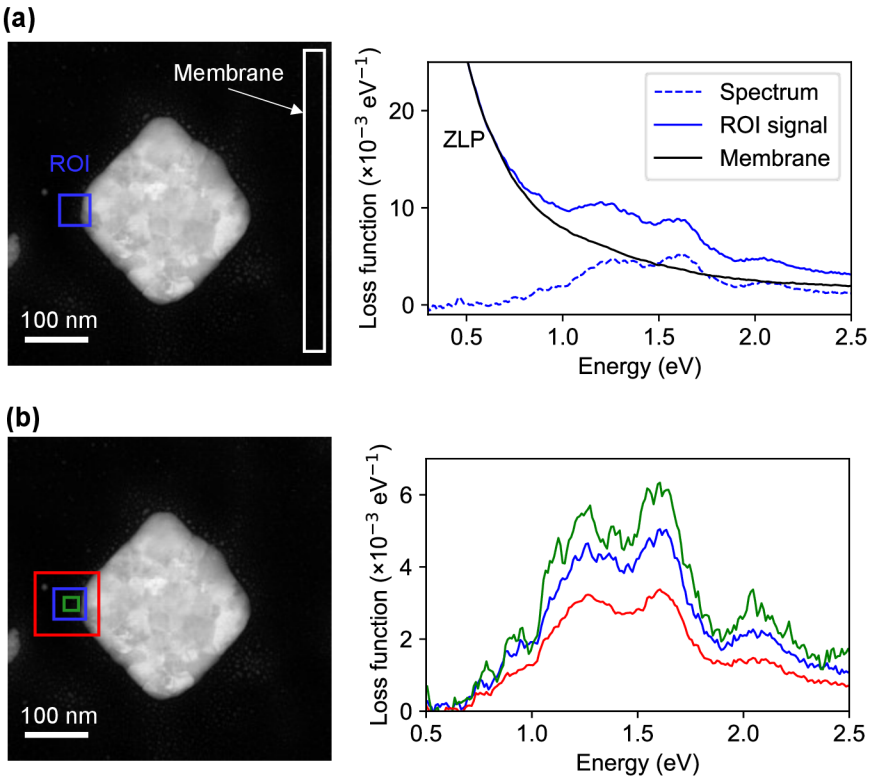

Figure 3.7: (a) Experimental EEL spectra processing. LSPR spectrum (blue dashed line) is obtained by subtracting the membrane signal (black line) representing the bacground from the ROI signal (blue line). (b) The effect of the ROI size on the intensity and the noise of the EEL spectrum. Left panels: HAADF micrographs of the square-shaped PA indicating the areas for the EEL spectra extraction. Right panels: EEL spectra with colors corresponding to the indicated areas.

monly used to represent the EEL spectra and is also directly obtained from numerical simulations [Eq. (2.35)].

The spectra can be extracted from individual pixels of the data cube. However, to suppress noise and random effects associated with manufacturing inaccuracies (such as imperfectly sputtered grains, different membrane thicknesses, possible damage to the membrane, etc.), it is useful to integrate spectra from larger areas. The extraction of spectra is illustrated in Fig. 3.7(a). The left panel displays a HAADF micrograph of the analyzed antenna, highlighting specific areas for spectrum integration. A blue square indicates the region of interest (ROI) where a strong LSPR signal is expected. The white rectangle identifies the membrane area chosen for ZLP and background subtraction. We choose the membrane area as large as possible to account for potential background variations arising from the mentioned manufacturing inaccuracies. Furthermore, this area is located far from the PA to ensure that the LSPR signal is not included in the background. The integrated spectra from these regions are shown in the right panel of Fig. 3.7(a). We can see that the LSPR contribution to the ROI signal (blue line) is very weak compared to the ZLP and also overlapping with its tail. Considering that the membrane signal (black curve) accurately reflects the background in the considered energy interval, it can be directly subtracted from the ROI signal to obtain the pure LSPR contribution (blue dashed line). For a quantitative comparison of the experimental and simulated loss spectra, it is important to also consider the size of the ROI. The ROI has to be small to correspond well to the precise (point-like) electron beam position utilized in the numerical simulations. A comparison of the loss spectra (right panel) obtained from three ROIs of different sizes is shown in the right panel of Fig. 3.7(b). The regions are marked with the corresponding colors in the left panel of Fig. 3.7(b). We observe a reduction of the random noise with increasing the size of the ROI. Simultaneously, the intensity of the (spatially-averaged) loss function is reduced, reflecting the spatial dependence of the

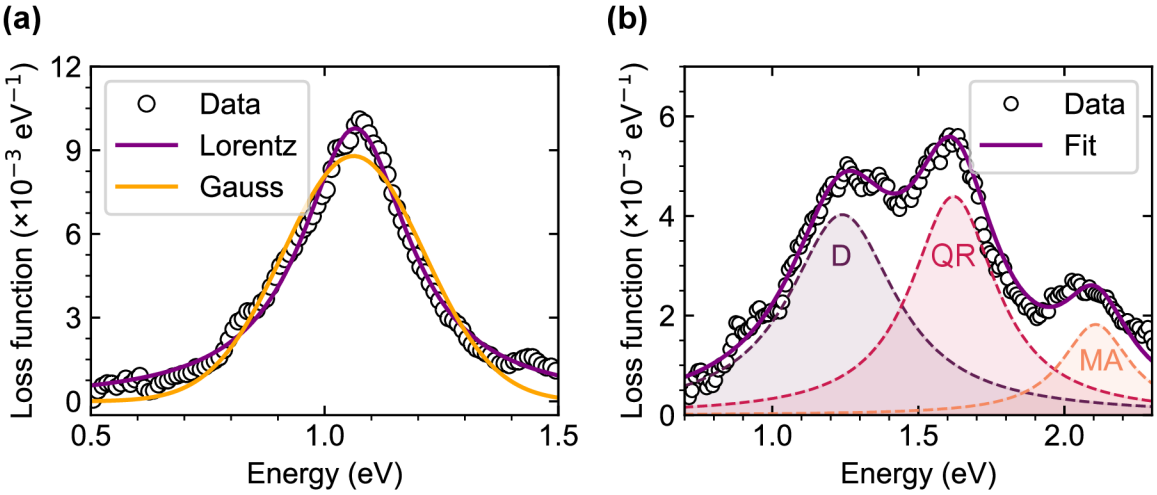

Figure 3.8: Fit of the experimental spectra. (a) Experimental LSPR peak fitted with a Lorentzian function (purple curve) and a Gaussian function (orange curve). (b) Sequential fitting of the experimental data with Lorentzians. The spectrum is decomposed into three peaks corresponding to the dipole (D) LSPR, the quadrupole (QR) LSPR, and the residual multimodal assembly (MA).

actual loss function. It seems that the medium-size (blue) ROI of 50×50 nm^2 represents a reasonable optimum with sufficiently suppressed noise and still not too much influenced intensity of the loss function.

To determine the parameters of individual LSPRs and disentangle overlapping LSPRs, we fit the experimental spectra with a suitable spectral profile. The fit parameters are then used to describe the intensity of the corresponding peaks, their central energies, and FWHM. Fig. 3.8(a) shows a typical loss function peak representing a single LSPR (circles) fit with a Lorentzian function (purple curve) and a Gaussian function (orange curve). The Lorentzian function produces a better fit for most experimental and theoretical spectra, and it will be thus used throughout this work. The experimental spectrum shown in Fig. 3.8(b) is contributed by multiple LSPR. It can be decomposed into individual peaks by sequential fitting of Lorentzians [Fig. 3.8(b)]. In doing so, we obtain three distinct peaks. The first two correspond to individual LSPRs, namely, the dipole (D) LSPR and the quadrupole (QR) LSPR. The intensity of the third peak is influenced by the onset of interband absorption in gold. The nature of the last peak is not always easy to determine. It is likely to include contributions from the heaxapolar LSPR and possibly other higher-order modes, thus we will refer to it as the multimodal assembly (MA) [69].

The spatial distribution of the LSPR signal can also be retrieved from the EELS data cube. This can be done simply by imaging a specific energy slice of the data cube corresponding to the resonance energy. This image is likely to exhibit substantial experimental noise. To reduce this noise, the data cube can be integrated across a certain energy window centered around the LSPR energy. We utilize the width of the integration window of 0.1 eV, as it results in decent noise suppression while maintaining a sufficient spectral resolution. Subsequently, this map is divided by a ZLP map, acquired by integrating from -1 eV to 1 eV. The result is the so-called EEL map, which shows the spatial distribution of the loss probability for a specific LSPR. Examples of EEL maps produced in this way for a diamond-like PA are shown in Fig. 3.10(b–d) for the cases of dipole LSPR [Fig. 3.10(b)], quadrupole LSPR [Fig. 3.10(c)] and multimodal assembly [Fig. 3.10(d)] discussed in Fig. 3.8(b).

3.2.4 Theoretical Modeling

Theoretical modeling is essential in our analysis of LSPRs and the plasmonic lightning-rod effect. Simulations provide verification of the EELS experiments, help with the interpretation of the observed phenomena, and also allow for the retrieval of quantities which are experimentally difficult to obtain, such as the induced electromagnetic fields. In our study, we simulate EELS experiments using the MNPBEM toolbox for MATLAB, which has been described in detail in Section 2.3.1.

In all simulations, the antennas have been represented by gold particles of various shapes such as squares (diamond PA), rods or discs with precisely defined geometries. The dielectric function for gold was taken from [41]. To more accurately simulate the experimental conditions, the PA may be placed on a 30 nm thick silicon nitride membrane, represented by two parallel plates. The dielectric function of silicon nitride can be approximated in the considered spectral region by a constant $\varepsilon_\mathrm{m} = 4$ [70]. To calculate the loss spectra, it is necessary to define the energy of the electron beam (120 keV) and also its position relative to the PA (usually positioned 20 nm away from the PA's boundary).

We first discuss the comparison of the PA model on the membrane and the PA model without the membrane. For this comparison, the loss spectrum was calculated for the case of a diamond-shaped PA with a diagonal length of 300 nm, which is shown in the inset of Fig. 3.9(a). The electron beam was placed outside the antenna at a distance of 20 nm from its corner (indicated by the blue dot).

Let us first focus on the case without membrane [Fig. 3.9(a)]. If we compare the calculated spectra (blue lines) and experimental spectra (red lines), we can state the following: (1) The calculated spectrum is approximately 0.15 eV blue shifted with respect to the experiment.(2) The first two LSPR peaks are slightly more separated in the calculated spectrum (0.44 eV) than in the experimental spectrum (0.36 eV). (3) The calculated spectrum has higher peak intensities, which is evident especially for the 2nd peak corresponding to the quadrupole LSPR. The calculation does not include the finite instrumental spectral broadening. To account for the instrumental broadening, it is reasonable to convolve the numerical loss spectra with a Gaussian of a linewidth corresponding to the FWHM of the ZLP (here set to a slightly higher value of 0.15 eV), mimicking the instrumental broadening. The convolved spectrum (green line) resembles the experimental spectrum reasonably well, except for a certain energy shift which might be attributed primarily to the neglection of the substrate. To facilitate the comparison of both dependencies, we applied a constant energy shift of 0.2 eV to the convolved spectrum; the resulting spectrum (green dashed line) reproduces the experimental spectrum very well.

Similar analysis can be carried out for the case of PA on the membrane [Fig. 3.9(b)]. The following differences can be observed: (1) The calculated spectrum is red shifted by approximately 0.1 eV with respect to the experiment. This energy shift might be caused e.g. by differences between the real and model dimensions of the PA or differences between the real and model dielectric functions. (2) The peaks in the calculated spectrum are slightly less separated (0.28 eV) compared to the experimental spectrum (0.36 eV). (3)

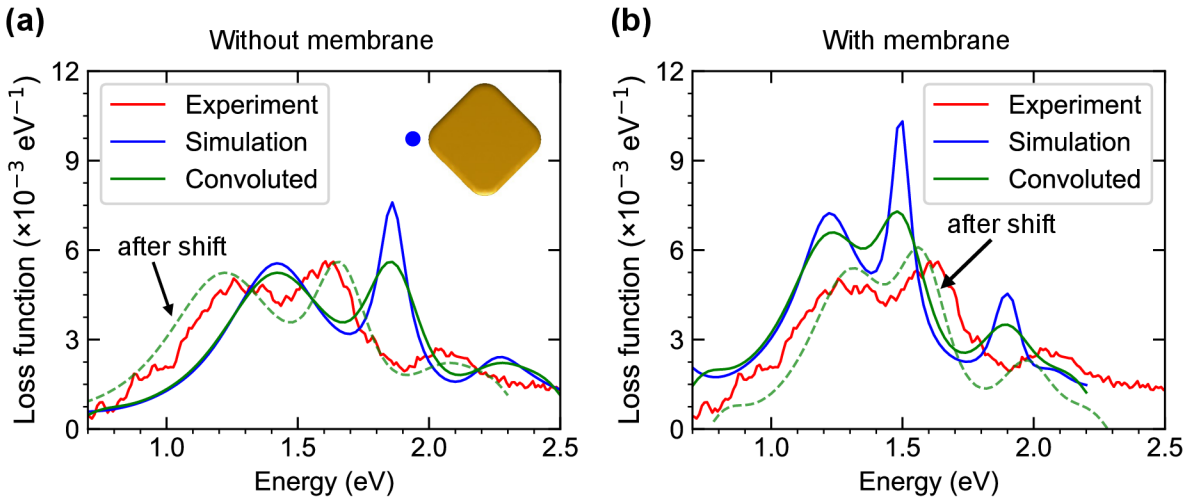

Figure 3.9: Comparison of experimental EELS spectrum (red lines) with simulated spectra (blue lines) for two models: (a) PA without the membrane and (b) PA on a membrane. The electron beam position is indicated in the inset (blue dot). The calculated spectra were convolved with a Gaussian (full width at half maximum 0.15 eV, green line) and shifted for the comparison (green dashed line).

The calculated spectrum has a larger background signal, which is in the experimental case subtracted with the membrane signal. The calculated spectrum is again convolved with the Gaussian (green line) and shifted in both energy (by 0.1 eV) and intensity (by 2×10^{-3} eV^{-1}) to facilitate the comparison for comparison with the experiment (green dashed line).

In conclusion, the intensities and spectral profiles of the LSPR peaks for the case of a particle without a membrane correspond better to the experimental peaks. The inclusion of the membrane causes a red shift of the whole spectrum, which results in a better match of the spectral positions of the peaks with the experiment. However, note that the spectral positions of the LSPR peaks are also highly influenced by the precise PA geometry and, likely, by a different dielectric function of our gold. It can be affected not only by the length of the PA but also by its other dimensions such as the width, thickness, and even the curvature of its corners, as will be shown later in this work. We will use

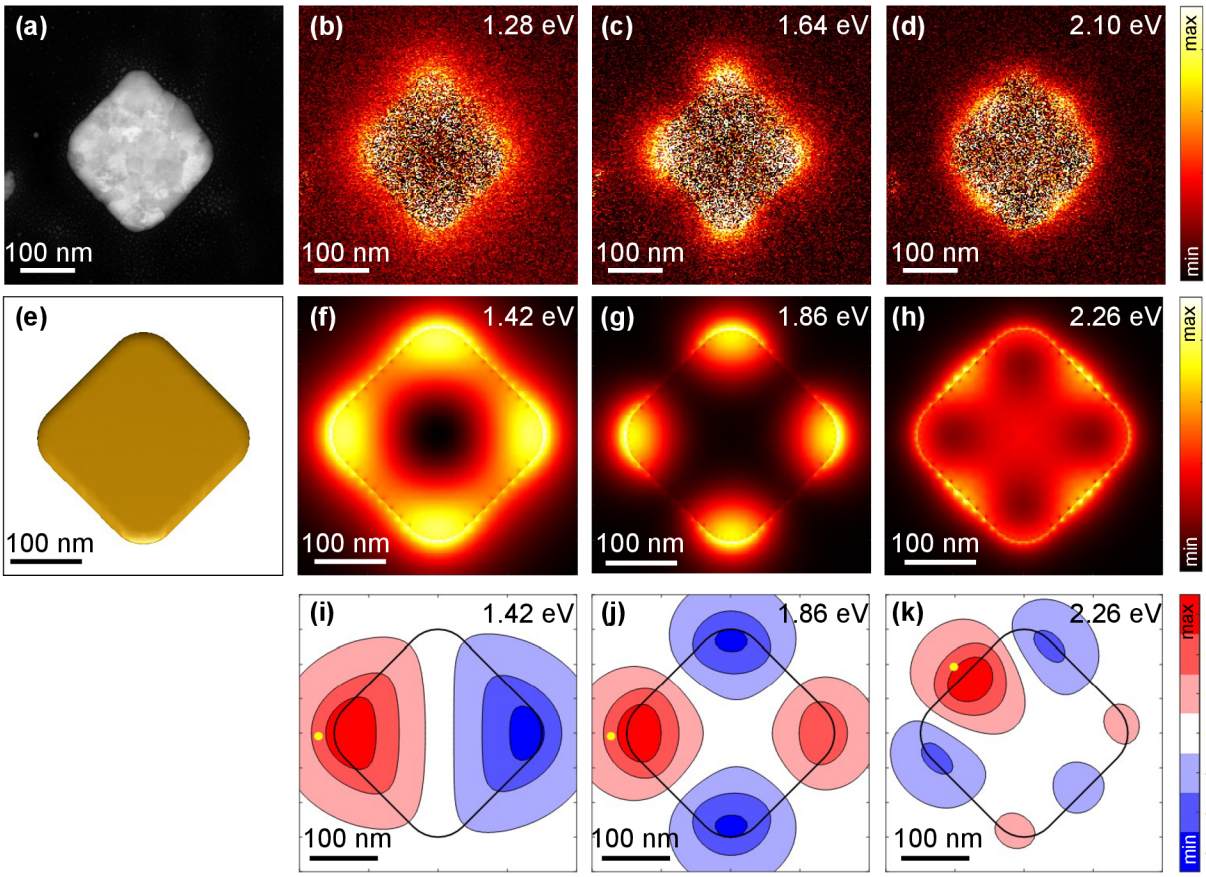

Figure 3.10: (a) HAADF micrograph of the square-shapedPA. (b–d) Experimental EEL maps corresponding to the dipole LSPR (b), the quadrupole LSPR (c), and the multimodal assembly (d). (e) The PA model for numerical simulations. (f–h) Simulated EEL maps at the energy of the dipole LSPR (f), the quadrupole LSPR (g), and the multimodal assembly (h). (i–k) Imaginary part of the out-of-plane component (parallel to the electron beam) of the induced electric field 50 nm above the PA for the dipole LSPR (i), the quadrupole LSPR (j), and the multimodal assembly (k). The electron beam position is marked with a yellow dot.

the membrane-free model of the PA in all presented simulations, which will also result in higher numerical stability of the calculations. The spectra will always be convolved with a Gaussian to mimic the experimental broadening, and the individual LSPR peaks will be fitted with Lorentz curves similar to the experimental spectra in Fig. 3.8(b).

In addition to loss spectra, we can also simulate EEL maps. In these simulations, the electron beam position is varied across the PA. At each beam position, the loss probability is calculated for a given LSPR energy. This results in the creation of spatial maps of the loss probability. For the diamond-like PA discussed above, the calculated EEL maps for three resolved LSPR are shown in Fig. 3.10(f–h) and compared to experimental EEL maps shown in Fig. 3.10(b–d). We observe good qualitative agreement between the experimental and the theoretical maps. The dipole LSPR [Fig. 3.10(b,f)] and the quadrupole LSPR [Fig. 3.10(c,g)] are most intense at the corners of the diamond PA, while the quadrupole LSPR signal is more localized. This might be attributed to the higher LSPR energy and thus the higher localization of the plasmonic fields. We note that the EEL maps of distinct LSPR are often rather similar and do not provide clear information for the identification of the LSPR, particularly in the case of experiment where these LSPRs significantly overlap. Therefore, we can employ numerical simulations for the retrieval of the maps of induced electric fields, which provide additional information on the nature of the LSPR and allow their identification as dipole, quadrupole, and others.

Fig. 3.10(i–k) shows such maps for the imaginary part of the induced electric fields parallel to the electron beam. The position of the electron beam is indicated by the yellow dot. In these electric field maps, the modes can be easily distinguished. The dipole LSPR corresponds to the longitudinal oscillations of the electron gas throughout the PA, and thus opposite charges accumulate at the PA corners inducing fields with opposite signs [Fig. 3.10(i)]. The quadrupole LSPR exhibits additional maxima of the induced field at the remaining two corners of the PA, and also an additional charge nodal plane [Fig. 3.10(j)]. The third field map might partially correspond to the octupole LSPR but might contain contributions from several LSPRs.

In our study of PLRE, we focus on the dipole LSPR. This LPSR is important from the application point of view due to its net dipole moment, which allows its coupling to far electromagnetic field, related to enhancement of optical processes. Further, the dipole LSPR is the lowest energy LSPR, which makes it well spectrally distinguishable from the higher energy LSPR and thus convenient for our analysis. In conclusion, numerical simulations, together with EELS measurements, provide a robust and efficient platform for the interpretation of designed experiments, including quantitative characterization of accumulated charges and induced electric fields related to the lightning-rod effect.

3.3 Task 1: Charge Reservoir

In this section of the thesis we study the effect of the charge reservoir of a plasmonic antenna on the overall enhancement of the induced electric field in its vicinity. We used the spatially resolved EELS to study the electromagnetic response of plasmonic antennas and complemented the measured data with numerical simulations of the induced electric fields. The electric fields have been also evaluated for the case of interaction of plasmonic antennas with an electromagnetic plane wave.

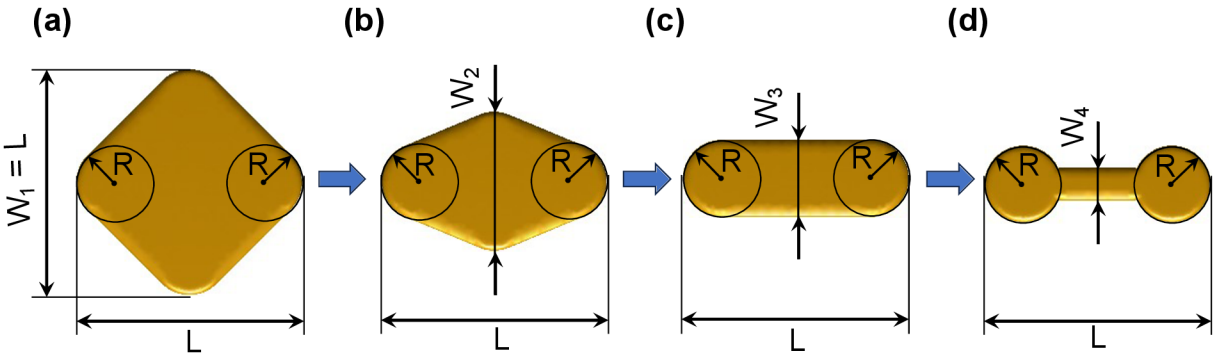

Figure 3.11: Schematic of the designed set of plasmonic antennas with indicated dimensions. The set consists of the following PA types: (a) Diamond, (b) tapered diamond, (c) rod, (d) dumbbell.

3.3.1 Design of Plasmonic Antennas

To investigate the effect of the charge reservoir on the total field enhancement of plasmonic antennas, we have designed a set of plasmonic antennas, depicted schematically in Fig. 3.11, where the reservoir is varied while the other parameters of PAs are as much unchanged as possible. The primary representative of this set is the diamond PA [Fig. 3.11(a)] with the largest volume and thus the largest charge reservoir of the set. The other PA types of the set, namely the tapered diamond PA [Fig. 3.11(b)], the rod PA [Fig. 3.11(c)], and the dumbbell PA [Fig. 3.11(d)], are obtained by gradually decreasing the width of the diamond PA. Individual PA types vary considerably in their volume and thus should provide a suitable platform for the study of the charge reservoir.

Each PA type is designed with identical curvatures at both ends (defined by the radius R of the inscribed circle). This ensures that the magnitude of the induced field is not influenced by the varied local curvature. To exclude the effect of surface wave localization, all of the PAs should support the dipole LSPR at the same energy. The resonant energy of the longitudinal dipole LSPR is primarily influenced by the PA's length. Consequently, the initial design choice was to set the length of the PAs constant.

The nominal dimensions of the PAs indicated in the diagram in Fig. 3.11 are as follows: antenna length $L = 300$ nm, radius of curvature $R = 50$ nm, antenna thickness $t = 30$ nm, and antenna widths $W_i = \{300, 200, 100, 40\}$ nm for $i = 1, 2, 3, 4$. These antenna dimensions have been used in numerical simulations.

For each considered PA type, a total of ten PAs have been produced. Three representatives of each type have been selected for EELS measurements. The dimensions of the fabricated PAs have been determined from the HAADF micrographs recorded during the EELS measurements. The thicknesses of the PAs were determined from EELS thickness profiles.

The dimensions of the fabricated antennas are listed in Table 3.1. The measured values of the PA widths and lengths are in all cases smaller than the nominal values, which is a typical fabrication inaccuracy of the FIB method (mainly associated with the Gaussian ion beam profile). The antenna lengths are approximately 30 nm shorter than the nominal values but they are very similar for all PA types. The measured curvature values are in good agreement with the nominal value and do not differ by more than

Table 3.1: The measured dimensions of the fabricated PAs of individual types. The nominal dimensions are as follows: 300 nm for length, 50 nm for local curvature, and 30 nm for the PA thickness.

PA type	Nominal width (nm)	Measured width (nm)	Measured length (nm)	Measured curvature (nm)	Measured thickness (nm)
1	300	285 ± 12	276 ± 8	53 ± 4	41 ± 1
2	200	197 ± 9	270 ± 3	47 ± 7	39 ± 1
3	100	95 ± 4	267 ± 5	44 ± 5	38 ± 2
4	40	32 ± 6	269 ± 9	44 ± 6	33 ± 4

10 nm for individual PA types. Therefore, we do not expect a significant effect of the local curvature on the experimental data retrieved from EELS measurements. Representatives of individual PA types are shown in the left panel of Fig. 3.14. The average thicknesses of most PA types are very similar, with an approximate value of 40 nm. The lower value for the dumbbell-type PA is due to a significant decrease in thickness in the narrow PA regions.

3.3.2 Electron Energy Loss Spectroscopy

EELS measurements and numerical simulations have been performed for all four PA types. The loss probability spectra are compared in Fig. 3.12. All spectra feature two distinct peaks corresponding to the dipole LSPR (lower energies) and the quadrupole LSPR (higher energies), which have been identified in Section 3.2.4 for the case of dia-

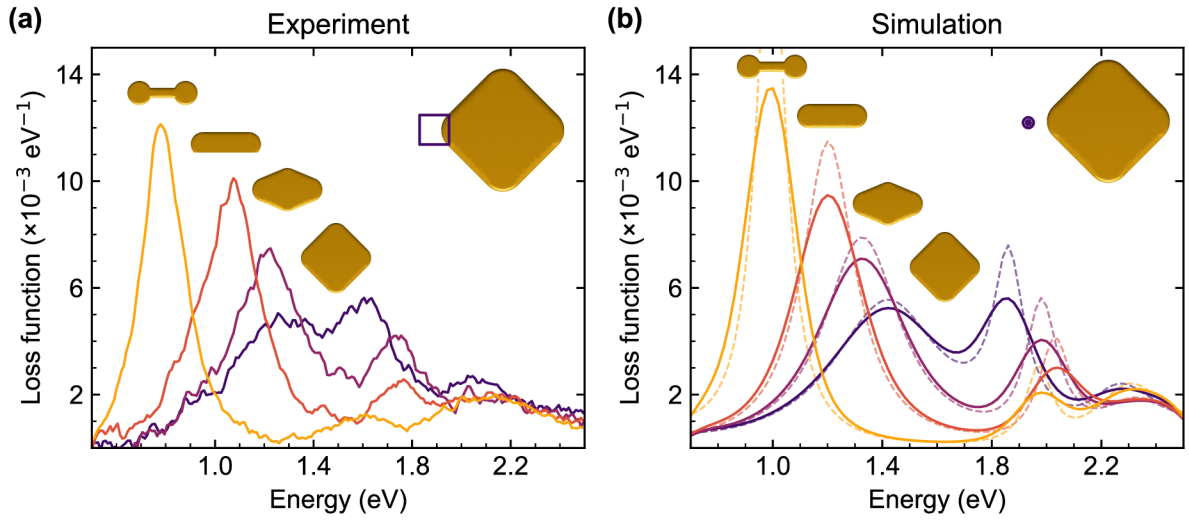

Figure 3.12: (a) Measured and (b) calculated EEL spectra of individual PA types. The spectra are complemented by the corresponding PA model. The square in the inset of the panel (a) indicates the ROI across which the spectrum was spatially averaged. The spot in the inset of panel (b) indicates the position of the electron beam utilized in the simulations. The calculated spectra (dashed lines) are convolved with a Gaussian with FWHM of 0.15 eV (solid lines).

mond PA. The spectral profiles show good qualitative agreement between the experiment [Fig. 3.12(a)] and the numerical simulations [Fig. 3.12(b)].

The dipole LSPR peaks have been fitted with Lorentzian functions (as described in Section 3.2.3), and the retrieved fit parameters have been used to determine the LSPR energies [Fig. 3.13(a)], the maximum peak intensities (amplitudes) [Fig. 3.13(b)], and the quality (Q) factors [Fig. 3.13(c)]. Measurements have been performed on several representatives of each type of PA, so the fit values here correspond to the determined mean values. These quantities are plotted against the true antenna width, that is, the nominal width for numerical simulations and the measured widths for the experiment (taken from Table 3.1). The error bars represent standard errors of the displayed quantities. The calculated spectra have been convolved with a Gaussian of FWHM 0.15 eV prior to peak fitting.

We will first address the energies of the dipole LSPR depicted in Fig. 3.13(a). As the antenna width decreases, a systematic red shift in the dipole LSPR energy is observed for both the experiment and the simulations. For all PA types, the experimental energies show a red shift relative to the simulations. In the case of wider PA types (ranging between 300 nm and 100 nm), the observed red shift is approximately 0.15 eV, which is mainly due to the fact that the membrane is not taken into account in the simulations. The thinnest dumbbell-type PA has a red shift of 0.3 eV compared to the simulated values. The exact cause of this significant difference remains unknown, but it may stem from the variance between the nominal and true dimensions of the fabricated dumbbell-type PAs (see Table 3.1).

The amplitudes of the dipole LSPR are depicted in [Fig. 3.13(b)]. Here, a strong quantitative correlation is observed between the experimental results and the simulations. Interestingly, the diamond PA shows the lowest amplitude of the PA set, slightly below 5×10^{-3} eV^{-1}. A consistent increase in the dipole LSPR amplitude is observed with the gradual narrowing of the antenna width. In the case of dumbbell PA, the LSPR amplitude reaches a value of 12×10^{-3} eV^{-1}, which is more than twice the amplitude recorded for diamond PA.

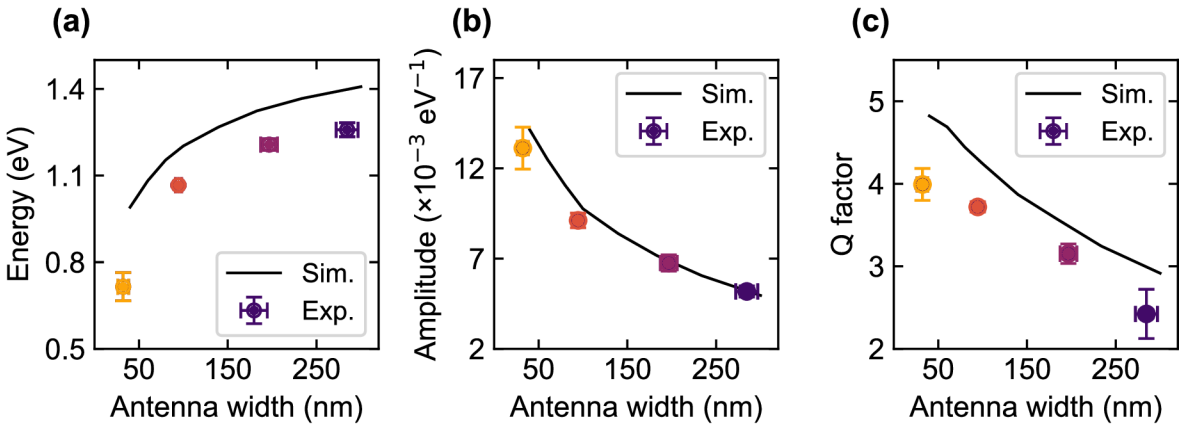

Figure 3.13: (a) Resonance energies, (b) amplitudes, and (c) Q factors of the dipole LSPR of individual PA types. The values obtained from the simulations are represented by a black curve and correspond to a total of eight types of PAs of different widths.

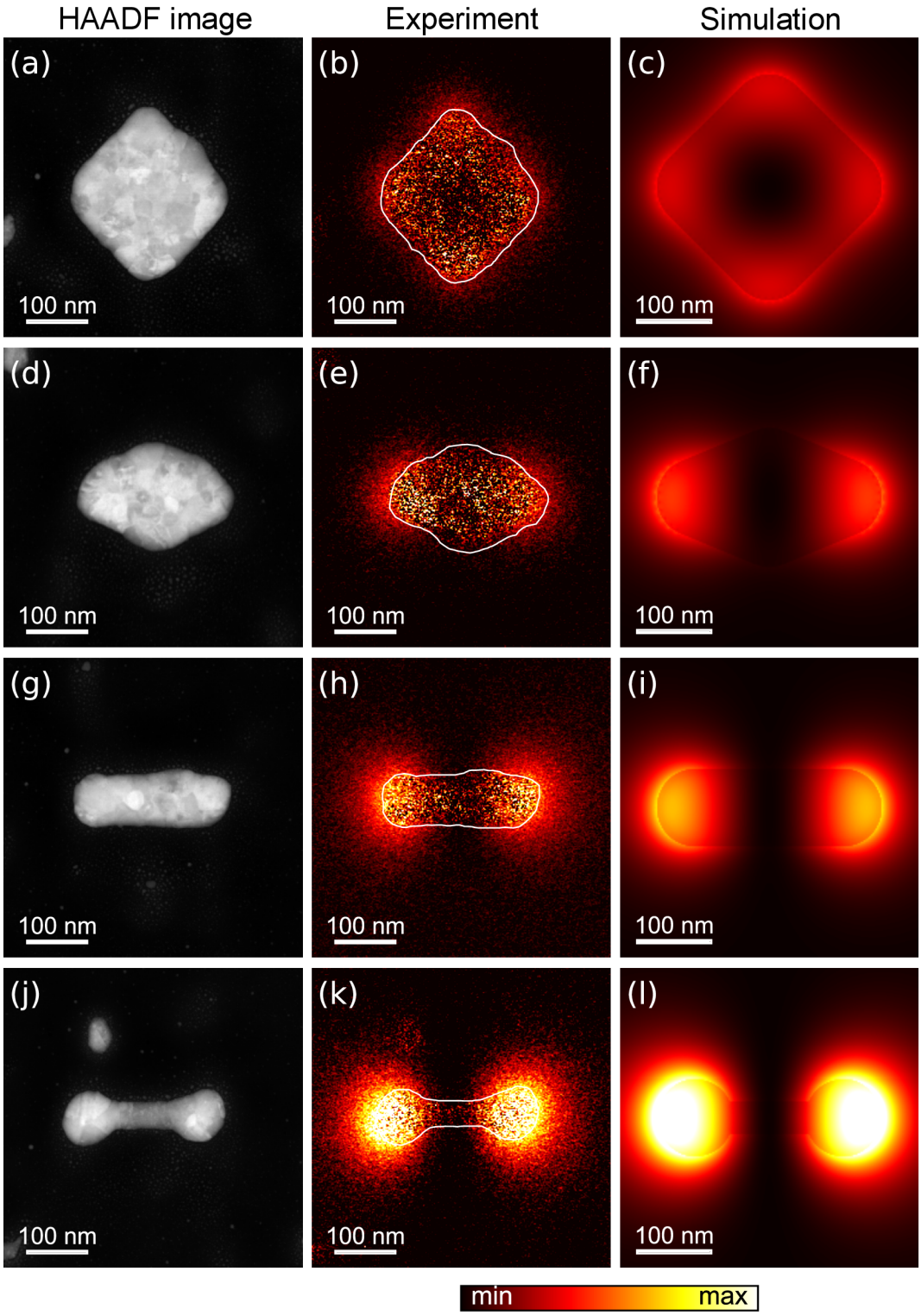

Figure 3.14: EEL maps of the dipole LSPR for the diamond PA (a–c) , the tapered diamond PA (d–f) , the rod PA (g–i), and the dumbbell PA (j–l). The HAADF micrographs of the studied PAs are shown in the left panels, the experimental EEL maps in the middle panels, and the calculated EEL maps in the right panels.

Q factors provide a good measure for comparing the performance of individual PA types in applications. Their values are often related to the field enhancement and other important characteristics of plasmonic fields [4]. The Q factors, defined as the resonance energy divided by the FWHM of the LSPR peak, are shown in Fig. 3.13(c) for the studied PA set. In this case, we also observe a good qualitative agreement between the experiment and the simulation. The experimental Q factors exhibit slightly lower values compared to the simulations, and this can be attributed to both their lower resonance energies and broader LSPR peaks. The lowest Q factor is observed for the diamond PA with a value of 2.4. The Q factor increases with decreasing antenna width and the highest experimental value of 4.0 is obtained for the dumbbell PA.

The results suggest that the charge reservoir effect does not seem to affect the set of examined PAs in the expected way. The highest amplitudes of the loss probability and also the highest Q factors have been observed for the case of the dumbbell PA, which should represent the smallest charge reservoir of the set. The results of the analysis in the spectral domain are also confirmed by the spatial distributions of the dipole LSPR loss probabilities shown in Fig. 3.14. The experimental EEL maps (displayed in the middle panel) exhibit a clear qualitative similarity to the calculated EEL maps (shown in the right panel). In the transition from diamond-type PA to dumbbell-type PA related to the decrease of the charge reservoir, we observe a significant increase in the loss probabilities at the antenna ends.

3.3.3 Induced Electric Field

EELS proves to be a prominent technique for mapping the near-fields of the LSPRs. However, it should be noted that this technique is only sensitive to the out-of-plane component (parallel to the electron beam) of the induced electric field. Therefore, in the following section, we complement the EELS results with calculations of the total magnitudes of the induced electric fields using numerical simulations. Numerical simulations were performed on eight different PA types, varying in width. This included the previously analyzed PA set, as well as other PAs that have intermediate widths.

The planar cross sections of the induced electric field calculated for the dipole LSPR are presented in Fig. 3.15 for the PA types studied in the previous section. The upper panels display the field distributions in the plane of the PA (the $xy-$plane), while the lower panels show the field distributions in the vertical plane passing through the center of the PA (the $xz-$plane). The calculated field distributions exhibit an analogous behavior to that observed in the EEL maps presented in Fig. 3.14, i.e., stronger induced electric fields are formed for the cases of thinner PA types. This phenomenon can be observed more clearly in the linear cross sections depicted in Fig. 3.16(b).

The excitation of the dipole LSPR was performed using the electron beam positioned near the left corner of the PA (position of the electron beam indicated by the white dot in the $xy-$plane and its trajectory with the white dashed line in the $xz-$plane, respectively). As a result, a stronger induced electric field is observed on this side of the PAs. In order to minimize the influence of the electron beam on the quantification of the induced electric field, we performed the quantification at the opposite (right) corner of the PAs. We are mainly interested in the local field magnitude evaluated at a single point (20 nm from the PA edge, marked by the blue point in panels (a) and (e) of Fig. 3.15). We have also investigated the mean field magnitude averaged over a volume of a cube with an edge

length of 50 nm indicated by the green squares in Fig. 3.15(a,e). The obtained magnitudes of the induced electric field are presented in Fig. 3.16(a). It is notable that the local field magnitudes are highly similar to the mean field magnitudes (within 5 %). Consequently, they can be utilized to represent the near field strength of individual PAs with great accuracy. Furthermore, these dependencies are in a qualitative agreement with the loss function amplitudes presented in Fig. 3.13(b). The highest magnitudes of both the local and mean fields are observed for the dumbbell-type PA, which are more than twice the corresponding magnitudes for the diamond-type PA.

Next, we studied the linear cross sections of the induced electric fields shown in Fig. 3.16(b) (taken along the orange dashed lines in Fig. 3.15). The field profiles exhibit the expected qualitative behavior, as illustrated in Fig. 3.15. The maximum field values are observed at the PA edges, where they decrease sharply in the surrounding dielectric environment. Within the PA, the field is nearly absent. For antennas of a smaller thickness, we observe the expected increase in the strength of the electric fields, which are also more localized (with larger slopes of the field profiles). In order to gain a deeper understanding of the characteristics of the field profiles, it is beneficial to attempt to fit them with appropriate curves. In this context, we present a phenomenological model in the form

$$E(x) = \frac{Q_{\text{eff}}}{(r_{\text{eff}} + x)^d} \exp(-\beta x). \tag{3.1}$$

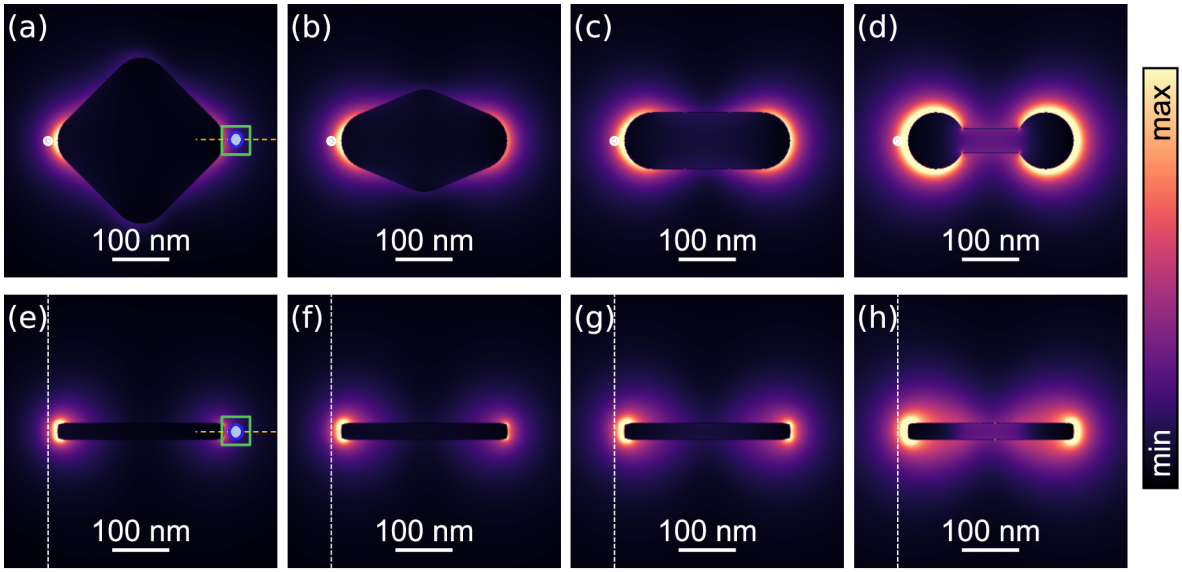

Figure 3.15: Calculated planar cross sections of the induced electric fields for individual PA types. (a–d) Field distributions in the PA (xy) plane. (e–f) Field distributions in the vertical (xz) plane crossing the longitudinal axis of the antenna. The electron beam position is indicated in the top panels (white dot), and its trajectory in the $xz-$plane in the bottom panels (white dashed line). Orange dashed lines indicate the positions of linear cross sections shown in Fig. 3.16(b). The blue dots and green squares indicate the position or area where we obtained the local and mean field magnitudes shown in Fig. 3.16(a).

The first term of the model is based on empirical relationships (well known from electrostatics) related to electric fields near charged particles. Here, Q_{eff} denotes the effective charge located at a distance r_{eff} (effective PA curvature) from the edge of the PA [see schematic in Fig. 3.16(c)]. The parameter d represents the dimensionality exponent, which should based on its value represent the nature of the effective charge, that is, point charge for $d = 2$ and linear charge for $d = 1$. The second term represents the evanescent field confinement given by the β parameter, which represents the nature of plasmonic fields. All of the introduced quantities are free fit parameters of the model.

The field profile fits using the introduced phenomenological model are found to be highly accurate within the considered interval, extending from 20 nm to 150 nm from the edge of the PA. The maximum estimated error did not exceed 0.1 %. The resulting fit parameters of the field profiles are presented in Table 3.2 for each considered PA type. The following observations can be made: (1) The values of the effective charge increase rapidly as the width of the PA decreases. The effective charge of the dumbbell-type PA

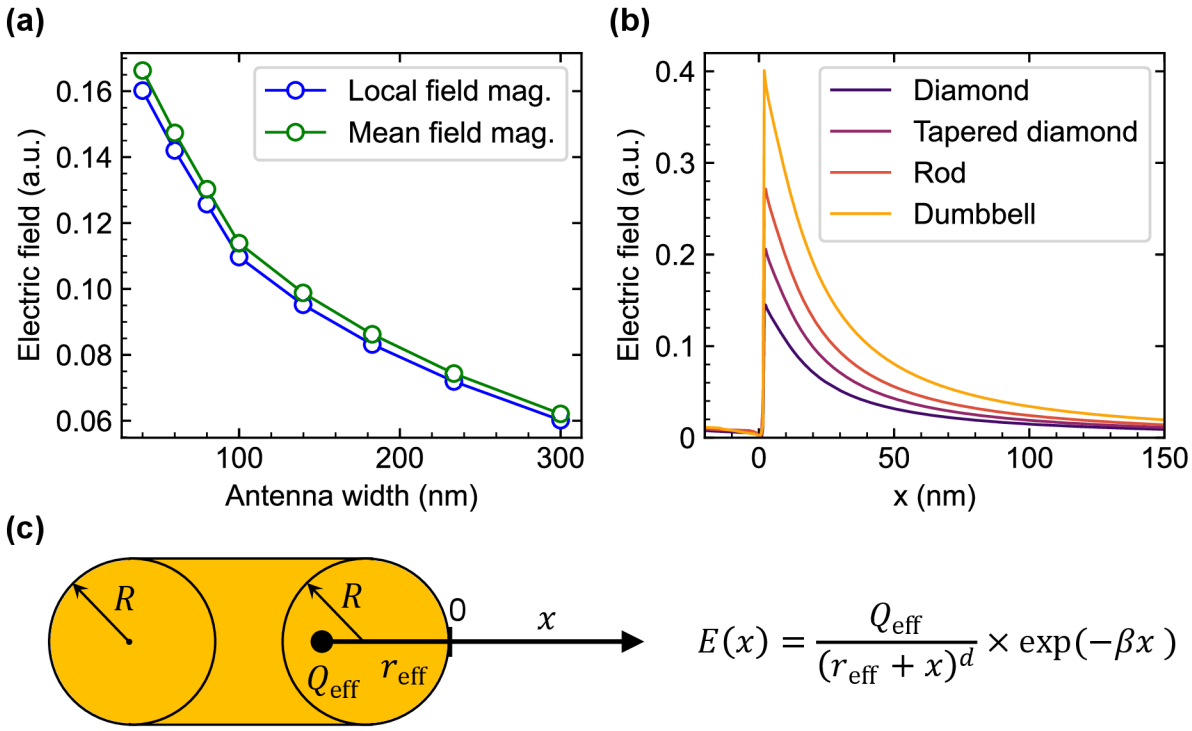

Figure 3.16: (a) The local (blue line) and mean (green line) electric field magnitudes taken from areas indicated in Fig. 3.15. The symbols correspond to the actual calculated values for individual PA types (indicated by the antenna width, where 300 nm corresponds to the diamond and 40 nm corresponds to the dumbbell), lines are guides to the eye. (b) Linear cross sections of the induced electric field from Fig. 3.15. The $x-$axis denotes the distance from the edge of the PA in correspondence to the schematic in (c). (c) Schematic defining the parameters of the phenomenological model (equation on the right) for the fit of the linear cross sections of the induced electric field in (b). The effective charge Q_{eff} is located at a distance r_{eff} (effective curvature) from the edge of the PA. The dimensionality exponent d resembles the nature of the effective charge (2: point charge, 1: linear charge). β represents the contribution of the evanescent confinement.

reaches a value that is more than ten times higher than that of the diamond PA. (2) The dimensionality exponent d is found between the values 1.31 and 1.63, This indicates a shift from a relatively linear charge distribution (wider PAs) to a more concentrated, point-like one (narrow PAs). (3) The effective curvatures seem to be rather constant for most PAs. The exception to this trend are the two widest PAs, which exhibited a 20 % reduction in the values. (4) The evanescent confinement parameter β has been found to deviate from its originally anticipated function. The values fluctuate randomly and their magnitudes are very small. With this in mind, we also performed the fits of the induced fields with β set to zero, thus neglecting the exponential component of the model. The parameters of the fit with this simplified model are presented in the lower section of Table 3.2. The parameters exhibit qualitative similarities to those observed in the previous case.

Table 3.2: Parameters of the phenomenological model obtained from the fits of the linear cross sections of individual PA types (represented by their widths). The upper part of the table presents the parameters of the fit when considering the complete model given by Eq. (3.1). The lower part of the table presents its simplified version neglecting the exponential term by setting $\beta = 0$.

Phenomenological model								
Width (nm)	300	250	200	150	100	80	60	40
Q_{eff}	8	13	32	39	52	60	72	90
d	1.31	1.39	1.55	1.57	1.60	1.60	1.61	1.63
r_{eff}	16	17	21	22	22	22	22	23
β	0.0004	0.0004	-0.0003	-0.0001	-0.0001	0	0.0001	0.0001
Phenomenological model ($\beta = 0$)								
Q_{eff}	10	17	27	36	48	61	77	100
d	1.38	1.45	1.51	1.55	1.58	1.60	1.63	1.66
r_{eff}	17	18	20	21	22	22	23	24

3.3.4 Discussion

The primary objective of the proposed set of plasmonic antennas was to investigate the charge reservoir effect in isolation from other phenomena that contribute to the total field enhancement. By selecting the same curvatures at the PA terminations, the influence of local curvature was negated. However, selecting the same lengths of the antennas did not guarantee exactly the same resonance energies observed in the dipole LSPR, and thus the impact of surface wave localization could not be fully excluded. In this section, we will address this effect by tuning the dipole resonance energies to the same value for the whole PA set. In doing so, the effect of the charge reservoir on the field enhancement should be isolated.

The dipole resonance energies of individual PAs can be tuned by modifying their lengths. The resonance energy of 1.2 eV was found to be achievable for all PA types with reasonable length adjustments. To achieve this energy, the lengths of the individual PA

types were changed from the nominal value of 300 nm to the following: 385 nm for the diamond, 350 nm for the tapered diamond, 300 nm for the rod, and 235 nm for the dumbbell. Note that the widths of the diamond PA and the tapered diamond PA were adjusted accordingly to preserve their shapes (dimension ratios). The widths of the thinner PAs (rod and dumbbell types) remained unchanged. This resulted in the creation of even more significant differences in the charge reservoirs.

The calculated EEL spectra of tuned PAs are shown in Fig. 3.17(a). Note that the spectra were convolved with a Gaussian of FWHM 0.15 eV, facilitating their comparison with the previous cases. Once more, it is observed that the amplitudes of the dipole LSPRs are higher for antennas with smaller charge reservoirs.

Thus far, the observed behavior of the charge reservoir has been precisely the opposite of what was anticipated. One potential explanation for this phenomenon is the nature of the selected excitation field. The electron beam represents a localized excitation that does not exploit a full volume of the PA – the interaction volume is restricted by the extension of the field of the electron beam and does not vary significantly for the examined antenna. To exclude this effect, we shall now examine the induced electric fields of the dipole LSPR excited by a plane electromagnetic wave, which represents a planar excitation that affects charges throughout the entire volume of the PA.

All calculations were performed using the MNPBEM toolbox. The same antenna dimensions and discretizations were used as in the EELS simulations, only the excitation was changed. Scattering and absorption cross sections were calculated for all considered PA types. The scattering cross sections C_{scat} correspond to the ratio of the total power scattered by the antenna and the intensity of the incident plane wave, that is, $C_{\mathrm{scat}} = P_{\mathrm{scat}}/I_0$. Similarly, the absorption cross section is calculated as the total absorbed power by the antenna normalized to the intensity of the plane wave: $C_{\mathrm{abs}} = P_{\mathrm{abs}}/I_0$. The extinction can be expressed as their sum, thus $C_{\mathrm{ext}} = C_{\mathrm{scat}} + C_{\mathrm{abs}}$. The calculated scattering and absorption cross sections for the PA set are shown in Fig. 3.17(b,c).

Both spectra feature a single peak corresponding to the dipole LSPR. In the case of scattering [Fig. 3.17(b)] we observe a slight blue shift in the energy of the peak with

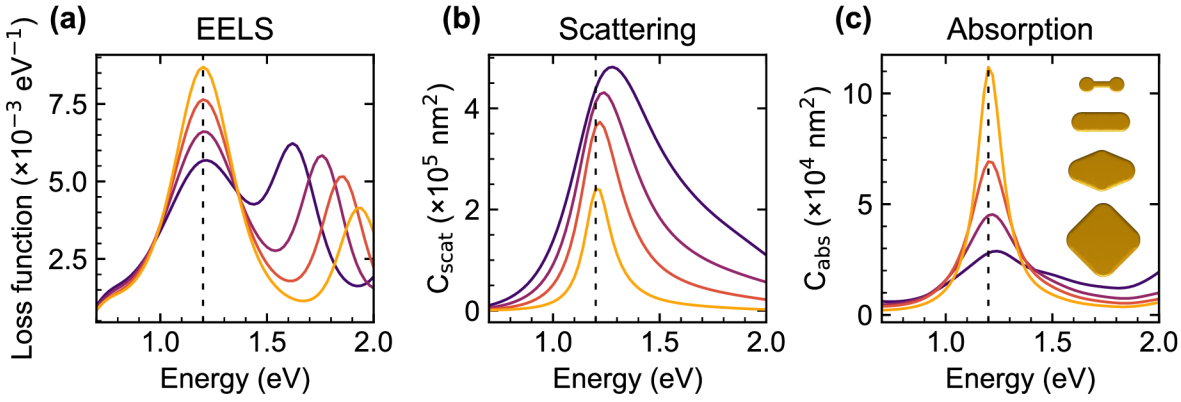

Figure 3.17: Tuning the resonance energies of the dipole LSPR to 1.2 eV (black dashed line) in (a) EEL spectra, (b) scattering cross section, and (c) absorption cross section. Individual PA types with adjusted dimensions are shown in (c) to facilitate their size comparison.

increasing antenna width. The target energy 1.2 eV (black dashed line) is reached for the dumbbell PA, while the diamond PA is at the energy 1.3 eV. However, in the case of the absorption cross section [Fig. 3.17(b)], the peak energies correspond very well to the target energy for all PA types. The origin of the blue shift is not further investigated in this thesis. All PA types are predominantly scattering. Higher scattering cross sections are observed for the larger PAs, which may therefore suffer stronger radiative losses. The high absorption observed for narrow PAs might stem from increased ohmic absorption as a result of the high currents in the narrow cross sections of these PAs.

Induced electric fields were calculated at the target energy 1.2 eV. Similarly to the electron beam excitation, the local and mean electric field magnitudes were evaluated in areas indicated in Fig. 3.15(a,e). We will now discuss their comparison with previous results for electron beam excitations. To enable this comparison, we normalize the values of each presented quantity against the value of the same quantity for the diamond type PA. This gives us the enhancement factor for each quantity related to the studied effect of the charge reservoir (studied PA sets). These enhancement factors are shown in Fig. 3.18 for the case of the PA set with constant lengths [Fig. 3.18(a)] and also for the case of the PA set with constant resonance energies [Fig. 3.18(b)].

For all of the presented quantities, we observe an increase in the enhancement factors with decreasing PA charge reservoirs (PA widths), thus, the opposite behavior to the originally expected. In the case of the PA set with constant lengths [Fig. 3.18(a)], we can see good quantitative agreement between the experimental (light blue line) and calculated (dark blue line) loss function enhancement factors. Furthermore, the corresponding enhancement factors of the calculated induced electric fields (red curve) lie in between these dependencies. All three quantities do not differ by more than 10 %. The difference is larger (around 30 %) in the case of PAs with constant energies in Fig. 3.18(b). Nevertheless, we see that EELS represents a suitable technique for experimental comparison of the induced field magnitudes of individual antennas.

By changing the type of excitation from the electron beam (localized) to the electromagnetic plane wave (planar), the enhancement factors related to the induced electric fields seem to decrease quite significantly. In the case of the constant-length PA set, the enhancement factor decreases from the value of 2.8 for the electron beam to 1.9 for the plane wave. In the case of the constant-energy PA set, the enhancement factor decreases from the value of 3.1 for the electron beam to 1.6 for the plane wave, thus almost by 50 %. Because the electromagnetic plane wave affects the charges of the entire PA volume, this phenomenon could be partially related to the charge reservoir. However, even in the case of the plane wave, the effect of the charge reservoir shows an inverse behavior.

We propose several possible explanations for the inversed effect of the charge reservoir: (1) The larger volume of the antenna might result in stronger radiative losses, thus suppressing the Q factor and the amplitude of the dipole LSPR. This factor is supported by the amplitudes of the quadrupole LPSR, which shall not be influenced by the radiative losses (since the quadrupole mode is dark and does not couple to the far field). The amplitudes of the quadrupole LSPR are ordered in the opposite way, decreasing with a decreasing reservoir. (2) The idea of the charge reservoir is based on a classical view of free electrons driven by external excitation. However, LSP are quantized, and we observe only single LSP processes. The energy of the LSP is contributed by the energy stored in the induced electric field. For larger PAs, this field is distributed over the larger volume,

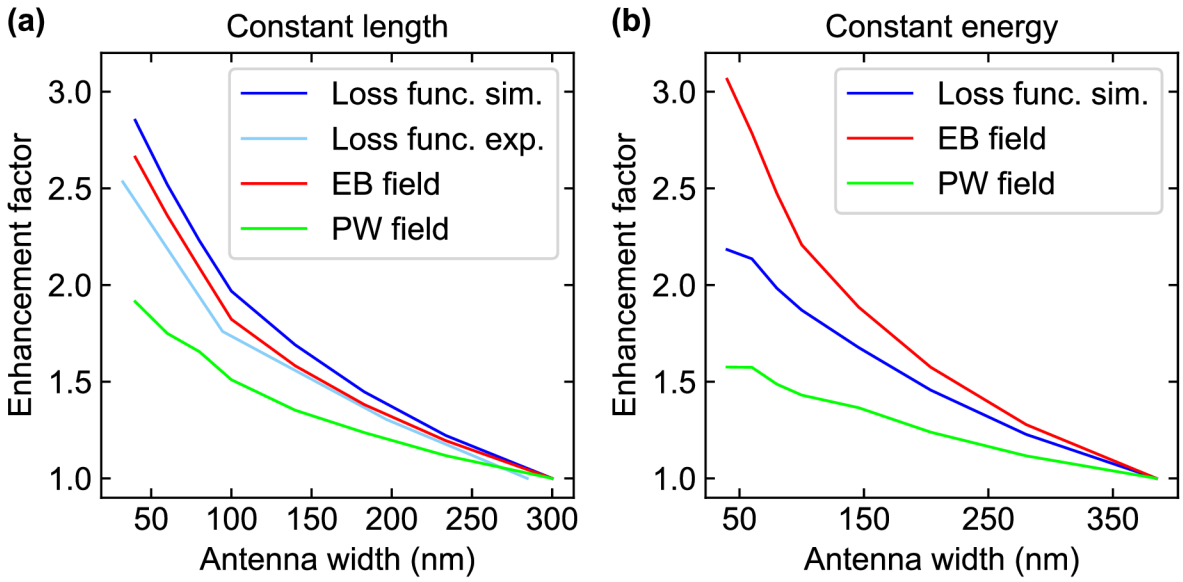

Figure 3.18: Enhancement factors for the PA set with constant length (a) and for the PA set with constant dipole LSP resonance energies (b). The enhancement factors were determined by normalizing the values of individual quantities against the value of the same quantity obtained for the diamond type PA. The included induced electric fields correspond to the local field magnitudes taken from areas indicated in Fig. 3.15, for the case of electron beam (EB) excitation and the plane wave (PW) excitation.

and its magnitude shall be reduced. The detailed analysis of these effects is beyond the scope of this thesis.

3.4 Task 2: Local Curvature

This section of the thesis examines the impact of the local curvature of a plasmonic antenna on the overall induced electric field in its vicinity. This phenomenon is studied only on the basis of numerical simulations. The procedure to be used will be analogous to that applied in the case of the charge reservoir.

3.4.1 Design of Plasmonic Antennas

In this section, we will study a set of plasmonic antennas shown in Fig. 3.19. The first antenna in this set is a disc with a radius of curvature $R_1 = 150$ nm [Fig. 3.19(a)]. The other antennas in the set are squares with rounded corners, each having unique curvature radii [Fig. 3.19(b–d)]. These radii correspond to the circles inscribed at the PA corners and are set to $R_i = \{125, 100, 75, 50, 25, 10\}$ nm, for $i = 2, 3, \ldots, 7$. The dimensions of these PAs are kept at 300 nm for both length L and width W, corresponding to the diameter of the disc. This configuration should ensure that all PAs in the set support the dipole LSPR at similar energies while also maintaining comparable charge reservoirs. Consequently, this PA set provides a suitable platform for studying the effect of local curvature on the induced electric field in isolation from other considered contributions. In addition, the identical diamond antenna is included in both this set [Fig. 3.19(c)] and the

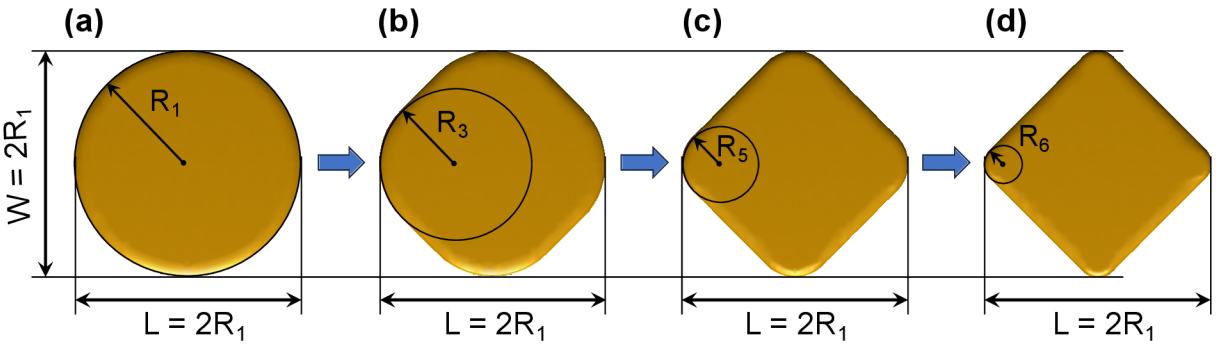

Figure 3.19: Schematic of the designed set of plasmonic antennas with indicated dimensions including the disc shaped PA with the lowest curvature of the set (a), and a series of diamond PAs with rounded corners of different curvatures given by the inscribed circles at the corners (b–d).

set related to the charge reservoir [Fig. 3.19(a)], which facilitates a direct comparability of both effects.

3.4.2 Electron Energy Loss Spectroscopy

The EEL spectra have been calculated for all the considered PA types. The electron beam was perpendicular to the plane of the PA and positioned 20 nm away from the corner of the diamond (or disc). Although the experiment is not included in this case, we have convolved the EEL spectra with a Gaussian of FWHM 0.15 eV to facilitate comparison with the results obtained in the study of the charge reservoir effect. The convolved EEL spectra for several PA representatives of different local curvatures are shown in Fig. 3.20(a). Similarly to the previous cases, the spectra feature two distinct peaks corresponding to the dipole LSPR (lower energies) and the quadrupole LSPR (higher energies). As the radius of curvature (values in the legend) decreases, the amplitudes of both peaks increase. Furthermore, the energies of the dipole LSPR blue shift, while the opposite is true for the quadrupole LSPR. This results in a stronger overlap of these LSPRs for the case of PAs with high curvatures.

After the convolution, we performed the sequential fitting of individual LSPR peaks with Lorentzian functions. The fitted values for the dipole LSPR energies are depicted in Fig. 3.20(b), the peak amplitudes are illustrated in Fig. 3.20(c), and the Q factors are presented in Fig. 3.20(d). As the local curvature of the PA increases (curvature radius decreases), we observe a systematic blue shift in the resonance energies within 0.12 eV [Fig. 3.20(b)]. The relationship between peak amplitudes and the local curvature of the PA [Fig. 3.20(c)] appears to be less straightforward. The disc (R = 150 nm) shows the smallest value of the amplitude of 4.55×10^{-3} eV^{-1}. With increasing local curvature, the peak amplitudes systematically increase until a value 4.9×10^{-3} eV^{-1} is reached for the PA with the radius of curvature equal to 50 nm. This behavior was anticipated as a consequence of the increased local curvature of the PA, thus a manifestation of the PLRE. However, when the local curvature of the PA is further increased, a rapid decrease in the peak amplitudes is observed. This behavior may seem counterintuitive at first, but it is

important to remember that these peak amplitudes correspond to only one beam position [indicated in the inset in Fig. 3.20(a)].

In order to better describe the behavior of the near fields around these antennas of different curvatures, we calculated the spatial distributions of the loss probabilities at the energy of the dipole LSPR, which are shown in Fig. 3.21(e–h). In the case of the disc, we qualitatively observe the lowest loss probabilities of the PA set [Fig. 3.21(e)]. The spatial distribution of the loss probability is concentrated mainly at the edge of the disc and preserves its radial symmetry. When PA curvatures increase, the loss probabilities increase systematically in magnitude and become strongly localized at the corners of the PAs. Thus, the decrease in the peak amplitudes observed in Fig. 3.20(c) is likely to be related to a strong confinement of the induced electric fields at the sharp corners of these PAs. Consequently, the magnitudes of these induced electric fields are weaker at the position of the electron beam, which also leads to weaker peak amplitudes. We will further address this effect in the following section.

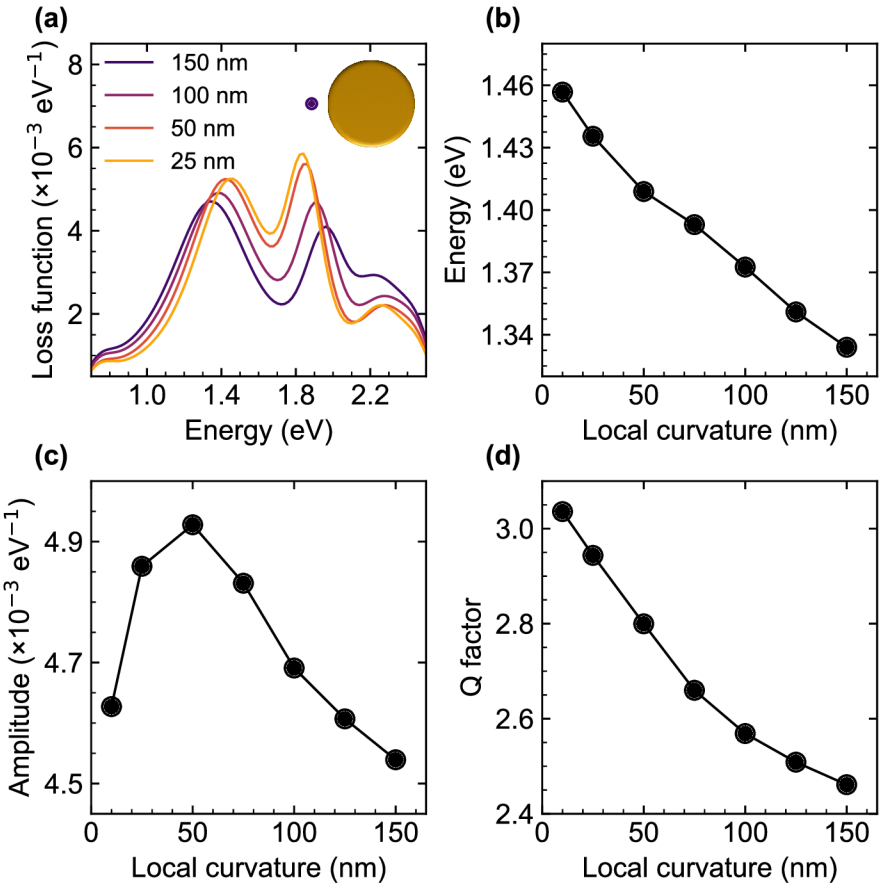

Figure 3.20: (a) Calculated EEL spectra convolved with a Gaussian of FWHM 0.15 eV of individual PA types with different curvatures. The curvature radii correspond to the values in the legend. The dot in the inset shows the position of the electron beam used in the simulations. The dipole LSPR energies (b), peak amplitudes (c), and Q factors (d) obtained from the fit parameters of the corresponding peaks. The calculated values are indicated by black circles. The lines are guides to the eye.

Finally, we observe a systematic increase in the Q factors with the increasing local curvature of the PA [Fig. 3.20(d)], which is related to the decrease in the FWHM of the dipole LSPR peaks and also to the increase in the resonance energies.

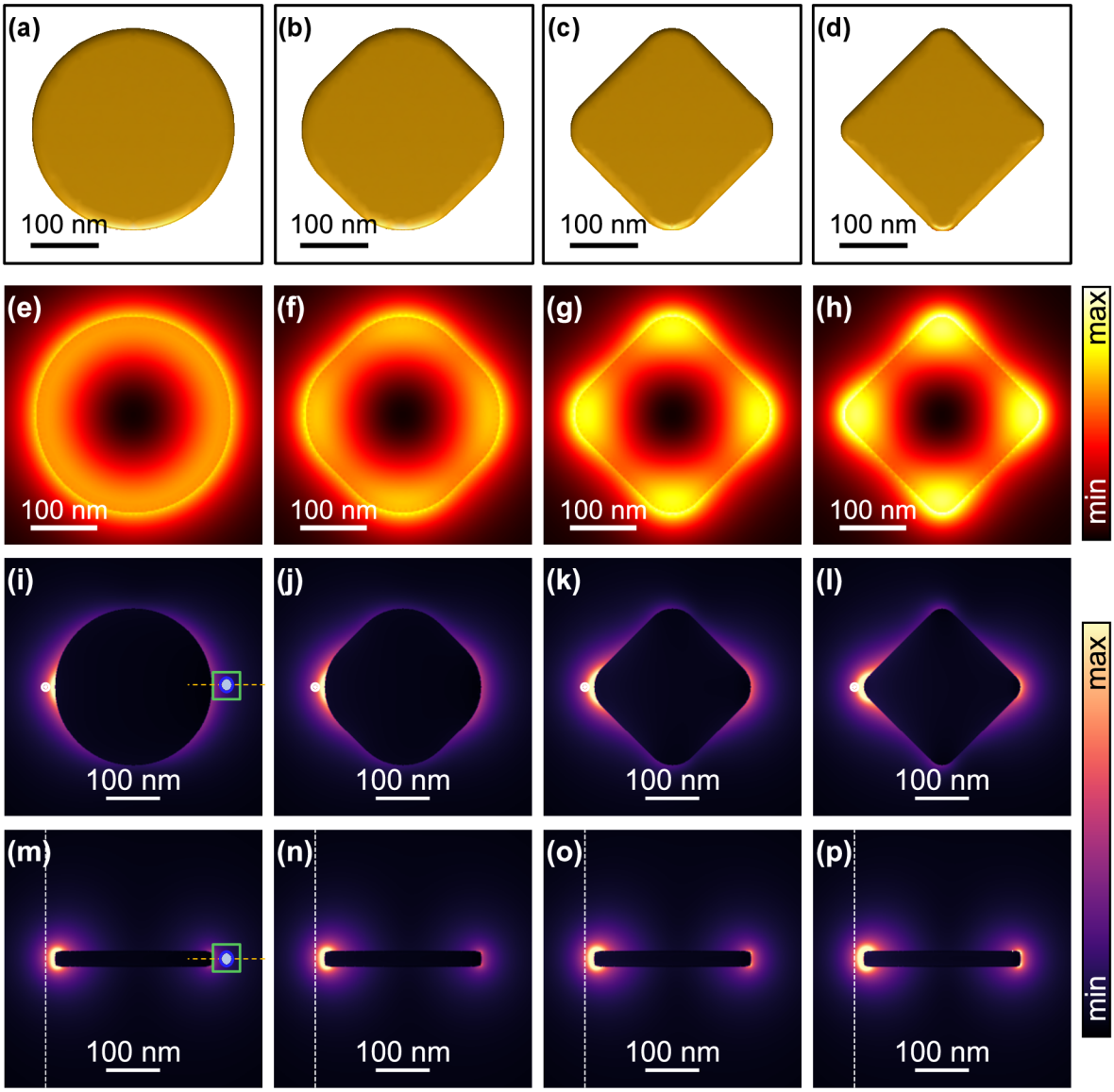

Figure 3.21: The mapping of the dipole LSPR near fields for the studied PA set. (a–d) Schematics of the studied PAs. (e–h) Calculated EEL maps at the energy of the dipole LPSR. (i–l) Calculated planar cross sections of the induced electric field in the central plane of the PA. (m–p) Calculated planar cross sections of the induced electric field in the vertical (xz) plane crossing the longitudinal axis of the antenna. The electron beam position is indicated in the top panels (white dot), and its trajectory in the xz—plane in the bottom panels (white dashed line). The blue dots and green squares in panels (i,m) indicate the position or area where we obtained the local and mean field magnitudes shown in Fig. 3.22(a). Orange dashed lines indicate the positions of linear cross sections shown in Fig. 3.22(b).

3.4.3 Induced Electric Field

First, we computed the planar cross sections of the induced electric field at the dipole LSPR energy. The resulting field distributions in the PA plane (intersecting the PA in the middle) are illustrated in Fig. 3.21(i–l), and the field distributions in the vertical plane intersecting the longitudinal axis of the antenna are depicted in Fig. 3.21(m–p). The following observations can be made: (1) For the disc-shaped PA [Fig. 3.21(i,m)], the induced electric field is the least confined, spreading across its surface well beyond the longitudinal axis of the PA and exhibiting noticeably lower field magnitudes. (2) As the local curvature of the PAs increases, the field gradually intensifies in magnitude and becomes more concentrated at the sharp corners. This phenomenon can be seen as a clear demonstration of the PLRE. (3) The fields are significantly more concentrated at their left corners in comparison to the right corners, i.e., near the location of the electron beam excitation (indicated by the white dot in the xy-plane and its trajectory with the white dashed line in the xz-plane).

We will now examine the local and mean field magnitudes from the areas indicated in Fig. 3.21(i,m). The corresponding values for each PA type are shown in Fig. 3.22(a). Once again, the local field magnitudes correspond very well to the mean field magnitudes, with a difference of less than 5 %. A systematic increase in the electric field is observed with increasing local curvature of the PA corner. The highest magnitudes for both local and mean fields are found for the PA with the highest curvature (radius of curvature equal to 10 nm), and are approximately 1.5 times larger than the fields observed for the disc.

Next, we examine the linear cross sections of the induced electric field along the orange dashed lines depicted in Fig. 3.21(i,m). The obtained field profiles are shown in Fig. 3.22(b). As discussed, the smallest electric field magnitudes are observed for the disc. With increasing curvature of the PA, the magnitudes of the induced electric field also increase, especially near the edge of the PA where the field is highly localized. This strong localization is further evidenced by the rapid decrease in magnitude with increasing distance from the PA. Conversely, the field of the disc is less concentrated at the PA's edge and decreases rather gradually. As a result, the magnitudes of the electric field are nearly identical for all PAs at greater distances from the PA. It is important to note that this behavior of the field profiles is significantly different from that observed in the case of the charge reservoir effect [see Fig. 3.16(b)]. To demonstrate these differences, we will now fit the field profiles using the phenomenological model introduced in Section 3.3.3.

The field profiles were fitted with a very high accuracy. The maximum fitting errors are below 0.2 % for the complete phenomenological model. The resulting fit parameters of the field profiles are listed in Table 3.3. Let us begin by examining the full model presented in the upper part of the table. The values of the effective charge Q_{eff} gradually increase with increasing PA curvature. The dimensionality exponent d also increases gradually, but for all PAs corresponds to rather a linear charge character. The effective curvatures do not show a significant trend in the case of PAs with smaller curvatures, the values then drop by about 50 % for the cases of higher curvatures. The values of the evanescent confinement parameter β are rather small. Therefore, we will also employ the simplified phenomenological model which neglects the exponential term.

These fits were also very successful with maximum estimated errors below 2.5 %. The fit parameters are listed in the bottom part of Table 3.3. The values of the effective charge Q_{eff} are similar for all antennas in the set, with some decrease for the lowest values of the

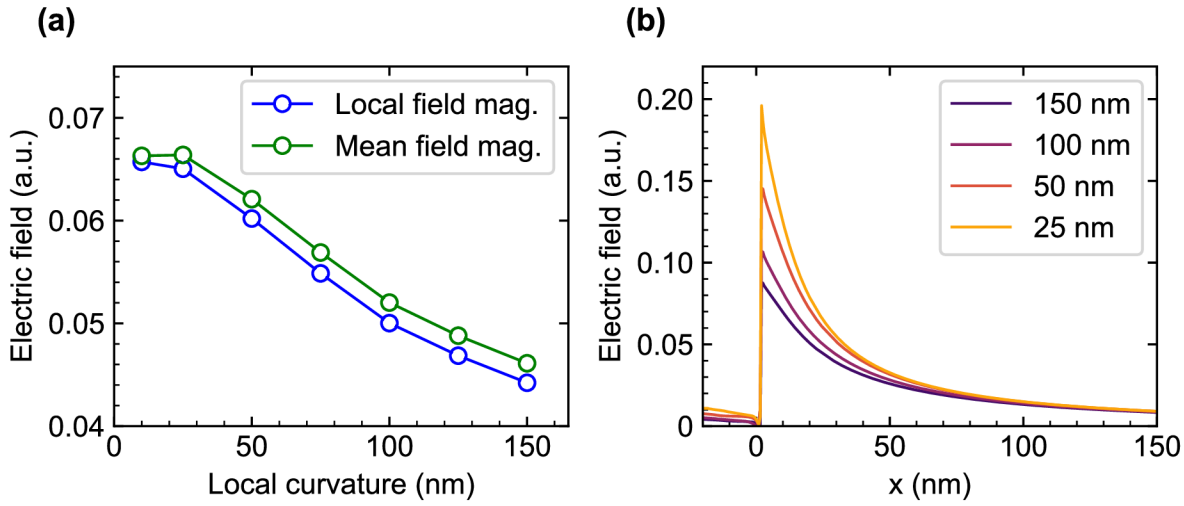

Figure 3.22: (a) Local (blue line) and mean (green line) electric field magnitudes taken from areas indicated in Fig. 3.21(i,m). The symbols correspond to the actual calculated values for individual PA types of different local curvatures, and the lines are guides to the eye. (b) Linear cross sections of the induced electric field taken along the orange line in Fig. 3.21(i,m). The x-axis denotes the distance from the edge of the PA in correspondence with the schematic of the phenomenological model in Fig. 3.16(c).

radius. The dimensionality exponent d is very similar for almost all considered PAs and maintains rather a linear charge character (values closer to 1). Finally, in this case, we observe a systematic decrease in the effective curvature values, which corresponds very well to the decreasing actual radius of curvature of the antennas. This parameter might be thus strongly related to the effect of the strong field localization near the sharp PA corners.

Table 3.3: Parameters of the phenomenological model obtained from the fits of the field profiles of individual PAs with different local curvatures (indicated by their radius of curvature). The upper section of the table shows the fit parameters for the full model described by Eq. (3.1). The bottom section displays a simplified version of the model, which neglects the exponential term by setting $\beta = 0$..

Phenomenological model							
Curvature (nm)	150	125	100	75	50	25	10
Q_{eff}	3	4	5	7	8	8	5
d	1.09	1.15	1.23	1.27	1.31	1.31	1.24
r_{eff}	18	19	19	18	15	15	10
β	0.0015	0.0012	0.0009	0.0007	0.0004	0.0004	0.0006
Phenomenological model ($\beta = 0$)							
Q_{eff}	10	11	11	11	10	8	6
d	1.37	1.38	1.39	1.39	1.38	1.33	1.29
r_{eff}	27	26	24	21	17	12	9

3.4.4 Discussion

The primary objective of the proposed set of plasmonic antennas was to investigate the effect of local curvature in isolation from other phenomena that contribute to the overall magnitude of the electric field. The proposed antennas have very similar dimensions, which should greatly limit the influence of the charge reservoir. By choosing the same length for all antennas in this set, the differences in the resonance energies for the different antenna types were significantly reduced, with a maximum difference of 0.12 eV. Consequently, the effect of surface wave localization should not differ significantly for this set of antennas. To completely exclude this effect, we modified the antenna dimensions so that they all exhibit a dipole LSPR at an energy of 1.2 eV. This value was selected in the same way as in Task 1.

To achieve this resonance energy, it was necessary to make the following adjustments to the antenna dimensions: The lengths and widths of individual PAs were changed from the nominal value of 300 nm to $L_i = W_i = \{350, 360, 370, 375, 385, 395, 405\}$ nm, for $i = 1, 2, \ldots, 7$. The radius of curvature was changed only for the case of the disc to preserve its shape.

The EEL spectra were calculated for both PA sets and the plane electromagnetic wave excitation was also considered for comparison with the previous case. The induced electric fields were then calculated and evaluated for both cases of excitations. We present the results of these calculations in the form of the enhancement factors, which were introduced in Section 3.3.4. In this case, we normalize the values of each presented quantity against the value of the same quantity obtained for the disc. The resulting enhancement factors

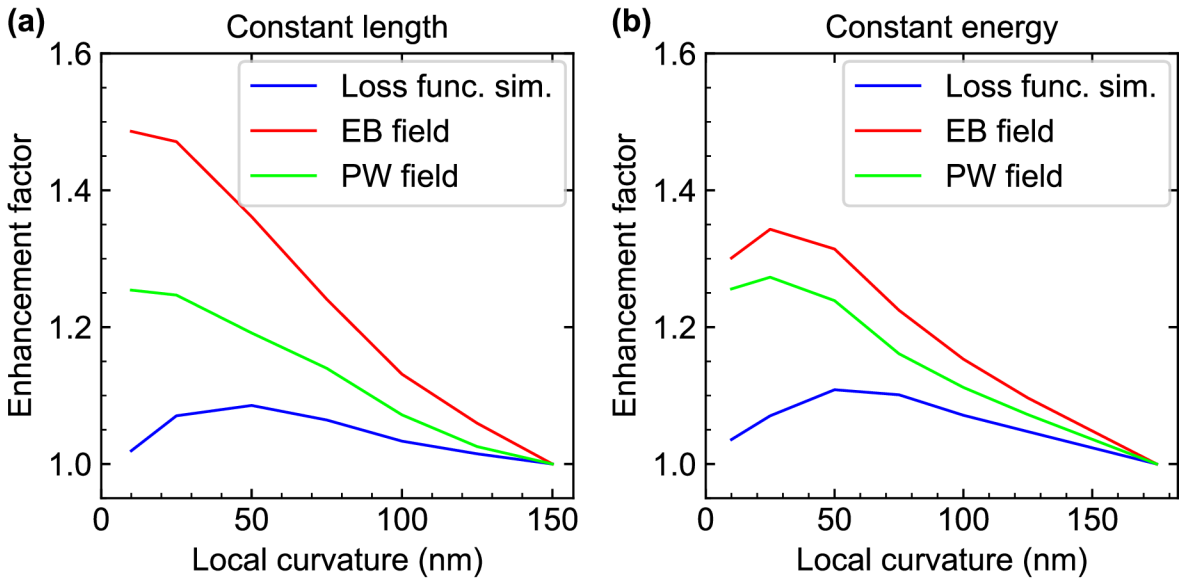

Figure 3.23: Enhancement factors for the PA set with constant lengths (a) and for the PA set with constant dipole LSP resonance energies (b). The enhancement factors were determined by normalizing the values of individual quantities against the value of the same quantity obtained for the disc type PA. The included induced electric fields correspond to the local field magnitudes taken from areas indicated in Fig. 3.21(i,m), for the case of electron beam (EB) excitation and the plane wave (PW) excitation.

are shown in Fig. 3.23 for the case of the PA set with constant lengths [Fig. 3.23(a)] and also for the case of the PA set with constant resonance energies [Fig. 3.23(b)].

All dependencies of the enhancement factors exhibit a qualitatively similar behavior. We observe a systematic increase in all enhancement factors with increasing curvature. The enhancement of the electric field of the antenna is thus clearly related to its curvature. Interestingly, in the case of antennas with the highest curvatures, we observe a slight decrease in the enhancement factors. This can be associated with strong field localization in the vicinity of these antennas. All quantities are evaluated at a distance 20 nm from the edge of the PA, where these strongly localized fields have smaller magnitudes than the more spread fields of PAs with smaller curvatures. The increase in field enhancement factors for both PA sets is less pronounced for the plane wave excitation.

Conclusions and Outlook

In this thesis, we have studied the plasmonic lightning-rod effect, which refers to correspondence between the local curvature of plasmonic antennas and local magnitude of the electric field of localized surface plasmons supported by those plasmonic antennas.

We performed a detailed qualitative analysis aiming at the identification of the individual effects that influence the local magnitude of the electric field induced in plasmonic antennas. Beside the local curvature, they include the charge reservoir and the evanescent nature of the plasmon field. Next, we attempted to isolate the contribution of these individual effects to the overall magnitude of the induced electric field. To this end, we designed sets of PAs where only one effect is intentionally varied and the others are kept as much unmodified as possible.

In the first case, we studied the effect of the charge reservoir on the magnitude of the induced electric field. The set consists of antennas with identical length (to ensure similar energies of plasmon resonances related with the surface confinement of plasmon field) and identical local curvature of the parts where the field was recorded (to exclude effects of varied local curvature). The width of the antennas was varied in order to vary the area (or volume) of PA which provides the reservoir of free electrons that shall affect the magnitude of the charge of plasmon resonances. We observed, somewhat surprisingly, that antennas with larger areas produce weaker fields. This effect was consistently observed for both the local excitation of plasmon resonances (using electron beam) and delocalized excitation using a plane wave. This effect is probably related with radiative losses, which are higher for larger antennas (evidence from a higher calculated scattering cross section).

In the second case, we studied the effect of the local curvature on the magnitude of the induced electric field. The set of the studied plasmonic antennas includes a disc and a number of square-shaped antennas with rounded corners of different curvatures. The lengths of the antennas were also set identical in this case, to ensure both similar energies of plasmon resonances and similar charge reservoirs. We observed a systematic increase in the magnitudes of the electric fields with an increasing local curvature (decreasing radius of curvature) of the antenna for both the electron beam and the plane wave excitations. Antennas with high local curvatures also exhibit strong field confinements in their vicinity.

Further research in this area may address the following topics. The plasmonic lightning-rod effect could be studied for materials beyond gold. In addition to the obvious options of other plasmonic materials such as silver and aluminum, other materials such as doped semiconductors (ZrN) or planar semimetals (graphene) could also be considered. The study of PLRE phenomena could also be broadened to include materials that support phonon modes, thereby substituting free charge carriers in metals with bound charges. Furthermore, PLRE could also be studied for complementary aperture-type PAs utilizing Babinet's principle [4, 71]. By gaining an understanding of the individual mechanisms of the PLRE, we can provide guidelines for designing plasmonic antennas with optimized performance, primarily targeting significant field enhancements and field gradients, which are crucial for a range of applications including sensing, photoemission, and optical manipulation.

References

[1] HOHENESTER, U. *Nano and Quantum Optics : an Introduction to Basic Principles and Theory*. 1st ed. Springer Cham, Switzerland, 2020. ISBN 978-3-030-30503-1.

[2] H. BENISTY, J. Greffet; LALANNE, P. *Introduction to Nanophotonics*. 1st ed. Oxford University Press, England, 2022. ISBN 978–0–19–878613–9.

[3] MAIER, S. *Plasmonics: Fundamentals and Applications*. 1st ed. Springer New York, NY, 2007. ISBN 978-0-387-33150-8.

[4] HRTOŇ, M.; KONEČNÁ, A.; HORÁK, M.; ŠIKOLA, T.; KŘÁPEK, V. Plasmonic Antennas with Electric, Magnetic, and Electromagnetic Hot Spots Based on Babinet's Principle. *Phys. Rev. Appl.* 2020, vol. 13, p. 054045. Available from DOI: 10.1103/PhysRevApplied.13.054045.

[5] SCHULLER, J.; BARNARD, E.; CAI, W.; JUN, Y.; WHITE, J., et al. Plasmonics for extreme light concentration and manipulation. *Nature Materials*. 2010, vol. 9, no. 3, pp. 193–204. Available from DOI: 10.1038/nmat2630.

[6] KINKHABWALA, A.; YU, Z.; FAN, S.; AVLASEVICH, Y.; MÜLLEN, K., et al. Large single-molecule fluorescence enhancements produced by a bowtie nanoantenna. *Nature Photonics*. 2009, vol. 3, no. 11, pp. 654–657. Available from DOI: 10.1038/nphoton.2009.187.

[7] LIAO, P.; WOKAUN, A. Lightning rod effect in surface enhanced Raman scattering. *The Journal of Chemical Physics*. 1982, vol. 76, no. 1, pp. 751–752. Available from DOI: 10.1063/1.442690.

[8] GERSTEN, J. The effect of surface roughness on surface enhanced Raman scattering. *The Journal of Chemical Physics*. 1980, vol. 72, no. 10, pp. 5779–5780. Available from DOI: 10.1063/1.439002.

[9] BITTON, O.; GUPTA, S.; HOUBEN, L.; KVAPIL, M.; KŘÁPEK, V., et al. Vacuum Rabi splitting of a dark plasmonic cavity mode revealed by fast electrons. *Nature Communications*. 2020, vol. 11, no. 1, p. 487. Available from DOI: 10.1038/s41467-020-14364-3.

[10] URBIETA, M.; BARBRY, M.; ZHANG, Y.; KOVAL, P.; SÁNCHEZ-PORTAL, D., et al. Atomic-Scale Lightning Rod Effect in Plasmonic Picocavities: A Classical View to a Quantum Effect. *ACS Nano*. 2018, vol. 12, no. 1, pp. 585–595. Available from DOI: 10.1021/acsnano.7b07401.

[11] FUKUOKA, N.; TANABE, K. Lightning-Rod Effect of Plasmonic Field Enhancement on Hydrogen-Absorbing Transition Metals. *Nanomaterials*. 2019, vol. 9, no. 9. Available from DOI: 10.3390/nano9091235.

[12] WILLIAMS, D.; CARTER, C. *Transmission Electron Microscopy: A Textbook for Materials Science*. 2nd ed. Springer New York, NY, 2009. ISBN 978-1-4419-9583-4.

[13] EGERTON, R. *Electron Energy-Loss Spectroscopy in the Electron Microscope*. 3rd ed. Springer New York, NY, 2011. ISBN 978-0-387-76500-6.

[14] BATSON, P.; DELLBY, N.; KRIVANEK, O. Sub-ångstrom resolution using aberration corrected electron optics. *Nature*. 2002, vol. 418, no. 6898, pp. 617–620. Available from DOI: 10.1038/nature00972.

[15] REIMER, L.; KOHL, H. *Transmission Electron Microscopy: Physics of Image Formation*. 5th ed. Springer New York, NY, 2008. ISBN 978-0-387-34758-5.

[16] RUSKA, E. The development of the electron microscope and of electron microscopy. *Rev. Mod. Phys.* 1987, vol. 59, pp. 627–638. Available from DOI: 10.1103/RevModPhys.59.627.

[17] KARLÍK, M. *Úvod do transmisní elektronové mikroskopie*. 1st ed. České vysoké učení technické v Praze, Praha, 2011. ISBN 978-80-01-04729-3.

[18] TANAKA, M. *Glossary of TEM Terms* [online]. JEOL Ltd. [visited on 2024-02-29]. Available from: https://www.jeol.co.jp/en/words/emterms/search_result.html?keyword=..

[19] LENCOVÁ, B.; ZLÁMAL, J. A new program for the design of electron microscopes. *Physics Procedia*. 2008, vol. 1, no. 1, pp. 315–324. Available from DOI: 10.1016/j.phpro.2008.07.111.

[20] BIGAS, M.; CABRUJA, E.; FOREST, J.; SALVI, J. Review of CMOS image sensors. *Microelectronics Journal*. 2006, vol. 37, no. 5, pp. 433–451. Available from DOI: 10.1016/j.mejo.2005.07.002.

[21] LEVIN, B. Direct detectors and their applications in electron microscopy for materials science. *Journal of Physics: Materials*. 2021, vol. 4, no. 4, p. 042005. Available from DOI: 10.1088/2515-7639/ac0ff9.

[22] OPHUS, C. Four-Dimensional Scanning Transmission Electron Microscopy (4D-STEM): From Scanning Nanodiffraction to Ptychography and Beyond. *Microscopy and Microanalysis*. 2019, vol. 25, pp. 1–20. Available from DOI: 10.1017/S1431927619000497.

[23] GUBBENS, A.; BARFELS, M.; TREVOR, C.; TWESTEN, R.; MOONEY, P., et al. The GIF Quantum, a next generation post-column imaging energy filter. *Ultramicroscopy*. 2010, vol. 110, no. 8, pp. 962–970. Available from DOI: 10.1016/j.ultramic.2010.01.009.

[24] NEWBURY, D.; BRIGHT, D.; SCOTT, J.; MICHAEL, J.; KOTULA, P. Rapid X-ray Spectrum Imaging with the Silicon Drift Detector (SDD): Microstructural Characterization with NIST Lispix. *Microscopy and Microanalysis - MICROSC MICROANAL*. 2007, vol. 13. Available from DOI: 10.1017/S1431927607071371.

[25] KITTEL, C. *Introduction to solid state physics*. 8th ed. John Wiley & Sons, Hoboken, New Jersey, 2005. ISBN 0-471-41526-X.

[26] ZUO, J.; SPENCE, J. *Advanced Transmission Electron Microscopy: Imaging and Diffraction in Nanoscience*. 1st ed. Springer New York, NY, 2017. ISBN 978-1-4939-6607-3.

[27] WILLIAMS, D.; CARTER, C. *Transmission Electron Microscopy: Diffraction, Imaging, and Spectrometry*. 1st ed. Springer Cham, Switzerland, 2016. ISBN 978-3-319-26651-0.

[28] MADSEN, J.; SUSI, T. The abTEM code: transmission electron microscopy from first principles. *Open Research Europe*. 2021, vol. 1, no. 24. Available from DOI: 10.12688/openreseurope.13015.2.

[29] KRIVANEK, O.; CHISHOLM, M..; NICOLOSI, V.; PENNYCOOK, T.; CORBIN, G., et al. Atom-by-atom structural and chemical analysis by annular dark-field electron microscopy. *Nature*. 2010, vol. 464, no. 7288, pp. 571–574. Available from DOI: 10.1038/nature08879.

[30] GARCÍA DE ABAJO, F. Optical excitations in electron microscopy. *Rev. Mod. Phys.* 2010, vol. 82, pp. 209–275. Available from DOI: 10.1103/RevModPhys.82.209.

[31] KRIVANEK, O.; DELLBY, N.; HACHTEL, J.; IDROBO, J.; HOTZ, M., et al. Progress in ultrahigh energy resolution EELS. *Ultramicroscopy*. 2019, vol. 203, pp. 60–67. Available from DOI: 10.1016/j.ultramic.2018.12.006.

[32] KRIVANEK, O.; LOVEJOY, T.; MURFITT, M.; SKONE, G.; BATSON, P., et al. Towards sub-10 meV energy resolution STEM-EELS. *Journal of Physics: Conference Series*. 2014, vol. 522, p. 012023. Available from DOI: 10.1088/1742-6596/522/1/012023.

[33] KRIVANEK, O.; LOVEJOY, T. C; DELLBY, N.; AOKI, T.; CARPENTER, R., et al. Vibrational spectroscopy in the electron microscope. *Nature*. 2014, vol. 514, no. 7521, pp. 209–212. Available from DOI: 10.1038/nature13870.

[34] REZ, P.; AOKI, T.; MARCH, K.; GUR, D.; KRIVANEK, O., et al. Damage-free vibrational spectroscopy of biological materials in the electron microscope. *Nature Communications*. 2016, vol. 7, no. 1, p. 10945. Available from DOI: 10.1038/ncomms10945.

[35] LAGOS, M.; TRÜGLER, A.; HOHENESTER, U.; BATSON, P. Mapping vibrational surface and bulk modes in a single nanocube. *Nature*. 2017, vol. 543, no. 7646, pp. 529–532. Available from DOI: 10.1038/nature21699.

[36] STÖGER-POLLACH, M.; FRANCO, H.; SCHATTSCHNEIDER, P.; LAZAR, S.; SCHAFFER, B., et al. Čerenkov losses: A limit for bandgap determination and Kramers–Kronig analysis. *Micron*. 2006, vol. 37, no. 5, pp. 396–402. Available from DOI: 10.1016/j.micron.2006.01.001.

[37] GRANERØD, C.; ZHAN, W.; PRYTZ, Ø. Automated approaches for band gap mapping in STEM-EELS. *Ultramicroscopy*. 2018, vol. 184, pp. 39–45. Available from DOI: 10.1016/j.ultramic.2017.08.006.

[38] KOCIAK, M.; STÉPHAN, O. Mapping plasmons at the nanometer scale in an electron microscope. *Chem. Soc. Rev.* 2014, vol. 43, pp. 3865–3883. Available from DOI: 10.1039/C3CS60478K.

[39] GRIFFITHS, D. *Introduction to electrodynamics*. 3rd ed. Prentice Hall, New Jersey, 1999. ISBN 0-13-805326-X.

[40] JACKSON, J. *Classical Electrodynamics*. 3rd ed. John Wiley & Sons Inc, New Jersey, 1998. ISBN 978-0-471-30932-1.

[41] JOHNSON, P.; CHRISTY, R. Optical Constants of the Noble Metals. *Phys. Rev. B*. 1972, vol. 6, pp. 4370–4379. Available from DOI: 10.1103/PhysRevB.6.4370.

[42] OTTO, A. Excitation of nonradiative surface plasma waves in silver by the method of frustrated total reflection. *Zeitschrift für Physik A Hadrons and nuclei*. 1968, vol. 216, no. 4, pp. 398–410. Available from DOI: 10.1007/BF01391532.

[43] KRETSCHMANN, E.; RAETHER, H. Notizen: Radiative Decay of Non Radiative Surface Plasmons Excited by Light. *Zeitschrift für Naturforschung A*. 1968, vol. 23, no. 12, pp. 2135–2136. Available from DOI: doi:10.1515/zna-1968-1247.

[44] WILLETS, K.; VAN DUYNE, R. Localized Surface Plasmon Resonance Spectroscopy and Sensing. *Annual Review of Physical Chemistry*. 2007, vol. 58, no. Volume 58, 2007, pp. 267–297. Available from DOI: 10.1146/annurev.physchem.58.032806.104607.

[45] AĆIMOVIĆ, S.; ORTEGA, M.; SANZ, V.; BERTHELOT, J.; GARCIA-CORDERO, J., et al. LSPR Chip for Parallel, Rapid, and Sensitive Detection of Cancer Markers in Serum. *Nano Letters*. 2014, vol. 14, no. 5, pp. 2636–2641. Available from DOI: 10.1021/nl500574n.

[46] ATWATER, H.; POLMAN, A. Plasmonics for improved photovoltaic devices. *Nature Materials*. 2010, vol. 9, no. 3, pp. 205–213. Available from DOI: 10.1038/nmat2629.

[47] NORDLANDER, P.; OUBRE, C.; PRODAN, E.; LI, K.; STOCKMAN, M. Plasmon Hybridization in Nanoparticle Dimers. *Nano Letters*. 2004, vol. 4, no. 5, pp. 899–903. Available from DOI: 10.1021/nl049681c.

[48] AIZPURUA, J.; BRYANT, G.; RICHTER, L.; GARCÍA DE ABAJO, F.; KELLEY, B., et al. Optical properties of coupled metallic nanorods for field-enhanced spectroscopy. *Phys. Rev. B*. 2005, vol. 71, p. 235420. Available from DOI: 10.1103/PhysRevB.71.235420.

[49] NIE, S.; EMORY, S. Probing Single Molecules and Single Nanoparticles by Surface-Enhanced Raman Scattering. *Science*. 1997, vol. 275, no. 5303, pp. 1102–1106. Available from DOI: 10.1126/science.275.5303.1102.

[50] NESHEV, D.; AHARONOVICH, I. Optical metasurfaces: new generation building blocks for multi-functional optics. *Light: Science & Applications*. 2018, vol. 7, no. 1, p. 58. Available from DOI: 10.1038/s41377-018-0058-1.

[51] GARCÍA DE ABAJO, F.; HOWIE, A. Retarded field calculation of electron energy loss in inhomogeneous dielectrics. *Phys. Rev. B*. 2002, vol. 65, p. 115418. Available from DOI: 10.1103/PhysRevB.65.115418.

[52] HOHENESTER, U. *MNPBEM toolbox* [online]. UNIVERSITÄT GRAZ. [visited on 2024-03-17]. Available from: https://physik.uni-graz.at/de/mnpbem/.

[53] *COMSOL Multiphysics* [online]. COMSOL. [visited on 2024-03-17]. Available from: https://www.comsol.com/.

[54] *High-Performance Nanophotonic Simulation Software - Lumerical* [online]. Ansys Lumerical. [visited on 2024-03-17]. Available from: https://www.lumerical.com/.

[55] SMAJIC, J.; HAFNER, C.; RAGUIN, L.; TAVZARASHVILI, K.; MISHRIKEY, M. Comparison of Numerical Methods for the Analysis of Plasmonic Structures. *Journal of Computational and Theoretical Nanoscience*. 2009, vol. 6, pp. 763–774. Available from DOI: 10.1166/jctn.2009.1107.

[56] MYROSHNYCHENKO, V.; RODRÍGUEZ-FERNÁNDEZ, J.; PASTORIZA-SANTOS, I.; FUNSTON, A.; NOVO, C., et al. Modelling the optical response of gold nanoparticles. *Chem. Soc. Rev.* 2008, vol. 37, pp. 1792–1805. Available from DOI: 10.1039/B711486A.

[57] HOHENESTER, U.; TRÜGLER, A. MNPBEM – A Matlab toolbox for the simulation of plasmonic nanoparticles. *Computer Physics Communications*. 2012, vol. 183, no. 2, pp. 370–381. Available from DOI: 10.1016/j.cpc.2011.09.009.

[58] HOHENESTER, U. Simulating electron energy loss spectroscopy with the MNPBEM toolbox. *Computer Physics Communications*. 2014, vol. 185, no. 3, pp. 1177–1187. Available from DOI: 10.1016/j.cpc.2013.12.010.

[59] RITCHIE, R. Plasma Losses by Fast Electrons in Thin Films. *Phys. Rev.* 1957, vol. 106, pp. 874–881. Available from DOI: 10.1103/PhysRev.106.874.

[60] WAXENEGGER, J.; TRÜGLER, A.; HOHENESTER, U. Plasmonics simulations with the MNPBEM toolbox: Consideration of substrates and layer structures. *Computer Physics Communications*. 2015, vol. 193, pp. 138–150. Available from DOI: 10.1016/j.cpc.2015.03.023.

[61] KOLLMANN, H.; PIAO, X.; ESMANN, M.; BECKER, S.; HOU, D., et al. Toward Plasmonics with Nanometer Precision: Nonlinear Optics of Helium-Ion Milled Gold Nanoantennas. *Nano Letters*. 2014, vol. 14, no. 8, pp. 4778–4784. Available from DOI: 10.1021/nl5019589.

[62] ŠIKOLA, T.; SPOUSTA, J.; DITTRICHOVÁ, L.; NEBOJSA, A.; PEŘINA, V., et al. Dual ion-beam deposition of metallic thin films. *Surface and Coatings Technology*. 1996, vol. 84, no. 1, pp. 485–490. Available from DOI: 10.1016/S0257-8972(95)02823-4.

[63] KLINGER, M.; JÄGER, A. *Crystallographic Tool Box* (*CrysTBox*): automated tools for transmission electron microscopists and crystallographers. *Journal of Applied Crystallography*. 2015, vol. 48, no. 6, pp. 2012–2018. Available from DOI: 10.1107/S1600576715017252.

[64] KEJÍK, L.; HORÁK, M.; ŠIKOLA, T.; KŘÁPEK, V. Structural and optical properties of monocrystalline and polycrystalline gold plasmonic nanorods. *Opt. Express*. 2020, vol. 28, no. 23, pp. 34960–34972. Available from DOI: 10.1364/OE.409428.

[65] MITCHELL, D. Determination of mean free path for energy loss and surface oxide film thickness using convergent beam electron diffraction and thickness mapping: a case study using Si and P91 steel. *Journal of Microscopy*. 2006, vol. 224, no. 2, pp. 187–196. Available from DOI: https://doi.org/10.1111/j.1365-2818.2006.01690.x.

[66] IAKOUBOVSKII, K.; MITSUISHI, K.; NAKAYAMA, Y.; FURUYA, K. Thickness measurements with electron energy loss spectroscopy. *Microscopy research and technique*. 2008, vol. 71, pp. 626–31. Available from DOI: 10.1002/jemt.20597.

[67] HORÁK, M.; BUKVIŠOVÁ, K.; ŠVARC, V.; JASKOWIEC, J.; KŘÁPEK, V., et al. Comparative study of plasmonic antennas fabricated by electron beam and focused ion beam lithography. *Scientific Reports*. 2018, vol. 8, no. 1, p. 9640. Available from DOI: 10.1038/s41598-018-28037-1.

[68] HORÁK, M.; ŠIKOLA, T. Influence of experimental conditions on localized surface plasmon resonances measurement by electron energy loss spectroscopy. *Ultramicroscopy*. 2020, vol. 216, p. 113044. Available from DOI: 10.1016/j.ultramic.2020.113044.

[69] KŘÁPEK, V.; KOH, A.; BŘÍNEK, L.; HRTOŇ, M.; TOMANEC, O., et al. Spatially resolved electron energy loss spectroscopy of crescent-shaped plasmonic antennas. *Opt. Express*. 2015, vol. 23, no. 9, pp. 11855–11867. Available from DOI: 10.1364/OE.23.011855.

[70] SCHMIDT, F.; DITLBACHER, H.; HOFER, F.; KRENN, J.; HOHENESTER, U. Morphing a Plasmonic Nanodisk into a Nanotriangle. *Nano Letters*. 2014, vol. 14, no. 8, pp. 4810–4815. Available from DOI: 10.1021/nl502027r.

[71] HORÁK, M.; KŘÁPEK, V.; HRTOŇ, M.; KONEČNÁ, A.; LIGMAJER, F., et al. Limits of Babinet's principle for solid and hollow plasmonic antennas. *Scientific Reports*. 2019, vol. 9, no. 1, p. 4004. Available from DOI: 10.1038/s41598-019-40500-1.

List of abbreviations

ADF	Annular dark field
AEM	Analytical electron
AES	Auger electron spectroscopy
BF	Bright field
BFP	Back focal plane
BEM	Boundary element method
BP	Bulk plasmon
BSE	Backscattered electrons
CBED	Convergent beam electron diffraction
CCD	Charge-coupled device
CMOS	Complementary metal–oxide–semiconductor
CL	Cathodoluminescence
CTF	Contrast transfer function
DF	Dark field
DP	Diffraction pattern
EBIC	Electron-beam induced current
EBL	Electron beam lithography
EDS	Energy dispersive X-ray spectroscopy
EELS	Electron energy loss spectroscopy
EFTEM	Energy filtered transmission electron microscopy
ELNES	Energy-loss near-edge structure
FDTD	Finite-difference time-domain
FEG	Field emission gun
FEM	Finite element method
FFP	Front focal plane
FIB	Focused ion beam
FWHM	Full width at half maximum

HAADF	High-angle annular dark field
HRTEM	High resolution transmission electron microscopy
IMFP	Inelastic mean free path
LDA	Longitudinal dipole antibonding
LDB	Longitudinal dipole bonding
LO	Longitudinal optical
LSP	Localized surface plasmon
LSPR	Localized surface plasmon resonance
LST	Lyddane-Sachs-Teller
MA	Multimodal assembly
MNPBEM	Metallic nanoparticle boundary element method
PA	Plasmonic antenna
PLRE	Plasmonic lightning-rod effect
Q	Quality
QR	Quadrupole resonance
ROI	Region of interest
SAED	Selected area electron diffraction
SEM	Scanning electron microscopy
SP	Surface plasmon
SPP	Surface plasmon polariton
STEM	Scanning transmission electron microscopy
TEM	Transmission electron microscopy
TE	Transverse electric
TM	Transverse magnetic
TO	Transverse optical
ZLP	Zero loss peak